**Rochester Institute of Technology**
**RIT Scholar Works**

Theses                                                      Thesis/Dissertation Collections

2009

# Investigation and development of advanced models of thermoelectric generators for power generation applications

Emil Sandoz-Rosado

Follow this and additional works at: http://scholarworks.rit.edu/theses

# Investigation and Development of Advanced Models of Thermoelectric Generators for Power Generation Applications

By

## Emil Jose Sandoz-Rosado

A Thesis Submitted in Partial Fulfillment of the Requirement
for Master of Science in Mechanical Engineering

Approved by:

**Dr. Robert Stevens** – *Thesis Advisor*                    _____
Department of Mechanical Engineering


**Dr. Steve Weinstein**                    _____
Department Head of Chemical Engineering


**Dr. Edward Hensel**                    _____
Department Head of Mechanical Engineering


**Department of Mechanical Engineering**
**Kate Gleason College of Engineering**
**Rochester Institute of Technology**
**Rochester, New York 14623**
**September 2009**

**PERMISSION TO REPRODUCE THE THESIS**

# Investigation and Development of Advanced Models of Thermoelectric Generators for Power Generation Applications

I, EMIL JOSE SANDOZ-ROSADO, hereby grant permission to the Wallace Memorial Library of Rochester Institute of Technology to reproduce my thesis in the whole or part. Any reproduction will not be for commercial use or profit.

Date: _____     Signature: _____

September 2009

# Abstract

With developing interest in power generation applications of thermoelectrics and the growing influence of advanced materials on thermoelectric device fabrication, there is an increased demand for better understanding of module-level behavior. Likewise, novel module geometries are being explored for higher performance and require sophisticated modeling methods.

In addition to new geometrical design, transport phenomena, such as Thomson heating and contact resistances, aggravate the complexity of modeling thermoelectric modules (TEMs) and thus limit design capability. Typically, these effects are either approximated (or in some cases neglected entirely) with little exploration in to the validity of the underlying assumptions associated with the approximation. As such, standard models are often predicated on assumptions that cannot be made beyond very limited operating regimes. Consequently, most TEM analysis generally utilizes simplistic methods of modeling on a module-level scale, which introduce inaccuracies that must be redressed.

Particularly with larger temperature gradients, typically negligible effects could begin to impact overall system performance. Material property temperature-dependency, combined with leakage effects, leave much to be desired of the simple property-average-based models. Additionally, one-dimensional (1-D) models neglect the contribution of three-dimensional (3-D) module facets that can significantly impact TEM performance. To compound the analytical issue, complex material technologies are emerging that will require robust models for module design.

With burgeoning focus in using thermoelectrics for waste heat recovery in automobiles, industrial processes and power plants, new application and commercial development of high temperature TEMs is imminent. However, modeling design and optimization of TEMs has been piecemeal at best. Hence, it is imperative that a comprehensive model be developed for TEMs that addresses some of the analytical problems stemming from over-simplification. The primary intention of this work is to develop and validate a comprehensive model that can be used as a TEM design tool and to quantify the error in the simple 1-D analytical models.

The scope of this work is multifaceted. First, several models are developed, implemented and compared to each other as design tools that are useful for determining material performance and also for optimizing TEM performance. An improved 1-D analytical model, a unique asymptotic model and a comprehensive 3-D finite element (FE) model are created and established. These models are compared to each other for both validation and for quantification of error in the analytical models. Secondly, the quantification of error in 1-D analytical models based on module parameters, called error mapping, can be used as a design tool in and of itself to either identify regimes where a 1-D model is inaccurate (and thus establish when 3-D FE modeling is required), or as a corrective factor to a 1-D

model. Thirdly, an experimental test stand is developed for device characterization, to be used either for system-level integration or for future model validation. Finally, the Thomson effect is analytically explored and detailed, and its contribution to the overall performance of a TEM is quantified. The role of the Thomson effect in previous analyitical models is nebulous, but has been elucidated in this thesis both with derivation and the development of the asymptotic model, which is the first analytical solution to the non-linear thermoelectric governing equations.

Ultimately, this thesis defines the advantages and limitations of current TEM models, quantifies their error and provides several new design tools that can be used for material selection, module optimization and system-level design. These new design tools will provide new leverage to advance thermoelectrics as a robust power generation technology at a time when such capability is critical.

# Acknowledgements

I would like to take this opportunity to thank the GEM Consortium for their support, Dr. Edward Hensel and the Mechanical Engineering Department for offering me the opportunity and encouraging me to pursue an advanced degree, Dr. Steven Weinstein for his ability to inspire and instill confidence in the face of daunting and overwhelming tasks, and above all, Dr. Robert Stevens for going beyond the role of adviser, whose mentorship made it possible for me to flourish as a successful student, researcher and, ultimately, committed socially-responsible human being.

# Contents

# List of Figures

# List of Tables

# Nomenclature

| Latin Symbol | Parameter | Units |
|:---:|:---|:---|
| $A$ | Cross-sectional Leg Area | m$^2$ |
| $A_{Gap}$ | Area Between Legs | m$^2$ |
| $A_p$ | Cross-sectional Area P-type Leg | m$^2$ |
| $A_n$ | Cross-sectional Area N-type Leg | m$^2$ |
| $B_i$ | Dimensionless Coefficient of $\bar{x}$ in $\bar{T}(\bar{x})$ | $-$ |
| $C_i$ | Dimensionless Coefficient of $\bar{\alpha}(\bar{T})$ | $-$ |
| $D$ | Leg Spacing | m |
| $D_{norm}$ | Nominal Leg Spacing for 2-D Optimization Series | m |
| $D_P$ | Parameterized Leg Spacing for 2-D Optimization Series | m |
| $D_i$ | Dimensionless Coefficient of $R_A$ in $\bar{T}(\bar{x})$ | $-$ |
| $E_{Melcor}$ | Error Between 1-D 3-D Models, Melcor | $-$ |
| $E_{CRC}$ | Error Between 1-D and 3-D Models, CRC | $-$ |
| $E_{Melcor,Pred}$ | Predictive Error Between 1-D and 3-D Models, Melcor | $-$ |
| $E_{CRC,Pred}$ | Predictive Error Between 1-D and 3-D Models, CRC | $-$ |
| $I$ | Electrical Current | A |
| $J$ | Current Density | A/m$^2$ |
| $k$ | Thermal Conductivity of a Thermoelectric Material | W/mK |
| $k_{Cer}$ | Thermal Conductivity of a Ceramic Substrate | W/mK |
| $k_{Cu}$ | Thermal Conductivity of the Copper Contact | W/mK |
| $k_n$ | Thermal Conductivity of an N-type Material | W/mK |
| $k_p$ | Thermal Conductivity of a P-type Material | W/mK |
| $K$ | Thermal Conductance of a Thermocouple | W/K |
| $K_{TEM}$ | Thermal Conductance of a Thermoelectric Module | W/K |
| $L$ | Leg Length | m |
| $n$ | Number of Elements in a Subdomain | $-$ |
| $N$ | Number of Thermocouples or Thermopiles in a Module | $-$ |
| $P$ | Power Produced by a Thermocouple | W |
| $P_{TEM}$ | Power Produced by a Module | W |
| $q$ | Heat Flow | W |
| $q_C$ | Heat Flow Out of a Thermocouple | W |
| $q_H$ | Heat Flow Into a Thermocouple | W |

| Latin Symbol | Parameter | Units |
|---|---|---|
| $q_{Peltier}$ | Peltier Heat | W |
| $Q'''_{Thomson}$ | Thomson Heat | W/m$^3$ |
| $R$ | Electrical Resistance of a Thermocouple | $\Omega$ |
| $R_A$ | Ratio of Joule Heat to Heat Conduction | $-$ |
| $R_{Cer}$ | Thermal Resistance of the Ceramic Substrate | K/W |
| $R_{Load}$ | Electrical Load Resistance | $\Omega$ |
| $R_t$ | Thermal Resistance of a Thermocouple | K/W |
| $R_{TE,Eq}$ | Equivalent Thermal Resistance of a Thermoelectric | K/W |
| $R_{TEM}$ | Electrical Resistance of a Module | $\Omega$ |
| $t_{Cer}$ | Thickness of Ceramic Substrate | m |
| $t_{Cu}$ | Thickness of Cu Contact | m |
| $t_{Cu,norm}$ | Nominal Thickness of Contact for 2-D Optimization | m |
| $t_{Cu,P}$ | Parameterized Thickness of Contact for 2-D Optimization | m |
| $t_{Solder}$ | Thickness of Solder | m |
| $t_{Solder,norm}$ | Nominal Thickness of Solder for 2-D Optimization | m |
| $t_{Solder,P}$ | Parameterized Thickness of Solder for 2-D Optimization | m |
| $T$ | Absolute Temperature | K |
| $\bar{T}$ | Normalized Temperature | $-$ |
| $T_C$ | Cold-Side Temperature | K |
| $T_{CE}$ | Equivalent Cold-Side Temperature | K |
| $T_H$ | Hot-Side Temperature | K |
| $T_{HE}$ | Equivalent Hot-Side Temperature | K |
| $T_n$ | Temperature Profile in the N-type Leg | K |
| $T_p$ | Temperature Profile in the P-type Leg | K |
| $V$ | Electromotive Force | $\mu$V, V |
| $V_{Open}$ | Open Circuit Voltage | V |
| $W$ | Leg Width | m |
| $x$ | Coordinate Along Length of Leg | m |
| $\bar{x}$ | Unitless Coordinate Along Length of Leg | $-$ |
| $ZT$ | Figure of Merit | $-$ |

| Greek Symbol | Parameter | Units |
| --- | --- | --- |
| $\alpha$ | Seebeck Coefficient for a Module | $\mu$V/K |
| $\bar{\alpha}$ | Normalized Seebeck Coefficient | $-$ |
| $\alpha_{p,n}$ | Seebeck Coefficient for a Thermocouple | $\mu$V/K |
| $\alpha_p$ | Seebeck Coefficient for a P-type Material | $\mu$V/K |
| $\alpha_n$ | Seebeck Coefficient for an N-type Material | $\mu$V/K |
| $\beta_i$ | Dimensional Coefficient of $\alpha(T)$ | $-$ |
| $\epsilon$ | Asymptotic Expansion Coefficient | $-$ |
| $\epsilon_{EM}$ | Emissivity | $-$ |
| $\eta$ | Thermodynamic Efficiency | $-$ |
| $\rho$ | Electrical Resistivity | $\Omega$m |
| $\rho_p$ | Electrical Resistivity of a P-type Material | $\Omega$m |
| $\rho_n$ | Electrical Resistivity of an N-type Material | $\Omega$m |
| $\sigma$ | Electrical Conductivity | S/m |
| $\sigma_{Cu}$ | Electrical Conductivity of Copper Contact | S/m |
| $\sigma_p$ | Electrical Conductivity of a P-type Material | S/m |
| $\sigma_n$ | Electrical Conductivity of an N-type Material | S/m |
| $\sigma_{SB}$ | Stefan-Boltzmann Constant | W/m$^2$K$^4$ |
| $\tau$ | Thomson Coefficient for a Material | $\mu$V/K |
| $\tau^*$ | Effective Bulk Thomson Coefficient for a Material | $\mu$V/K |
| $\tau_{p,n}$ | Thomson Coefficient for a Thermocouple | $\mu$V/K |
| $\tau_p$ | Thomson Coefficient for a P-type Material | $\mu$V/K |
| $\tau_n$ | Thomson Coefficient for an N-type Material | $\mu$V/K |
| $\tau_{TEM}$ | Thomson Coefficient for a Module | $\mu$V/K |

# Chapter 1

# Introduction to Thermoelectrics

Over the past half century thermoelectrics have been the object of much study [1], and are emerging as a potential means for increasing electrical power production, particularly in the realm of waste heat recovery from low grade heat sources. Thermoelectric modules (TEMs) utilize electron transport phenomena in extrinsic (doped) semiconductors for either refrigeration or electrical power generation applications. In the presence of a direct current TEMs will perform a refrigeration process, employing electrons as the primary energy carrier instead of the fluid coolant typically used in vapor-compression cycles. Though the majority of thermoelectric applications involve cooling, demands for development of alternative energy and remote power generation have coalesced into a niche market for thermoelectric devices. Because market demand for TEMs, until recently, was dominated by refrigeration, thermoelectric material development remained generally in the near-room-temperature regime. With the exception of the extreme minority of high-temperature power generation applications (Global Thermoelectric, Globelte.com), current material design of commercially-available TEMs restricts maximum operating temperatures to about $250\,^\circ$C.

## 1.1 Motivation

In lieu of unbridled economic development and industrialization, demand for energy has exploded and displays few signs of receding or plateauing. Coupled with a dependency on a limited reservoir of fossil fuels, inefficient methods of power conversion, and pervasive damage to the environment, energy has emerged as a critical global issue in the 21st century.

More efficient and cleaner energy conversion has been a growing issue in the scientific community since the middle of the last century [2]. Most power plants that convert heat into electricity employ multiple stages of energy conversion, with irreversible losses associated with each stage. Resultantly, most combustion engines, generators and plants convert only about one third (as much as forty percent in high-efficiency reactors) into desired mechanical or electrical energy [3]. The remaining two thirds of the energy are accounted for by exhausted waste heat (although in automobiles, some of this excess heat is sometimes desirable for climate control). More explicitly put, over half of the potential energy consumed

in power production is wasted in the form of heat. Needless to say, development of more efficient energy systems and more direct forms of energy conversion is paramount.

Thermoelectrics pose a unique solution to the issue of efficiency, since they recover waste heat in the most direct manner, namely electron transport. The implications of employing thermoelectrics as generators for reduction of fuel consumption via waste heat recovery are substantial. In 2007 the United States consumed 103 quadrillion BTUs of energy, with approximately half of that energy wasted in the form of heat. The thermal pollution of the United States in 2007 accounts for the net energy of New York State's industrial and commercial sectors over a 100 year period. The potential for energy recovery from this waste heat is staggering. Thermoelectrics, once optimized, pose a potential relief in energy consumption.

## 1.2 Historical Context

Upon the preliminary discovery of thermoelectric phenomena, owed to Seebeck circa 1822, little attention was given to the strange heat-induced electrical effect observed in metallic substrates [4]. The reverse of the Seebeck effect is the capacity for a thermoelectric to act as a heat pump or refrigerator in the presence of direct current. This effect was initially observed (but misunderstood) by Jean Charles Peltier in 1834. However, it was the nascent field of Thermodynamics, specifically a premier researcher by the name of William Thomson (better known as Lord Kelvin), that commenced significant study into thermoelectric effects nearly thirty years after Seebeck's initial exposition. Utilizing the evolving field of Thermodynamics as a scientific framework, Thomson fully described all of the observed phenomena associated with thermoelectrics [4].

Study and development of thermoelectrics remained predominately academic for the better part of a century. Dismal energy conversion efficiencies of thermoelectric materials and general lack of interest for direct energy conversion methods discouraged probing into applications that could benefit from thermoelectrics. The eminant field of materials science in the middle of the twentieth century equipped researchers with the expertise and the impetus to improve the operating behavior thermoelectrics.

## 1.3 Characteristics of Modern Thermoelectric Modules

The typical configuration of a TEM is a multitude of thermocouples (or thermopiles), connected in series electrically, and in parallel thermally, as shown in Fig.(1.1). Each couple consists of a negative-majority-carrier doped (n-type) semiconductor leg conjoined in series with a positive-majority-carrier doped (p-type) semiconductor. For electrical insulation and structural support, ceramics typically sandwich the thermopiles.
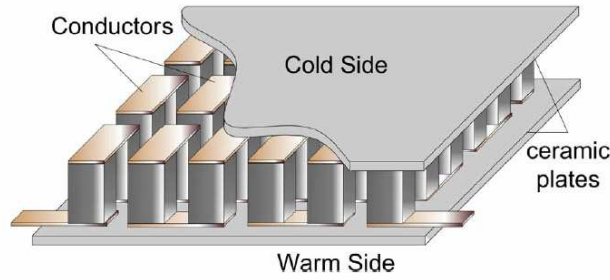
Figure 1.1: Schematic of a Thermoelectric Module [5]

The nomenclature, hot-side interface temperature ($T_H$) and cold-side temperature ($T_C$), are generally accepted in the research community. Typically for generation, a hot side and a cold side temperature are prescribed and the TEM is analyzed accordingly.

A heat-recovery system comprised of thermoelectrics can assume a myriad of geometries and is not limited in scale. Micro-thermoelectrics have been embedded in integrated circuits for cooling, TEMs have been deployed as waste heat recovery systems in semi trucks and have been used for power generation in stoves [6]. There has even been design for a large-scale oceanic power production facility employing thermoelectrics [7]. An additional advantage that compartmentalization offers is interchangeability of failed modules with no system down time. With no moving parts, TEMs can operate continuously for over three decades without failure. Additionally, thermoelectrics are excellent at recovering low-quality energy, and at lower temperature gradients can operate more efficiently than a vapor-compression cycle [7].

Modern thermoelectric devices have a relatively small footprint when compared to other power generation or refrigeration systems. TEMs are predominately limited to rectangular geometries with linear dimensions not exceeding a few centimeters, and typical thicknesses are on the order of millimeters. Much study has been focused on optimization of leg geometries (e.g. length and cross-sectional area), with no attention given to leg spacing, ceramic interface geometry, contact thickness, etc. The length and width of a module is principally limited to a relatively small configuration (on the order of several centimeters) for reduction of structural stresses associated with thermal expansion due to extreme temperature gradients [8].

## 1.4 Figure of Merit

The figure of merit, $ZT$, is a critical unitless metric for evaluating the performance of a given thermoelectric material. Though often incorrectly used to describe module behavior, the figure of merit is most accurately used to describe the ideal performance ceiling of a module, since it cannot account for various module-level inefficiencies. The figure of merit is expressed as follows [4]:

$$ZT = \frac{\alpha^2 \sigma}{k} T \tag{1.1}$$

The figure of merit contains the inherent relationships between the thermoelectric material properties (both electrical and thermal) with respect to overall performance. Clearly, decreasing thermal conductivity would increase the overall figure of merit. By decreasing thermal conduction the amount of stray heat that transmits through the TEM without being converted into electrical power is minimized. Since conduction is an irreversible loss, it is imperative to minimize the thermal conductivity of a material. In addition, increasing electrical conductivity diminishes the amount of heat generated by the current in the form of Joule heating (another irreversibility) and thus improves material performance. Finally, increasing the Seebeck coefficient impacts overall material performance the most, as the figure of merit is proportional to the square of the Seebeck coefficient.

Recently, there has been great focus on utilizing new materials science technology to improve the performance of thermoelectric devices. Significant advancement in thermoelectric materials have only occurred in the last fifteen years, as seen in Fig.(1.2). These high-efficiency materials have yet to be implemented commercially, and little study has been done as to their performance on the device-level.
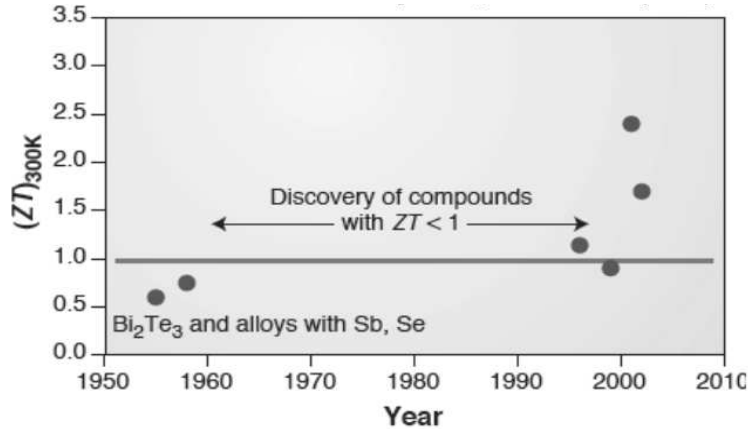


Figure 1.2: Development of ZT since 1950 [1]

The following relationship depicts how the figure of merit governs the maximum material efficiency of an idealistic thermoelectric pair [4].

$$\eta = \frac{T_H - T_C}{T_H} \times \frac{M - 1}{M + T_C/T_H} \tag{1.2}$$

where $T_H$ and $T_C$ are the hot-side temperature and cold-side temperatures respectively and

$$M = \sqrt{1 + \frac{1}{2} Z(T_H + T_C)} \tag{1.3}$$

The first half of the expression in Eq.(1.2) contains the Carnot Efficiency, while the second half of the expression depicts the mitigation of efficiency due to irreversibilities and

contains the average figure of merit. For varying temperature gradients the thermoelectric will exhibit maximum efficiency with respect to the figure of merit as follows:
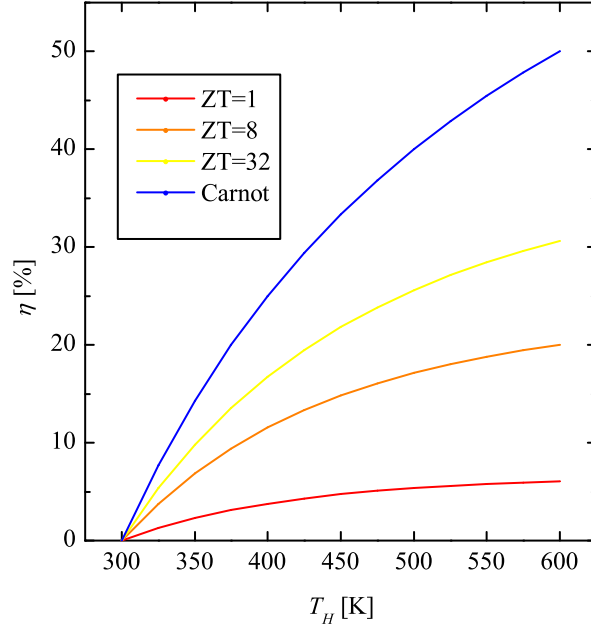


Figure 1.3: Module Efficiency vs. Figure of Merit, $T_C = 300K$

## 1.5   Seebeck Effect

The principal thermoelectric phenomena are the Seebeck, Peltier and Thomson effects. Seebeck characterized the electromotive force (EMF), $V_{open}$, generated by an open circuit thermoelectric experiencing a temperature gradient by the following relationship [8]:

$$dV_{open} = \alpha dT \tag{1.4}$$

$$V_{open} = \int_{T_C}^{T_H} \alpha dT \tag{1.5}$$

This effect is the principal study of this review, as it governs the ability of a thermoelectric system to convert heat flow into electrical energy. One characteristic of the Seebeck effect that is critical to note is that it is a contact phenomenon that only occurs through connection of two thermoelectric materials with different Seebeck coefficients. It should also be noted that Eq.(1.5) accounts for the Thomson effect, which is the electrical power generated or absorbed in the bulk of the material. Eq.(1.4) can be rewritten to define the Seebeck coefficient (or Thermopower), $\alpha$, which can vary spatially and with temperature.

The main driving potential behind the electromotive force is a result of thermal excitation at the junction between an n-type semiconductor and a p-type semiconductor. At the hot end

of the n-type leg, excited electrons begin occupying higher energy states and conversely at the low-temperature end the electrons are remaining in relatively low energy states. The high-energy electrons diffuse toward the available low-energy states, creating a positive voltage with respect to the lower energy electrons at the cold-side (positive $\alpha_n$). The holes in the adjacent, connected, p-type leg also get excited but, due to their polarity, generate a negative voltage (at the hot-side with respect to the cold-side) associated with a negative $\alpha_p$. The voltage that is generated in the p-type semiconductor is negative at the hot side with respect to the cold side because the polarity of the majority carriers, holes, is positive. The result is a relatively large voltage difference between the legs that, in a closed circuit, generates a current. A physical description of this phenomenon would be that the thermally excited electrons in the n-type leg translate through the connection to fill in the holes generated in the p-type leg, thus creating a net current [2]. For 1-D analytical analysis, the overall Seebeck coefficient of a thermocouple is the difference between the Seebeck coefficients of each leg on a given side (i.e. hot side or cold side).

$$\alpha_{Thermocouple} = \alpha_{p,n} = \alpha_p - \alpha_n \tag{1.6}$$

To maximize this difference, it is desirable to have an n-type with a large positive value coupled with a p-type with a large negative value. The polarity of $\alpha$ corresponds to the carrier type. Thus, couples are constituted of one n-type leg and one p-type leg [8].

## 1.6 Peltier Effect

Succinctly, the Peltier Effect is the reverse effect of the Seebeck phenomenon. Thermal energy is absorbed or emitted when translating charge carriers, associated with an electric current, transition from relatively high voltage in the n-type leg to the lower voltage of the p-type leg. The excited carriers in the n-type leg must transition from high energy states to low energy states in the p-type leg. In order to transition they must discharge (or, if moving from p-type to n-type, absorb) energy. The amount of heat absorbed or ejected due to the Peltier Effect for a thermoelement junction is given by:

$$q_{Peltier} = I(\alpha_p - \alpha_n)T = I\alpha_{p,n}T \tag{1.7}$$

where $I$ is the electrical current and the temperature, $T$, is absolute. It is important to note that the heat emitted, or absorbed, due to the Peltier effect occurs at the contact boundary between two materials with differing Seebeck coefficients. The Peltier heat is reversible, as it depends directly on the direction of the carrier flow, or electrical current. Thermoelectric refrigeration cycles are said to be driven by the Peltier effect, but it is important to note that the Peltier effect is present during thermoelectric power generation cycles as well.

## 1.7 Thomson Effect

The Thomson effect is also a reversible thermoelectric phenomena. Similar to the Peltier heat, the Thomson effect is observed when charge carriers change energy levels. The main difference is that the Thomson effect occurs in bulk thermoelectric materials experiencing a temperature gradient, and does not occur at the boundary between two materials with differing Seebeck coefficients. Since the Seebeck coefficient is dependent on temperature, the thermopower for a given material with a temperature gradient will change as a function of the temperature. As carriers move from the hot end to the cold end of a thermopile leg their overall energy will either increase or decrease due to the change in Seebeck coefficient as a function of temperature. This change in electrical energy is accompanied by a reciprocal generation or absorption of heat. The expression for the Thomson heat generated per unit volume is simply:

$$Q'''_{Thomson} = J\tau \frac{dT}{dx} \tag{1.8}$$

where

$$\tau = T\frac{d\alpha}{dT} \tag{1.9}$$

For materials that have Seebeck coefficients that vary dramatically with temperature, or for modules experiencing large temperature gradients, this effect can significantly impact module-level performance. The heat generated or absorbed by the Thomson effect is proportional to the electrical current flowing through the device. As a result, the TEM device behavior can be influenced by this effect (as well as Joule heating) to varying degrees depending on electrical loading conditions.

# Chapter 2

# Literature Review

Previous modeling of thermoelectric modules has focused mainly on analytical predictions, with the incorporation of several effects such as contact resistance. Major limitations of analytical models were the assumptions of temperature-independent properties and 1-D heat flow. Modeling of TEMs is critical for both design of the modules and incorporation of the modules into larger power generation systems. With a robust model, new module geometries can be evaluated and optimized for improved performance and module configurations can be tailored for emergent thermoelectric materials. In addition, because thermoelectric power generation can take place in a myriad of operating conditions (viz. low-grade wast heat recovery, high-grade heat source generation, continuous electrical load, variable load, etc.), a robust model can optimize the module for the conditions it may experience in a given system. For example, a TEM designed for recuperation of waste heat from a diesel truck will have a vastly different configuration than one harvesting body heat for a biomedical device.

Some work has utilized finite element and finite difference techniques for the purposes of examining segmented unicouples [9] and has even incorporated temperature-dependent properties. This exploration of thermoelectric modeling is motivated by the existence of significant discrepancies between the results produced by analytical and numerical techniques. Lau and Buist explored the limits of different techniques used to average material properties for implementation in analytical modeling methods [10]. Analytical solutions utilizing both point-averaged and integral-averaged Seebeck coefficient values were compared to a numerical solution accounting for temperature-dependent properties. The behavior of the numerical model compared to the analytical solutions varies greatly even at temperature gradients within the operating range of current thermoelectrics.

The discrepancy of the models illustrates the inadequacies of the analytical models. Because the analytical models assume averaged property values, the impact of the dramatic changes in material properties at large temperature gradients is neglected. This impact is especially sensitive in the case of the Seebeck coefficient, since the Thomson effect arises from the temperature-dependency of the Seebeck coefficient. The Thomson coefficient can be either augmentative or parasitic, depending on the temperature gradient and the material
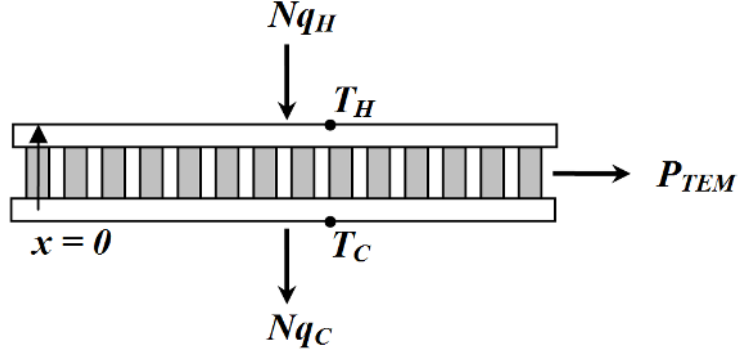
Figure 2.1: Diagram of a thermoelectric module for analysis

properties. In both cases, the Thomson effect can contribute (or detract) significantly from device performance and warrants further exploration into the limitations of current modeling techniques.

There are two main metrics for quantifying the performance of a TEM. The first metric is the power output of the thermoelectric module, $P_{TEM}$, and is typically expressed as a function of either electrical current, $I$, or electrical load resistance, $R_{Load}$. The second metric is the thermodynamic efficiency of the TEM, $\eta$, and likewise is expressed in terms of $I$ or $R_{Load}$. Analytically, both of these metrics can be determined by solving the heat flow into $(N \cdot q_H)$ and out of $(N \cdot q_C)$ the module.

Generally speaking, the steps to analytically solving the system of equations to determine TEM performance are (as seen in Fig.(2.1):

1. Solve the temperature profile, $T(x)$, of the respective heat equation in the thermoelement legs

2. Use the derivative of the temperature profile $\frac{dT}{dx}$ to determine the flow into and out of the module, $N \cdot q_H$ and $N \cdot q_C$

3. With the heat flowing into and out of the module, solve electrical current $I$ if needed

4. Using the heat into and out of the module, obtain $P_{TEM} = N(q_H - q_C)$ and $\eta = 1 - \frac{q_C}{q_H}$

One assumption that is generally made for analytical models is that the Thomson heat is negligible and the Seebeck coefficient is constant (unless otherwise specified). When this assumption is made, the temperature-dependent Seebeck coefficient is averaged over the temperature range experienced by the thermoelectric leg. There are two methods of averaging the Seebeck coefficient, the standard average [4], and the integral average [2]. The assumptions behind this method are later addressed in section 3.2. The integral averaged Seebeck coefficient takes the form:

$$\alpha = \frac{1}{\Delta T} \int_{T_C}^{T_H} \alpha dT \tag{2.1}$$

9

## 2.1   One Dimensional Analytical Solution of a Standard Thermoelectric Module

Let us begin with the simplest technique and the model that is most widely used in industry, the one dimensional model, with constant properties, of a typical TEM. Hodes outlines the approach and assumptions made for the simplified modeling of TEMs [8]. In this model, thermal conductivity and resistivity and Seebeck coefficient of the thermocouples are assumed to be isotropic, and independent of temperature. Additionally, 1-D transport is assumed. Since the Seebeck coefficient is assumed to be constant, it is important to note that the Thompson effect is neglected. Additionally, all connections between pellets are assumed to be perfect electrical and thermal conductors, contributing negligible contact resistances. Likewise, the Seebeck coefficient of all interconnecting materials are assumed to universally be zero. Lineykin and Ben-Yaakov demonstrated that a basic model (utilizing a module-level equivalent Seebeck coefficient, thermal conductivity and electrical resistance) could describe module behavior in certain regimes [5]. Hodes' approach solves the steady state heat diffusion equation and examines the location in the leg of the maximum temperature under different conditions:
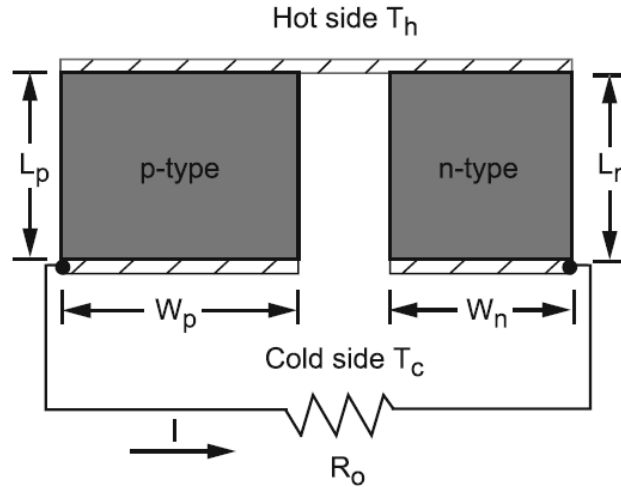


Figure 2.2: Thermopile p-n junction  [11]

$$\frac{d^2T}{dx^2} + \frac{I^2\rho}{kA^2} = 0 \tag{2.2}$$

where $\rho$ is electrical resistivity, $k$ is thermal conductivity, and $A$ is the cross-sectional area of the thermoelectric pellet. The second term in Eq.(2.2) is the contribution of the Joule heating term to the heat diffusion equation. Naturally, the energy generated by Joule heating per unit volume goes as the product of the current squared and material resistivity divided by the cross-sectional area normal to the flow of current. The boundary conditions are $T = T_C$ at $x = 0$ and $T = T_H$ at $x = L$ and once applied, yield:

$$T = \frac{-I^2 \rho}{2kA^2}x^2 + \left(\frac{I^2 \rho L}{2kA^2} + \frac{T_H - T_C}{L}\right)x + T_C \qquad (2.3)$$

By conventional standards, thermal conductance $(K)$ and electrical resistance $(R)$ are defined as:

$$R = \frac{2\rho L}{A} \qquad (2.4)$$

$$K = \frac{2kA}{L} \qquad (2.5)$$

Recall that the thermocouple legs are thermally in parallel and electrically in series, thus the thermal conductance and electrical resistance for a pair both have factors of two.

The heat flow across a boundary where thermoelectric phenomena is present takes a slightly different form than heat flux at a typical boundary (assuming electrical current is also flowing across the boundary). Because the charge carriers change energy levels when crossing from one material into another, the Peltier heat, Eq.(1.7), must be represented in the heat flow at the boundary. The generic expression for the heat flow at a boundary between two materials (with arbitrary labels 1 and 2) is:

$$q_{in} = I\alpha_{1,2}T_{Boundary} + q_{out} \qquad (2.6)$$

where the overall Seebeck coefficient is the difference between the Seebeck coefficients of the materials at the boundary $\alpha_{1,2} = \alpha_1 - \alpha_2$ and $T_{Boundary}$ is the absolute temperature at the boundary. The expression for the heat flow at the hot-side interface of the basic analytical model takes the form:

$$q_H = I\alpha_{p,n}T_H + 2kA \left.\frac{dT}{dx}\right|_{x=L} \qquad (2.7)$$

The only heat leaving the interface is from the conduction through the two thermoelectric legs, thus the second term represents the heat conducted through the thermoelement legs assuming that they have the same material properties and geometries. From Eq.(2.3), the conduction term in Eq.(2.7) can be evaluated, since the temperature gradient is known. The $\frac{dT}{dx}$ term falls out and the energy balance at the respective surfaces can be used to determine heat transfer at each surface.

$$q_H = I\alpha_{p,n}T_H + K(T_H - T_C) - I^2 R/2 \qquad (2.8)$$

$$q_C = I\alpha_{p,n}T_C + K(T_H - T_C) + I^2 R/2 \qquad (2.9)$$

Electrical power generated by a thermocouple is the difference between the two surface heat transfer rates and is equal to the product of the current squared and the external

electrical load resistance, $R_{Load}$. A module with $N$ elements will produce a total power that can be expressed as $P_{TEM} = N \cdot P$. Or,

$$P_{TEM} = N(q_H - q_C) \tag{2.10}$$

$$P_{TEM} = IN\alpha_{p,n}\Delta T - I^2 R_{TEM} = I^2 R_{Load} \tag{2.11}$$

Note that this is the power of a whole module, and not just a single pair of thermoelements. This expression of output power differs from that of a single thermoelement simply by the term $R_{TEM} = N \cdot R$ which accounts for the number of thermocouples in a module. Likewise the thermal conductance for the thermoelectric module, $K_{TEM}$, is simply the conductance of the leg pair with a multiple of $N$.

Eq.(2.11) reveals that current can be expressed as:

$$I = \frac{N\alpha_{p,n}\Delta T}{R_{Load} + R_{TEM}} \tag{2.12}$$

By substituting Eq.(2.12) into Eq.(2.11), the electrical power output of a TEM may be expressed in terms of electrical resistance, the Seebeck coefficient, and the hot and cold side temperatures.

$$P_{TEM} = \frac{(N\alpha_{p,n}\Delta T)^2}{R_{Load} + R_{TEM}} - \frac{(N\alpha_{p,n}\Delta T)^2 R_{TEM}}{(R_{Load} + R_{TEM})^2} \tag{2.13}$$

Conversion efficiency follows as:

$$\eta = \frac{P_{TEM}}{q_H} \tag{2.14}$$

$$\eta = \frac{(N\alpha_{p,n}\Delta T)^2 R_{TEM}}{2(N\alpha_{p,n})^2 \Delta T T_H (R_{Load} + R_{TEM}) - 4K_{TEM}\Delta T(R_{Load} + R_{TEM})^2 - (N\alpha_{p,n}\Delta T)^2 R_{TEM}} \tag{2.15}$$

Optimal power occurs when the condition $\partial P_{TEM}/\partial R_{Load} = 0$ is achieved, which yields maximum power at $R_{Load} = R_{TEM}$. It is important to note that the value of $R_{Load}$ at maximum power differs noticeably from the value that meets maximum efficiency condition $\partial \eta/\partial R_{Load} = 0$. For the purposes of simplicity of comparison, the different models will be evaluated at the maximum power condition $R_{Load} = R_{TEM}$.

The geometric optimization using this particular analytical model yields erroneous results. Because this model neglects contact resistances, linear optimization of this efficiency will report that ideal geometric design requires very short legs. However, as Rowe and Min reported , contact resistances become dominant as leg length decreases [12]. It is imperative that these effects be factored in when optimizing pellet length.

## 2.2 One-Dimensional Thermoelectric Module Model with Contact Resistances

Rowe and Min [12] offer a slightly more advanced approach to modeling TEMs. The basic assumptions for the new model are similar to those described by Hodes' work, with the exception of included electrical and thermal contact resistances between the pellets and the electrical connector. These contact effects are essential for optimization, because as leg lengths become small, the contact resistances will become increasingly prominent.

The equations of module performance are nearly the same as the basic 1-D model, except that resistance ($R$) would have a component related to the internal resistance of the module, and a component associated with the contact resistances between the legs *and* the adjoining electrical interconnect material, typically a copper film.

Voltage and current of a module at maximum power output (matched load condition) can be expressed, with both internal and contact resistances, as:

$$V_{TEM} = \frac{N\alpha_{p,n}(T_H - T_C)}{1 + 2rL_c/L} \tag{2.16}$$

$$I = \frac{\alpha_{p,n}A(T_H - T_C)}{2\rho(n + L)(1 + 2rL_c/L)} \tag{2.17}$$

where $N$ is the number of thermocouples, $A$ and $L$ are the cross-sectional area and length of the thermoelement, $L_c$ is the thickness of the contact layer, $T_H$ and $T_C$ are the hot and cold side temperatures respectively. $n = 2\rho_c/\rho$, $r = k/k_c$ where the subscript "$c$" denotes the respective characteristic of the contact layer.

Using this definition, power and efficiency become:

$$P_{TEM} = \frac{AN\alpha_{p,n}{}^2(T_H - T_C)^2}{2\rho(n + L)(1 + 2rL_c/L)^2} \tag{2.18}$$

$$\eta = \left(\frac{T_H - T_C}{T_H}\right)\left((1 + 2rL_c/L)^2\left[2 - \frac{1}{2}\left(\frac{T_H - T_C}{T_H}\right) + \left(\frac{4}{ZT_H}\right)\left(\frac{L + n}{L + 2rL_c}\right)\right]\right)^{-1} \tag{2.19}$$

The economic factor (a product of the conversion efficiency and the power generated per unit area) was compared to element length. For the case that Rowe and Min explore, a commercial Bismuth-Telluride TEM, optimization techniques yield an ideal element length of just under one millimeter.

Additionally, a comparison was done between contact effects to examine the impact of minimizing contact resistances. The results, Fig.(2.4), indicated that the largest factor for effecting overall system performance was thermal contact resistance. The power density and efficiency plots demonstrate that altering the ratio of contact resistance to bulk pellet resistance shifts the curves more dramatically than altering the electronic resistance ratio.
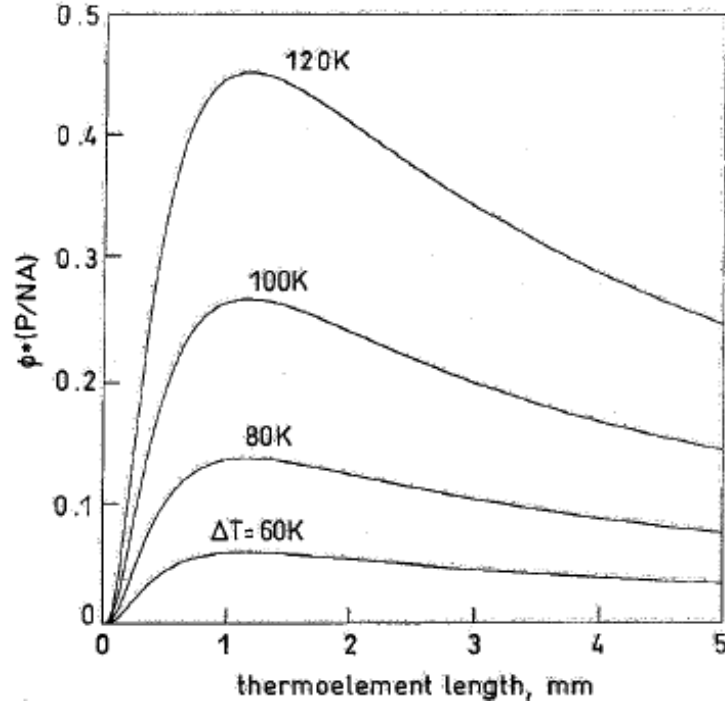
Figure 2.3: Product of power output per unit area and conversion efficiency as a function of thermoelement length [12]

Comparably, altering the overall material properties had less of an effect on the overall system performance. Altering both the bulk thermal and electrical conductivities by a factor of two only altered the overall system performance by about twenty percent, Fig.(2.5). Conversely, Fig.(2.3) indicates that altering the thermal contact resistance by a factor of two led to a performance change of a factor of two.

## 2.3 One-Dimensional Thermoelectric Module Model with Thomson Effect

So far, both TEM models have assumed that the Seebeck coefficient does not vary perceptibly with temperature, and have thus excluded the Thomson effect from their analysis. Chen et al. venture to examine a model that includes the Thomson effect, and determine a material-property threshold criteria for neglecting the Thomson effect [13]. Assumptions in this model include negligible contact resistances, and 1-D, steady state heat flow. In their analysis it is also assumed that the material properties have fixed values, although a constant Thomson coefficient is prescribed. Additionally, the Seebeck coefficient at the hot side, $\alpha_H$, has a different value than the Seebeck coefficient on the cold side, $\alpha_C$ where:

$$\alpha_i = (\alpha_p - \alpha_n)|_i \qquad i = H, C \qquad (2.20)$$

The heat diffusion is examined in both legs (prescribed as n-type leg and p-type leg) with the Thomson effect incorporated into the overall equation.

(a) Thermal Contact

(b) Electrical Contact
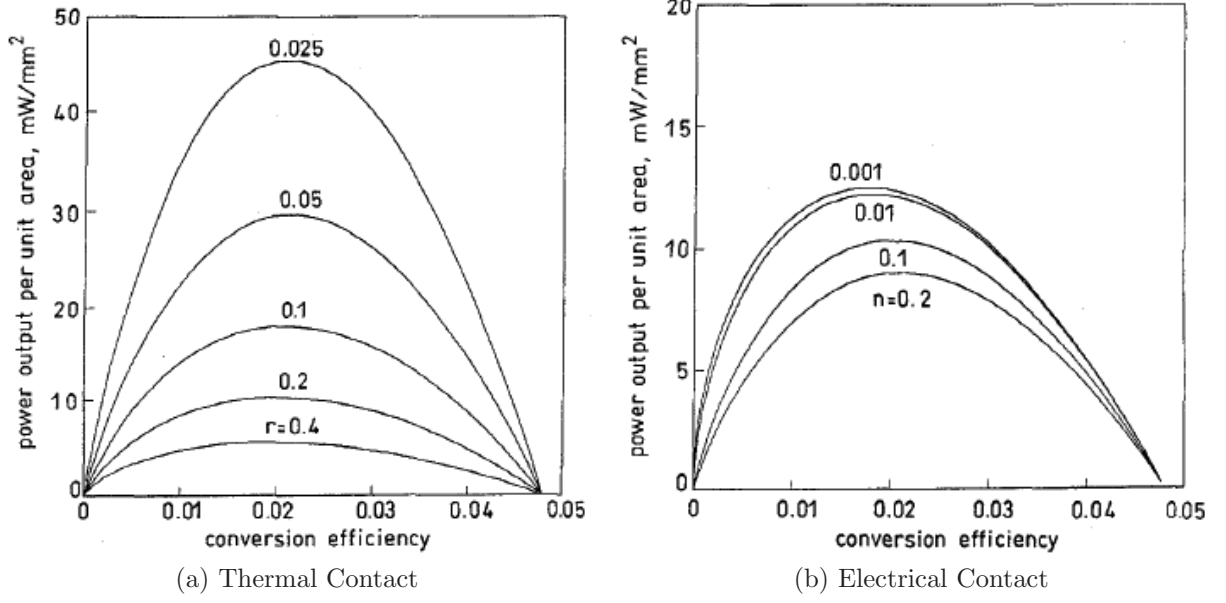
Figure 2.4: Power density vs. conversion efficiency for different contact properties (a) thermal (b) electrical [12]

$$K_n L_n \frac{d^2 T}{dx^2} - \tau_n I \frac{dT}{dx} + \frac{R_n I^2}{L_n} = 0, \ 0 \leq x \leq L_n, \qquad (2.21)$$

$$K_p L_p \frac{d^2 T}{dx^2} + \tau_p I \frac{dT}{dx} + \frac{R_p I^2}{L_p} = 0, \ 0 \leq x \leq L_p, \qquad (2.22)$$

Applying standard boundary conditions:

$$T_n(0) = T_p(0) = T_C, \qquad (2.23)$$

$$T_n(L_n) = T_p(L_p) = T_H, \qquad (2.24)$$

$$q_C = \alpha_C T_C I + K_n L_n \frac{dT_n}{dx}\bigg|_{x=0} + K_p L_p \frac{dT_p}{dx}\bigg|_{x=0}, \qquad (2.25)$$

$$q_H = \alpha_H T_H I + K_n L_n \frac{dT_n}{dx}\bigg|_{x=L_n} + K_p L_p \frac{dT_p}{dx}\bigg|_{x=L_p}, \qquad (2.26)$$

where $K_n = k_n A_n / L_n$, $K_p = k_p A_p / L_p$, $R_n = L_n / (\sigma_n A_n)$, and $R_p = L_p / (\sigma_p A_p)$ are the thermal conductances and electrical resistances of the n-type and p-type semiconductor elements respectively. The subscript $H$ corresponds to hot-side parameters, while the subscript $C$ relates to cold-side parameters. For the purposes of this investigation, $L_n = L_p = L$.

Following a similar procedure outlined in the section covering 1-D analytical solution of a TEM model, the temperature profile can be found using the boundary conditions. With the temperature profile, the $\frac{dT}{dx}$ terms can be evaluated in Eq.(2.25) and Eq.(2.26). Net power

15
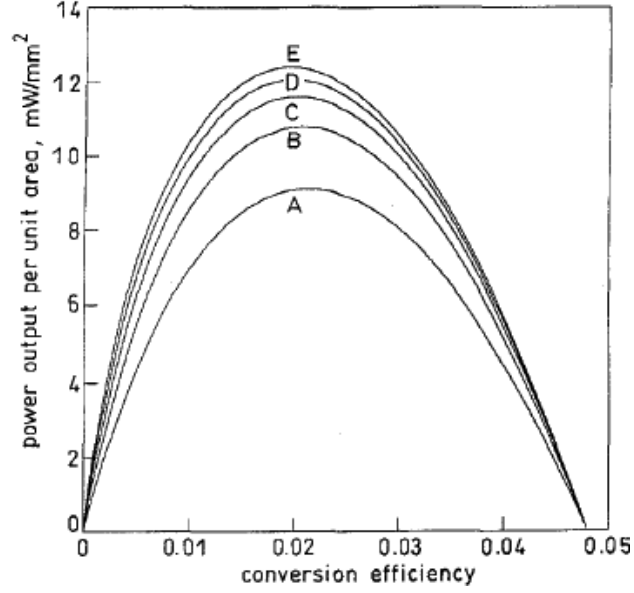
Figure 2.5: Effect of altering bulk material properties on system performance. [12]

A: $\lambda = 0.5 W/mK; \alpha^2\sigma = 15 \cdot 10^{-4} W/mK^2$
B: $\lambda = 1.0 W/mK; \alpha^2\sigma = 30 \cdot 10^{-4} W/mK^2$
C: $\lambda = 1.5 W/mK; \alpha^2\sigma = 45 \cdot 10^{-4} W/mK^2$
D: $\lambda = 2.0 W/mK; \alpha^2\sigma = 60 \cdot 10^{-4} W/mK^2$
E: $\lambda = 2.5 W/mK; \alpha^2\sigma = 75 \cdot 10^{-4} W/mK^2$

produced by the thermoelectric generator can then be expressed as:

$$P_{TEM} = N(q_H - q_C) = N(\alpha_H T_H - \alpha_C T_C)I - \tau_{TEM}(T_H - T_C)I - I^2 R_{TEM} \qquad (2.27)$$

And likewise efficiency can be expressed as:

$$\eta = 1 - \frac{q_C}{q_H} = \frac{(\alpha_H T_H - \alpha_C T_C)I - \tau(T_H - T_C)I - RI^2}{\alpha_H T_H I + (K_1^* + K_2^*)(T_H - T_C) - \tau(T_H - T_C)I + (R_1^* + R_2^* - R)I^2} \qquad (2.28)$$

with $R = R_n + R_p$, $\tau = \tau_p - \tau_n$, $K_n^* = \tau_n I/[exp(\omega_n L) - 1]$, $K_p^* = \tau_p I/[1 - exp(-\omega_p L)]$, $R_n^* = R_n(1/(\omega_l L) - 1/[exp(\omega_n L) - 1])$, $R_2^* = R_p(1/[1 - exp(-\omega_p L)] - 1/(\omega_p L))$, $\omega_n = \tau_n I/(K_n L)$, and $\omega_p = \tau_p I/(K_p L)$.

Clearly, the expression for efficiency is complex and difficult to analyze. Chen et al. examine a particular case where they assume $(\tau_p I/K_p)^2 \ll 1$, $(\tau_n I/K_n)^2 \ll 1$. This assumption holds true for the material properties of some of the commercially available thermoelectrics. Collapsed parameter values can be expressed as:

$$K_p^* = K_p\left(1 - \frac{\tau_p I}{2K_p}\right) K_n^* = K_n\left(1 + \frac{\tau_n I}{2K_n}\right) R_p^* = \frac{R_p}{2}\left(1 + \frac{\tau_p I}{6K_p}\right) R_n^* = \frac{R_n}{2}\left(1 - \frac{\tau_n I}{6K_n}\right)$$
$$(2.29)$$

Chen et al. have defined a method for analyzing TEM efficiency while incorporating

the Thomson effect. One disadvantage to this model, however, is that all of the analysis is predicated on the assumption that the material properties remain constant with temperature, except for the Seebeck coefficient. As described later, this assumption can lead to errors for materials with properties that are heavily temperature dependent. The Seebeck coefficient is assumed to be be logarithmic with respect to temperature, and thus yields a constant Thomson coefficient. Typical functions for describing the Seebeck coefficient are polynomial, and yield a heavily temperature-dependent Thomson coefficient, as seen in the Appendix and the section labeled "The Thomson Effect Revisited".

## 2.4   Improved Analytical Thomson Effect Model

A further expansion of the Thomson model made by Freunek et al. [14] implements a linearization of the Seebeck coefficient in addition to both thermal and electrical contact resistances. The same governing heat equations and boundary conditions seen in Eqs.(2.21-2.24) are implemented for the thermoelement legs in this model. A thermal resistance due to the ceramic interface is accounted for, as well as electrical contact resistances between the legs.
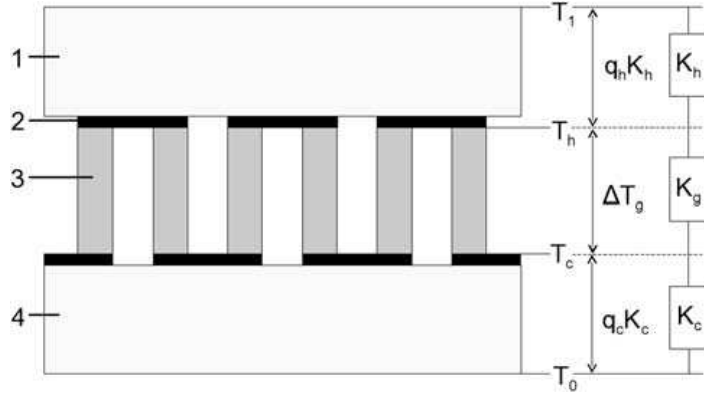


Figure 2.6: TEM. 1-Ceramic Interface (Hot), 2-Conducting Strip, 3- Thermoelement Legs, 4-Ceramic Interface (Cold). Note that $K$ in this analysis represents a thermal resistance, instead of conductance [14]

Because of the additional contact resistances, the heat flow equations into and out of the thermoelement junction are altered in two ways. First, the temperatures in the Peltier heat term are changed to be the temperatures at the legs and not the temperature at the interfaces since there is a thermal resistance in between, as seen in Fig.(2.6). Secondly, a boundary generation term representing the Joule heating due to the contact resistance at the hot side ($R_{ch}$) and cold side ($R_{cc}$) has been added. The new boundary heat flow terms are:

$$q_h = k_n L_n \frac{dT_n}{x}\bigg|_{x=L_n} + k_p L_p \frac{dT_p}{x}\bigg|_{x=L_p} + I T_h \alpha_{p,n} - I^2 R_{ch} \tag{2.30}$$

17

$$q_c = k_n L_n \frac{dT_n}{x}\bigg|_{x=0} + k_p L_p \frac{dT_p}{x}\bigg|_{x=0} + I T_c \alpha_{p,n} + I^2 R_{cc} \qquad (2.31)$$

Using Eq.(1.5) and the fact that the Thomson coefficient $\tau$ is constant, Freunek et al. express the electrical current through a thermoelectric as:

$$I = \frac{(\alpha(T_0) + \frac{\tau}{T_0}K_c q_c)\Delta T_g + \frac{\tau}{2T_c}\Delta T_g^2}{R_g + R_{Load}} = \frac{(\alpha(T_1) - \frac{\tau}{T_1}K_h q_h)\Delta T_g - \frac{\tau}{2T_h}\Delta T_g^2}{R_g + R_{Load}} \qquad (2.32)$$

where $T_0$, $T_1$, $K_c$, and $K_h$ are the cold-side temperature, hot-side temperature, cold-side thermal interface and hot-side thermal interface respectively. The overall generator electrical resistance can be represented as $R_g = R_{Leg} + R_{cc} + R_{ch}$. The Thomson coefficient is defined as $\tau = \tau_p - \tau_n$.

After solving the temperature profile in the legs, the flux terms can be approximated (by assuming $\tau I/K \ll 1$, a reasonable assumption using commercial thermoelectric material properties, the exponentials are simplified) as:

$$\begin{aligned}
q_h = \ & \frac{R_g + R_{Load}}{R_g + R_{Load} + \Delta T_g \alpha(T_1) K_h (2\tau + \alpha(T_1))} \\
& \times \left( \frac{\Delta T_g}{K_g} + \frac{\alpha^2(T_1) T_1 \Delta T_g}{R_g + R_{Load}} - \frac{\Delta T_g^2 \alpha(T_1)(\tau + (1-\epsilon)\frac{R_g \alpha(T_1)}{R_g+R_{Load}})}{R_g + R_{Load}} \right)
\end{aligned} \qquad (2.33)$$

$$\begin{aligned}
q_c = \ & \frac{R_g + R_{Load}}{R_g + R_{Load} - \Delta T_g \alpha(T_0) K_c (2\tau + \alpha(T_0))} \\
& \times \left( \frac{\Delta T_g}{K_g} + \frac{\alpha^2(T_0) T_0 \Delta T_g}{R_g + R_{Load}} + \frac{\Delta T_g^2 \alpha(T_0)(\tau + (1+\epsilon)\frac{R_g \alpha(T_0)}{R_g+R_{Load}})}{R_g + R_{Load}} \right)
\end{aligned} \qquad (2.34)$$

The simplification is made with a new parameter to describe the distribution of the Joule heat:

$$\epsilon = \frac{\frac{1}{2}R + R_{cc}}{R + R_{cc} + R_{ch}} \qquad (2.35)$$

Finally, using the relationship between the temperature difference across the leg and the temperature difference across the module, $\Delta T = \Delta T_g + K_c q_c + K_h q_h = T_1 - T_0$, the temperature across the legs can be solved for by utilizing Eqs.(2.34-2.35).

$$\Delta T_g = \Delta T \left( 1 + \frac{K_c}{K_g} + \frac{K_h}{K_g} + \frac{2\tau \Delta T (K_c \alpha(T_0) - K_h \alpha(T_1))}{R_g + R_{Load}} + \frac{\alpha^2(T_0) K_c T_1 + \alpha^2(T_1) K_h T_0}{R_g + R_{Load}} \right)^{-1} \qquad (2.36)$$

It is important to note that several Taylor series linearizations were required to simplify
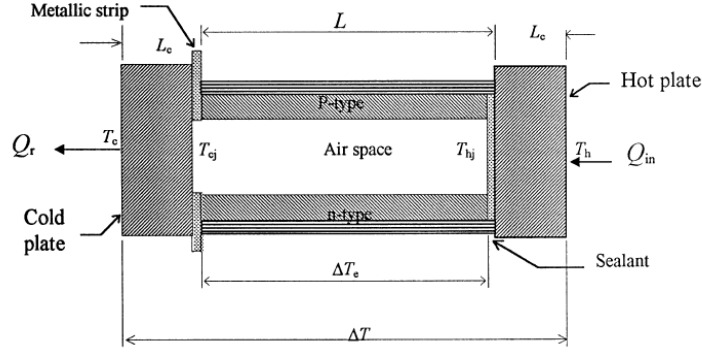
Figure 2.7: A thermopile with air space and ceramic insulation along the legs[15]

these systems of equations, and an approximation was used to simplify the exponential terms in the temperature profile. The appendix contains descriptions of this analysis. The system of equations described above can be used to calculate the performance of a TEM with an approximation of the Thomson coefficient as a temperature-independent term. The validity of this assumption is explored in a later section.

## 2.5    Thermoelectric Module Model with Heat Leakage

One significant source of inefficiency in a TEM is heat leakage. If a significant portion of heat transmits through the TEM without being absorbed and converted to electricity by the Seebeck effect, the module efficiency decreases, since it 'wastes' heat by allowing it to pass through without conversion. This is why the figure of merit, $ZT$, is inversely proportional to thermal conductivity, Eq.(1.1). This model, however, assumes that thermal conduction through the thermopile is the only form of heat leakage. In fact, there are gaps between thermopiles that could permit significant radiative and conductive heat transfer between the hot side and the cold side of the TEM. An improved model, which accounts for fluid and radiative heat leakage, was developed by Omer and Infield, as depicted in Fig.(2.7)[15]. As it stands, the model is flawed because of mistakes in the heat flow analysis and cannot be used in its current form. In a later section, the heat leakage is correctly implemented in a new analytical model and the role of heat leakage in module performance is evaluated.

The improved model proposed by Omer and Infield accounts for the air space between the hot and cold substrates. At high temperatures, the magnitude of heat leakage due to radiation could easily approach that of the heat leakage due to conduction through the thermopile. Additionally, some TEMs have an insulation layer of ceramic along the outside of each thermocouple leg that could provide another conduction route for heat leakage.

The energy balance described by Omer and Infield at the hot junction has the following incorrect form.

$$q_h = q_{Cond} + q_{Peltier} + q_{Rad} + q_{Air} + q_{Seal} - \frac{1}{2}q_t - \frac{1}{2}q_j \qquad (2.37)$$

where $q_h, q_{Cond}, q_{Peltier}, q_{Rad}, q_{Air}, q_{Seal}, q_t, q_j$ are the heat flow into the TEM at the hot side interface, the heat flow by conduction through thermoelement legs, the Peltier heat (or heat absorbed due to the Seebeck effect), the heat transfered by radiation in the gap between the thermopile, the heat transfered by convection in the gap, the Thomson heat, the Joule heat, the heat leakage via the space and the heat leakage via the sealant ceramic material to the cold junction.

The first mistake made in this model is in Eq.(2.37), and is merely a semantic error, but could lead to mathematical errors if not corrected. The terms $q_t$ and $q_j$, which represent the Joule and Thomson heats, are accounted for in the conduction term, $q_{cond}$, because the temperature profile (which is used in the conduction to determine $\frac{dT}{dx}$) contains the heat distributed by the Joule and Thomson effects. The equation should read:

$$q_h = q_{Cond} + q_{Peltier} + q_{Rad} + q_{Air} + q_{Seal} \tag{2.38}$$

since the Thomson and Joule heat terms are redundant.

The heat flow is assumed to be 1-D, and thus no heat leakage occurs through the sides of the TEM. Additionally, the fluid bulk properties of the air in the space between the hot-side and cold-side junctions are assumed to be at the mean temperature $T_m = 0.5(T_h + T_c)$.

Simultaneously, this model accounts for electrical and thermal contact resistances. Each of the two junction layers contributes a contact resistance and the total thermopile resistance can be expressed as follows:

$$r = 2r_c + 2\rho\frac{L}{A} = \frac{2\rho}{A}\left(\frac{r_c A}{\rho} + L\right) = 2\rho(\rho_{oc} + L)/A \tag{2.39}$$

where $\rho_{oc} = \frac{\rho_c}{\rho}$, and the quantity $\rho_c = r_c A$ characterizes the quality of the junction. Taking all resistances into account, the overall heat flow through the module, $q$, is represented (incorrectly) as:

$$q = \sum R_{th}^{-1}(T_h - T_c) \tag{2.40}$$

where $\sum R_{th}$ is the total thermal resistance through the thermoelectric module. This assumes that the heat flow through the module is constant, which is only true if there is no electrical load (open circuit condition). However, this is not true for the behavior of an active thermoelectric generator. A simple examination of the heat flowing into the module and heat flowing out of the module (as seen in Fig.(2.1) demonstrates that the flow is variable throughout the thermoelement leg. This is also clear because $q_H \neq q_C$. The overall resistance, including all forms of bypass heat leakage, is lumped into the parameter $U$, which is defined as:

$$U = 1 + k_{os}A_{os} + k_{og}A_{og} + \frac{\epsilon_{EM}\sigma_{SB}A_{og}}{2 - \epsilon_{EM}}(T_{hj}^2 + T_{cj}^2)(T_{hj} + T_{cj}) \tag{2.41}$$

where $k_{os}$, $k_{og}$ are, respectively, the ratios of thermal conductivity of the sealant, and the
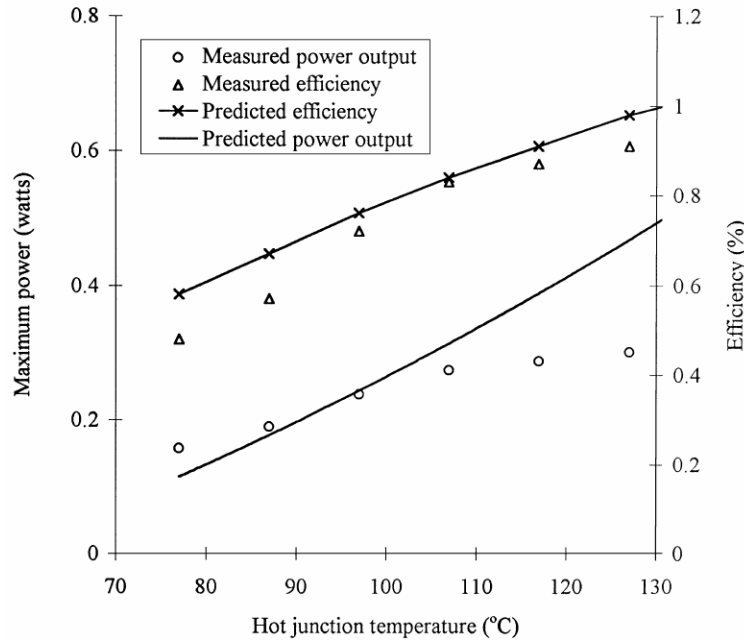
Figure 2.8: Power and Efficiency of the Model vs. Experimental Data [15]

thermal conductivity of the air in the gap to the thermal conductivity of the thermoelement. The terms $\epsilon_{EM}$ and $\sigma_{SB}$ are the emissivity and Stefan-Boltzmann constant respectively. $A_{os}$ and $A_{og}$ are the ratios of the cross-sectional areas of the sealant and the gap to the cross-sectional area of the thermoelement. $T_{hj}$ and $T_{cj}$ are the hot and cold side temperatures of the thermoelement.

The derivation for $P_{TEM}$ and $\eta_{TEM}$ differ from the previous models only in accounting for this additional $U$ term, but the results vary greatly. The derivation for the expressions is lengthy and needs slight corrections. The concept behind this model is implemented later in section 3.1, and detailed account of the authors' derivation can be found in [15].

The results shown in Fig.(2.8) for predicted efficiency and power output vs. experimental data shows some deviation. It is unclear whether this discrepancy is a fault of the model or because the experimental arrangement which was not designed to characterize thermoelectric modules but instead determine their performance under a specific radiative heat load (to simulate solar radiation for power generation). Further discussion on the results of this model is made in the following section.

## 2.6  Review of Previous Work

The aforementioned analytical techniques have been implemented and validated with varying degrees of success. The simple 1-D model is valuable for estimating the ideal behavior of a thermoelectric device, but cannot be used as a model for comprehensive geometric optimization of a device. Because contact resistances are neglected, the simple 1-D model will report that an infinitely small leg will yield the highest power output of a module [12].

Additionally, the impact of electrical contact resistance is not fully understood. Electrical

contact resistances, particularly those associated with soldered joints as in the case with many TEMs, are difficult to quantify. The impact of the contact resistance on TEM performance can be large, but because the contact resistance is used as a fitting parameter between models and experimental data [16], the size of the resistance and its impact is ambiguous.

As mentioned earlier, the the model that accounts for the Thomson effect proposed by Chen et al. makes the simplification that the Thomson coefficient is independent of temperature for the sake of treating the governing equations as an ordinary differential equation. Additionally, their model is not experimentally validated. This does not fully capture the contribution of the Thomson effect to the overall system performance. With large temperature gradients, or Seebeck coefficients that are highly temperature sensitive, the Thomson coefficient will change dramatically and increase the amount of heat generated or absorbed by this effect throughout the module.

The heat leakage model proposed by Omer and Infield is slightly more comprehensive, though some of the assumptions need to be reevaluated. The effective temperature across the thermoelements is calculated by making the incorrect assumption that the total heat flow through the thermoelectric module is simply the temperature difference between the hot side and cold side of the module, divided by the overall module thermal resistance. This model, however, is the only model to account for other forms of heat leakage and may prove to be accurate at high temperature gradients where this bypass heat may become more prevalent. Further examination of this model is warranted.

Freunek offers an improvement on the constant Thomson coefficient by accounting for thermal interface resistances. This model is comprehensive, and makes few assumptions, but is still limited by assuming a constant Thomson coefficient. The beginning stages of this model are explored in the section "Thomson Effect Revisited".

## 2.7 Numerical Modeling

When analytical solutions are difficult or impossible to derive, numerical techniques can be a powerful alternative. As it stands, analytical solutions to thermoelectric systems require making broad assumptions. Already, discrepancies have arisen that indicate that making some of these assumptions for an analytical solution is inappropriate [10],[11]. Models that assume that material properties as temperature-independent, or that the resistances between the thermoelement and the hot and cold sides are negligible, or neglecting the Thomson effect have all been shown to be inadequate in many scenarios.

Rodriguez, et al. implemented numerical techniques to model thermoelectric behavior, though the Thomson effect and stray heat leakage were neglected [17]. Additionally, Hirano et al., El-Genk et al., and Lau et al. utilized numerical techniques for the purposes of modeling functionally graded or segmented thermoelectrics to some success [18],[19],[9].

Recent advances in multiphysics coupling in commercial software have made finite element packages, such as ANSYS, competitive with finite difference techniques tailored for
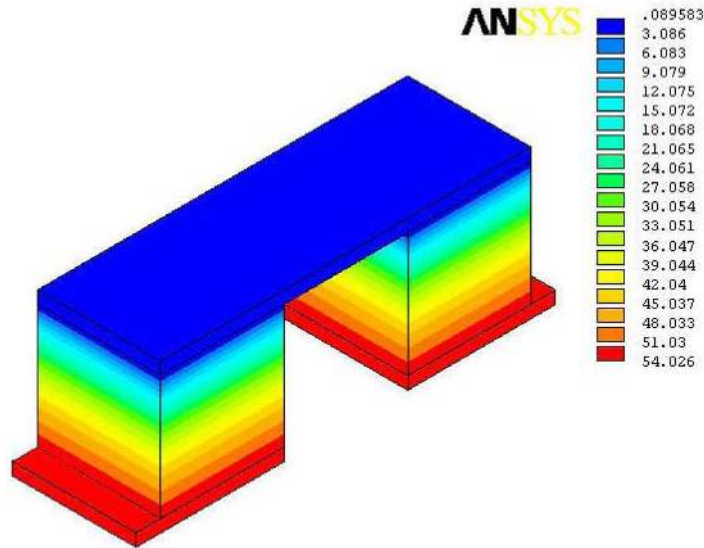
Figure 2.9: Temperature profile of a thermopile cooler in ANSYS[11]

thermoelectric analysis [11]. These new advances couple the Thomson and Peltier effect electrically and thermally. In the past, only Joule heating has been accounted as a coupled effect in the ANSYS package. Using the ANSYS finite element package, Antanova was able to produce temperature profiles of a Peltier cooler, as can be seen in Fig.(2.9). In addition, the performance of a TEM for the purposes of power generation was evaluated.

Because of their ease of implementation, and their robust nature, these packages have become desirable as modeling tools to replace cumbersome numerical techniques. Additionally, new geometrical configurations can easily be explored, thus the models are no longer limited to rectangular, 1-D analysis. Some finite element packages allow for physical models to be added for more complex analysis as well as allowing temperature dependent and spatially dependent properties.

# Chapter 3

# Improved Analytical Models

This section will address previously-neglected effects by integrating them into a robust analytical model. Thermal contact resistance, heat leakage and the approximated Thomson coefficient are all examined and explored for relative impact on TEM performance. In addition, the underlying assumptions are explicitly stated and their limitations are explored.

To quantitatively compare the different models and the relative impact of certain effects, the module output power $P_{TEM}$ and module efficiency $\eta$ are invoked. In some cases, it is prudent to compare maximum power output $P_{Max}$ of some models, as described in section 2.1.

The module parameters used for model comparison can be seen in Fig.(3.1) and their corresponding nominal values can be seen in Table 3.1. These parameters came from a Melcor HT6-12-40-W6, a commercial $Bi_2Te_3$ module. The Melcor module was selected as a benchmark due to its availability and likeness to many other commercial modules. The material properties of the electrical contact and ceramic interface were provided, and the dimensions of the module were measured.

Table 3.1: Parameters of a Thermoelectric Module

| Parameter | Value | Symbol |
|---|---|---|
| Leg Height | 1.092 [mm] | $L$ |
| Leg Width | 1.397 [mm] | $W$ |
| Leg Spacing | 1.016 [mm] | $D$ |
| Copper Thickness | 0.318 [mm] | $t_{Cu}$ |
| Ceramic Thickness | 0.787 [mm] | $t_{Cer}$ |
| Solder Thickness | 0.140 [mm] | $t_{Solder}$ |
| Ceramic Thermal Conductivity | 27 [W/mK] | $k_{Cer}$ |
| Copper Thermal Conductivity | 400 [W/mK] | $k_{Cu}$ |
| Copper Electrical Conductivity | $6 \cdot 10^7$ [S/m] | $\sigma_{Cu}$ |
| Number of Leg Pairs | 127 | $N$ |
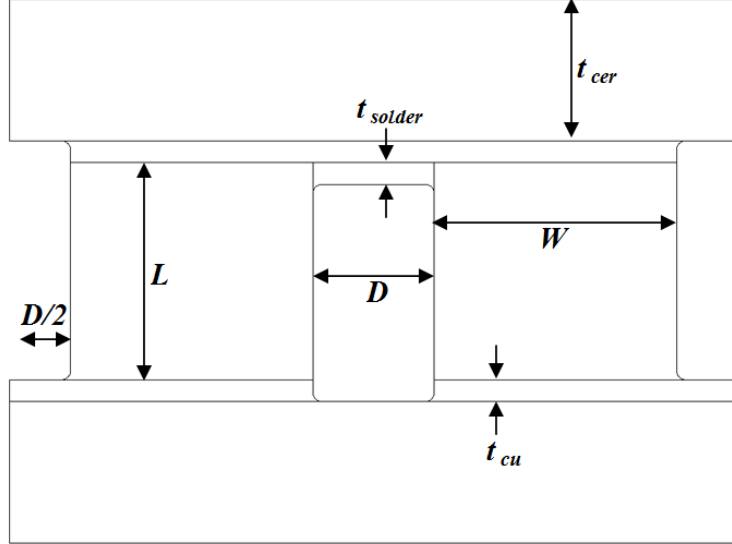
Figure 3.1: Parameters of a TEM for modeling. The copper contacts and solder are not modeled in the 1-D analytical models, and likewise the leg spacing is not a parameter that the 1-D models account for

## 3.1 Heat Leakage and Contact Model

The standard 1-D model serves as an excellent foundation for describing thermoelectric material behavior; however, it neglects certain module-level facets that can significantly impact TEM performance.

Typically a thermal interface material, such as a ceramic wafer, provides electrical insulation for the junctions. Consequently, the temperature difference across the legs will always be lower than predicted by the standard 1-D model. TEM models must account for the temperature drop across the interface materials for accurate design and system integration [12]. An implicit set of equations is established when the thermal resistances before and after the module are accounted for:

$$q_H = \frac{T_H - T_{HE}}{R_{Cer}} \tag{3.1}$$

$$q_C = \frac{T_{CE} - T_C}{R_{Cer}} \tag{3.2}$$

where $T_{HE}$ and $T_{CE}$ are the temperatures of the hot-side and cold-side of the thermoelectric legs, $R_{Cer}$ is the thermal resistance of the ceramic plates covering the junction, assuming the hot-side and cold-side ceramic interfaces have identical thicknesses and thermal conductivities as seen in Fig.(3.2).

TEM design can lead to additional forms of heat leakage, which diminishes module efficiency. Heat that is conducted from the hot side to the cold side of a module cannot be converted into electricity, and is thus considered a parasitic loss. In most TEMs, the gap between the hot and cold side interfaces contributes to this heat leakage by conduction through
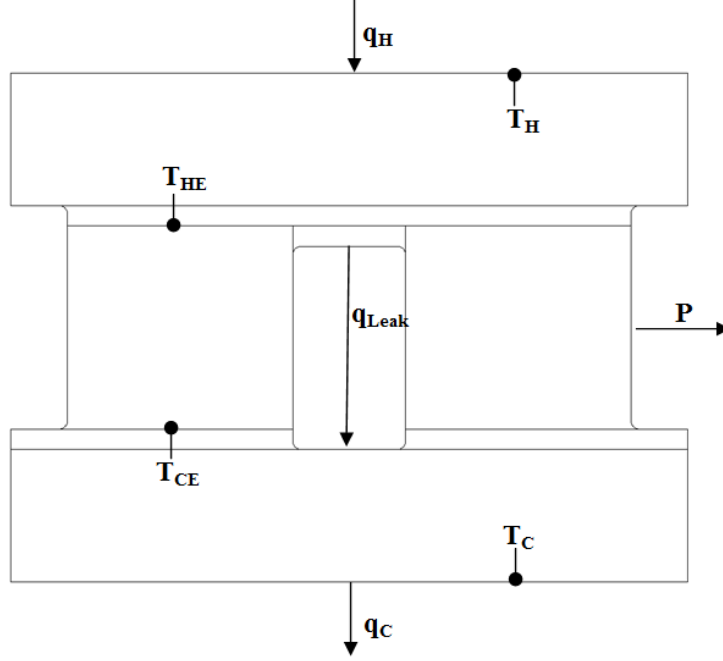
Figure 3.2: Diagram of a thermoelectric couple as addressed by the improved analytical model

the air and by thermal radiation. Accounting for this additional heat leakage, the heat rate at the bottom edge of the ceramic plate is:

$$
\begin{aligned}
q_H =\ & IN\alpha_{p,n}T_{HE} - \frac{I^2 R_{TEM}}{2} \\
& + \left( \frac{N}{R_t} + \frac{k_{Air}NA_{Gap}}{L} + \frac{\epsilon\sigma_{SB}NA_{Gap}}{2-\epsilon}(T_{HE}^2 + T_{CE}^2)(T_{HE}+T_{CE}) \right)(T_{HE}-T_{CE})
\end{aligned}
\tag{3.3}
$$

where $k_{Air}$, $A_{Gap}$, $\epsilon$, $\sigma_{SB}$, $R_t$ are the conductivity of the air, the total cross-sectional area of the gap between the ceramic plates per leg pair, emissivity of the ceramic plate, the Stefan-Boltzmann constant and the thermal resistance of the thermoelements respectively. The heat leaving the cold-side is similar to that entering the hot-side except for a sign difference in the second term and the equivalent temperature in the first term.

$$
\begin{aligned}
q_C =\ & IN\alpha_{p,n}T_{CE} + \frac{I^2 R_{TEM}}{2} \\
& + \left( \frac{N}{R_t} + \frac{k_{Air}NA_{Gap}}{L} + \frac{\epsilon\sigma_{SB}NA_{Gap}}{2-\epsilon}(T_{HE}^2 + T_{CE}^2)(T_{HE}+T_{CE}) \right)(T_{HE}-T_{CE})
\end{aligned}
\tag{3.4}
$$

The thermal radiation shape factor assumes two finite parallel plates connected on both ends by perpendicular plates on either end, similar to the geometry created by the gap between two thermoelement legs. A constant, temperature-independent emissivity is assumed. The heat leakage terms do not impact the power produced by the TEM because they subtract out for $P_{TEM} = q_H - q_C$. However the power takes a slightly different form, due to the

equivalent temperatures, $T_{HE}$ and $T_{CE}$. The power production must account for the thermal resistance of the ceramic interface, and takes the form:

$$P_{TEM} = IN\alpha_{p,n}(T_{HE} - T_{CE}) - I^2 R_{TEM} \tag{3.5}$$

The efficiency of the module takes a very different form, since the heat flowing into the module, $q_H$, contains the terms for heat bypassing the thermoelements.

$$\eta = \frac{IN\alpha_{p,n}(T_{HE} - T_{CE}) - I^2 R_{TEM}}{IN\alpha_{p,n}T_{HE} - \frac{I^2 R_{TEM}}{2} + \left(\frac{N}{R_t} + \frac{k_{Air}NA_{Gap}}{L} + \frac{\epsilon\sigma_{SB}NA_{Gap}}{2-\epsilon}(T_{HE}^2 + T_{CE}^2)(T_{HE} + T_{CE})\right)(T_{HE} - T_{CE})} \tag{3.6}$$

Because the system of equations, Eqs. (3.1)-(3.5), are implicit, an iterative technique is required. The heat flows, $q_H$ and $q_C$ reference the equivalent temperatures, $T_{HE}$ and $T_{CE}$, and reciprocally the equivalent temperatures reference the heat flows. Once the heat flows are determined using an appropriate iterative numerical technique, efficiency and power are easily calculated.

To illustrate the respective impact of the ceramic substrate and the additional heat leakage, the improved model is compared to the standard 1-D model. To examine the relative impact of the heat leakage and the ceramic thermal resistance, three models are compared to the standard model. The first model accounts for both the thermal substrate resistance and heat leakage. The second model accounts only for the thermal substrate resistance and the third model accounts only for the heat leakage. Using Melcor's material properties (Appendix A5) and the prescribed module parameters (Table 3.1), the module power and the module efficiency, Fig.(3.3), for the various models are calculated.

Upon examination of the power predicted by the different models, depicted in Fig.(3.3), it appears as though the heat leakage has minimal effect on module performance, and that the ceramic interface adversely affects the module performance greatly. As could be expected, the heat leakage model predicts the same power output as the standard model, since there is no ceramic thermal resistance thereby causing $T_{HE} = T_H$ and $T_{CE} = T_C$. This, in turn, would cause Eq.(3.5) to be equal to Eq.(2.11).

The heat leakage does have an impact, albeit minimal (less than 1% error at peak power between the standalone ceramic thermal resistance model and the combined ceramic resistance and heat leakage model), on the power output when coupled with the ceramic interface. However, the impact of the heat leakage on the power output is dwarfed by the negative impact of the ceramic thermal resistance, which predicts a peak power that is 20% less than that predicted by the standard model.

The significant impact of heat leakage is more readily identified by examining the module efficiency. The standalone heat leakage model has a 4% error in peak efficiency when compared to the standard model, and likewise the coupled heat leakage and ceramic resistance model has a 4% error in peak efficiency when compared to the standalone ceramic resistance

(a) Power

(b) Efficiency

Figure 3.3: (a) Model comparison of power output and (b) efficiency. $T_H = 473K$, $T_C = 307K$, Melcor material properties from Appendix, parameters from Table 3.1

model. Again, the ceramic interface resistance is the dominant facet, with a 10% error in peak efficiency when compared to the standard model.

The same effects are examined at a higher temperature gradient ($T_H = 973K$ and $T_c = 440K$) using high temperature material properties provided by CRC Handbook (appendix A3 for p-type $CeFe_4Sb_{12}$ and A4 for N-Type $CoSb_3$) and the same module parameters, Table 3.1. The heat leakage is dependent on temperature, so sensitivity to the size of the experienced temperature gradient must be probed.

Evaluation of power output at the higher temperature gradient (and new material property values) revealed that the ceramic interface ($k_{Cer} = 27W/mK$, $t_{Cer} = 0.79mm$) diminished peak power by 35% when compared to the standard model, seen in Fig.(3.4). The heat leakage had virtually no impact on power output at all, in this scenario.

Again, when the module efficiency is analyzed, the impact of the heat leakage is seen, Fig.(3.4). The heat leakage introduces an error of 5% when the heat leakage standalone is compared to the standard model, and an error of 5% when the ceramic resistance standalone was compared with the combined ceramic resistance and heat leakage model. It is worth mentioning that these contributions to error are true for the models where a constant hot and cold side temperature are maintained. In reality, the hot and cold side temperatures will slightly decrease and increase respectively due to the heat leakage.

The heat leakage was assumed to have a radiative emissivity of 1, which is a "worst case scenario". In fact, ceramic has an emissivity on the order of 0.2, indicating that the calculated radiative heat leakage is as much as an order of magnitude larger than would actually occur. In light of this, the heat leakage is not considered a critical modeling component of these

(a) Power                                (b) Efficiency
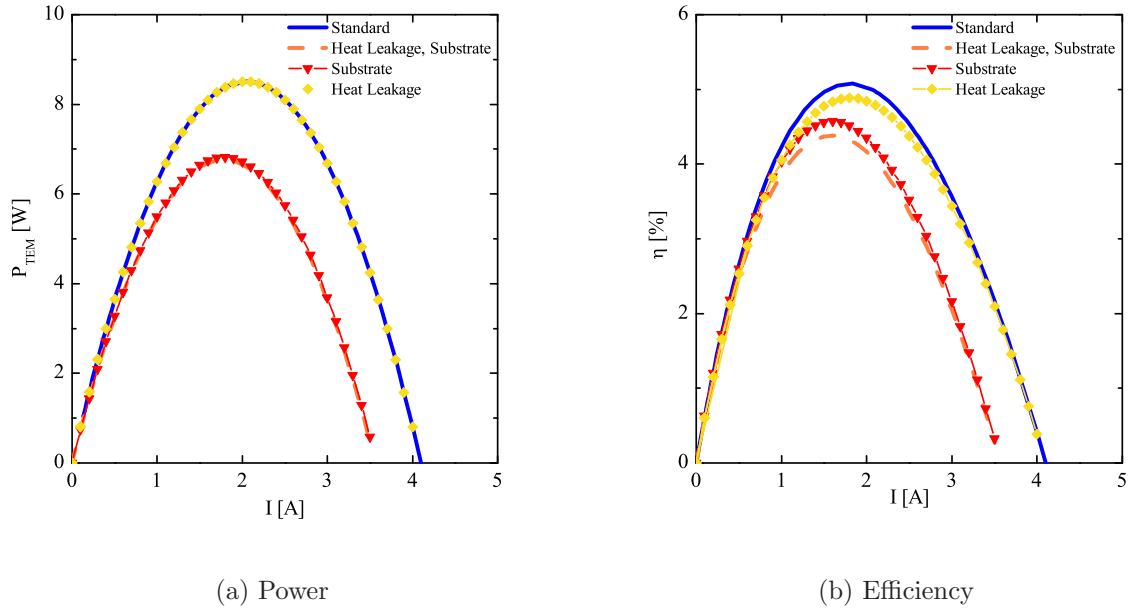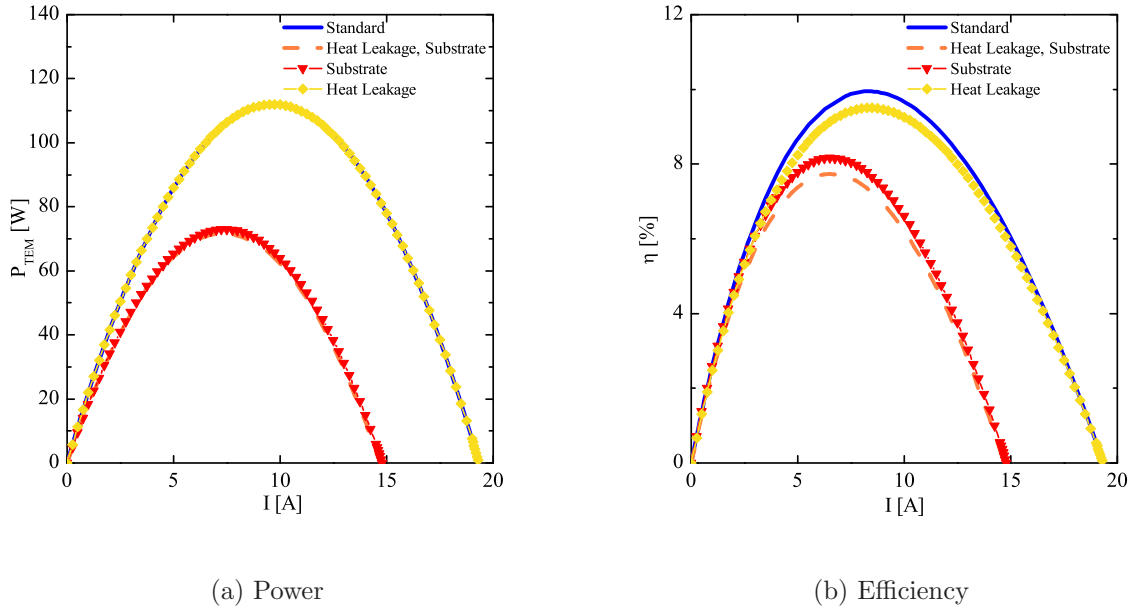
Figure 3.4: (a) Model comparison of power output and (b) efficiency. $T_H = 973K$, $T_C = 440K$, CRC material properties from Appendix (p-type CeFe$_4$Sb$_{12}$ and n-type CoSb$_3$), parameters from Table 3.1

TEMs.

## 3.2 Thomson Effect Revisited

Two analytical models in an earlier section accounted for the Thomson effect by assuming that it was temperature-independent. The validity of assuming the Thomson coefficient, $\tau$, is constant has not been probed by anyone, it has merely been assumed. In fact, both published and manufacturer's material data indicate that this assumption is inaccurate over large temperature gradients. In order for the Thomson coefficient to remain constant, the Seebeck coefficient, $\alpha$, must be a logarithmic function of temperature. This can be seen by invoking Eq.(1.9):

$$\int d\alpha = \tau \int \frac{1}{T} dT \tag{3.7}$$

$$\alpha = \tau \ln(T) + C \tag{3.8}$$

Because $\alpha$ must be a logarithmic function of temperature, the validity of the constant Thomson coefficient can be evaluated by examining a logarithmic curve fit if the Seebeck coefficient over a temperature range. There are some regimes where this assumption is appropriate, as seen in Fig.(3.5). The curve fit seen in Fig.(3.5) has the following form:

29

$$\alpha = -9.2769 \cdot 10^{-5} \ln(T) + 7.5186 \cdot 10^{-4} \ \ [\text{V/K}]$$

$$R^2 = 0.97828$$
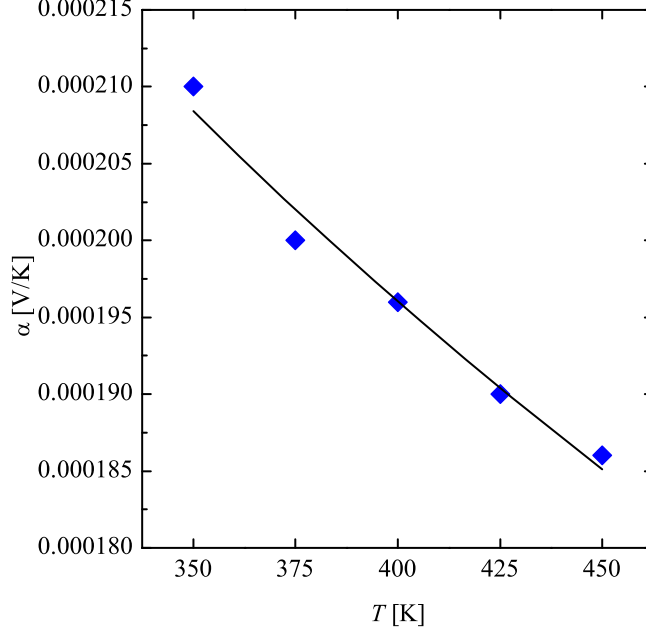


Figure 3.5: Melcor's Seebeck coefficient with logarithmic curve fit (appendix A5)

The curve fit above can provide a good estimate for the overall contribution of the Thomson coefficient. Because, in this particular case, the Thomson coefficient can accurately be estimated as constant, a single parameter value can be assigned. In this case, $\tau = -0.093[\text{mV/K}]$. Compared to the Seebeck coefficient, which over the same range has an integrated average value of $\alpha = 0.20[\text{mV/K}]$, the Thomson coefficient can contribute significantly to the performance of the system (it is 47% the size of $\alpha$).

Naturally, this has a significant impact on TEM performance. The Seebeck coefficient and Thomson coefficients are plotted against each other in Fig.(3.6). At any given temperature, the Thomson coefficient is at least 20% of the size of the Seebeck coefficient, and can get as large as 55%. Without a doubt, the Thomson effect is substantial, and should not be discounted in analysis. Additionally, the Thomson effect is sensitive to the temperature operating regime. In lower temperature ranges, the effect is beneficial, while in higher temperature ranges it is parasitic.

For other published thermoelectric material property data, the Thomson coefficient is not constant in any temperature regime, as seen in Fig.(3.7). This motivates the development of both a numerical model that can account for any material property temperature dependencies and also an analytical approximation of the non-linear Thomson coefficient term. In the next
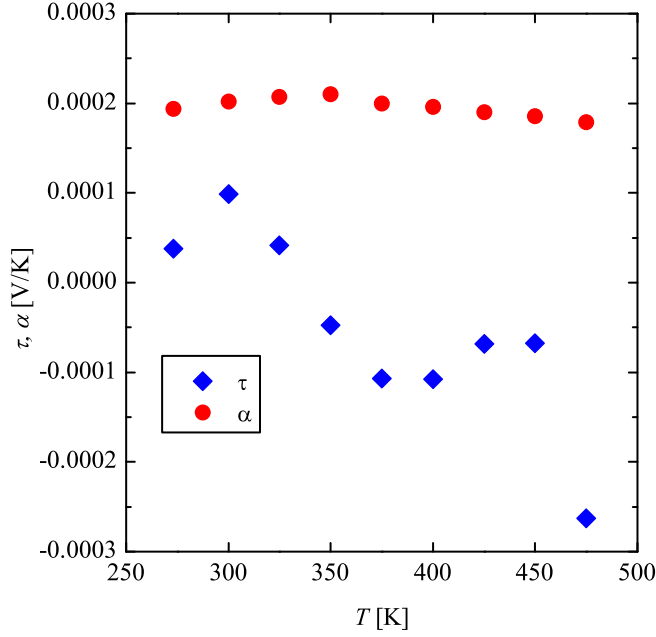
Figure 3.6: Melcor thermoelectric properties (appendix A5). $\tau$ calculated from a polynomial fit of $\alpha$

section, a novel analytical model is developed to approximate the non-linear behavior caused by the Thomson effect using asymptotic theory.

Any model that uses the integral of the Seebeck coefficient to determine the open-circuit voltage, as seen in Eq.(1.5), accounts for the Thomson effect by approximation. In the case where the Thomson coefficient is constant, the predicted power output of the standard model with an integral averaged Seebeck coefficient, and the predicted power output of the constant Thomson coefficient model are identical. Re-examining Eq.(2.11) with the Seebeck coefficient integral averaged, the power of the standard model takes the form:

$$P = I \int_{T_C}^{T_H} \alpha(T) dT - I^2 R \tag{3.9}$$

Assuming the Thomson coefficient is constant, the Seebeck coefficient takes the form of Eq.(3.8) and thus the power may be rewritten as:

$$P = I \left[ \tau(T ln(T) - T) + CT \right]_{T_C}^{T_H} - I^2 R \tag{3.10}$$

Substituting the definition of $\alpha$ from Eq.(3.8), the standard model output power takes the final form:

$$P = I(\alpha_H T_H - \alpha_C T_C) - I\tau(T_H - T_C) - I^2 R \tag{3.11}$$

If a factor of $N$ is distributed in the preceding equation to account for $N$ thermocouples in a device, Eq.(3.11) takes the same form as Eq.(2.27). The latter equation was derived by
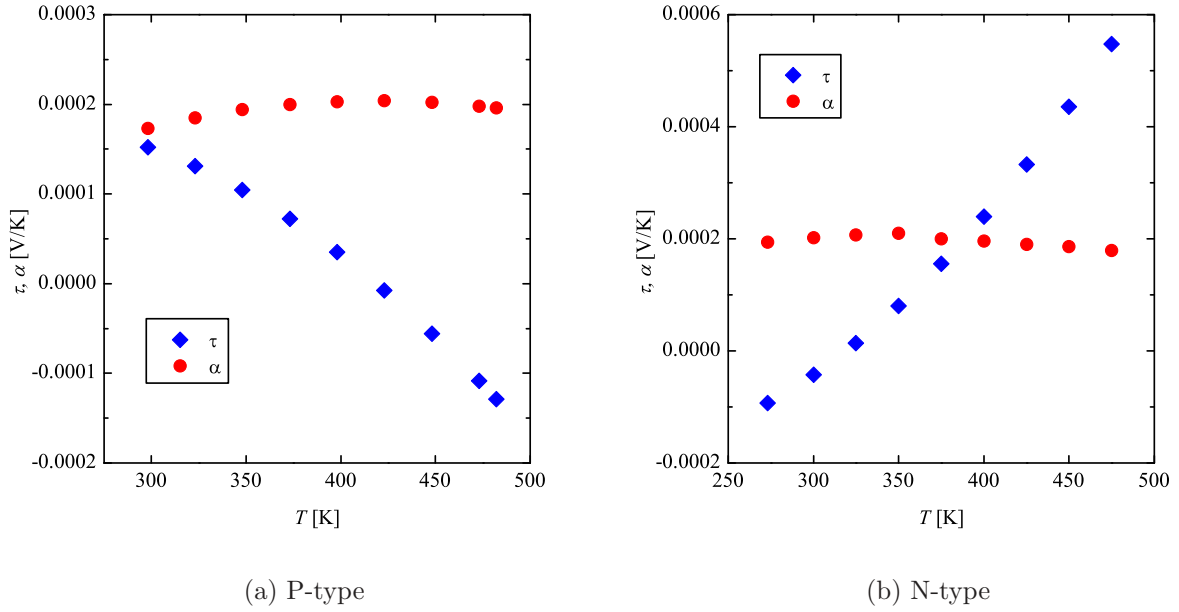
(a) P-type          (b) N-type

Figure 3.7: CRC $Bi_2Te_3$ (a) p-type and (b) n-type thermoelectric material properties. $\tau$ calculated from a polynomial fit of $\alpha$

solving the heat diffusion equations with the Thomson coefficient, Eqs.(2.21-2.26). The identical form of the two models in the case of the constant Thomson coefficient is demonstrative of the fact that any model using the integral average of the Seebeck coefficient approximates the Thomson effect.

The Thomson effect is present in any situation where the Seebeck coefficient is a function of temperature. Fig.(3.8) demonstrates that even at relatively low temperature gradients, the Thomson effect can be substantial (the equation governing the performance of a module that neglects the Thomson heat is Eq.(3.12)). The Thomson effect is never truly neglected by standard analytical models, although the authors will typically use language that indicates as much. If the Seebeck coefficient is averaged (by standard or integral averaging), the Thomson effect is implicit, and accounted for by approximation. This is expressed explicitly by Ioffe (Page 38) [4]:

> "For the time being we shall neglect the Thomson heat, regarding it as small in comparison with the other terms and shall assume $\alpha_1 = \alpha_0 = \alpha$. When $\alpha_1 \neq \alpha_0$ the Thomson heat is accounted for in the determination of the efficiency by substituting for $\alpha$ the mean value for the two ends $\overline{\alpha} = \frac{\alpha_1 + \alpha_0}{2}$."

The Thomson effect can be neglected in analytical models by simply using the non-averaged Seebeck coefficients for the heat flow into and out of the module. The power generated by a module, neglecting the Thomson heat entirely, may be represented as:

$$P_{TEM} = N[\alpha(T_H)T_H - \alpha(T_C)T_C]I - I^2 R_{TEM} \tag{3.12}$$

(a) Power
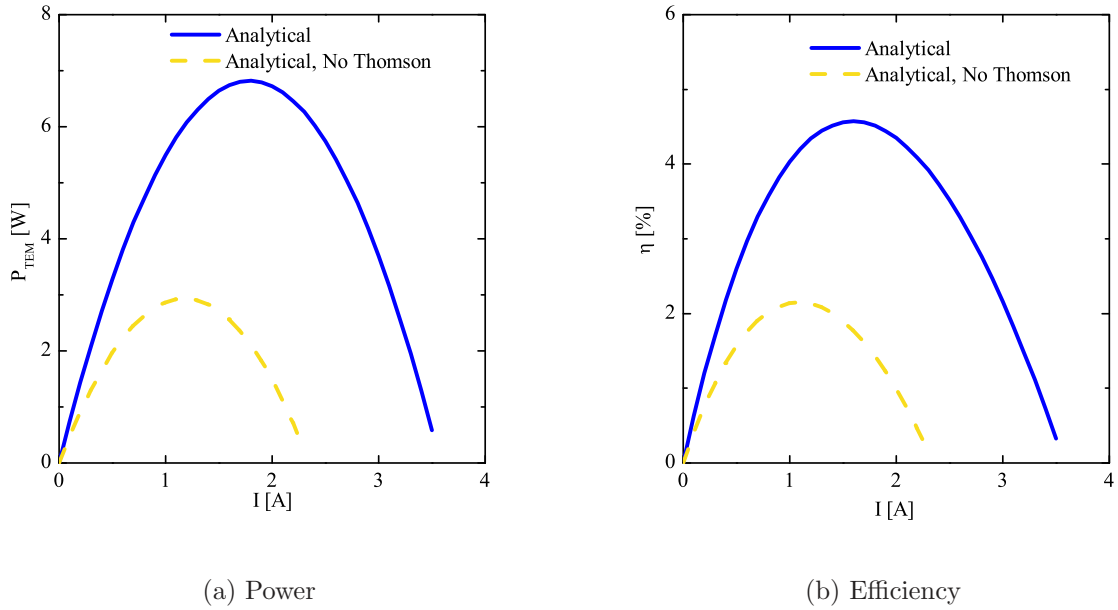
(b) Efficiency

Figure 3.8: (a) Module power output and (b) efficiency of models with and without the Thomson effect. The analytical models include the thermal resistance of the ceramic. Melcor properties with $T_H = 473$K and $T_C = 307$K

The preceding equation is highly inaccurate, as demonstrated by Fig.(3.8) and only serves to demonstrate the importance of quantifying the Thomson effect.

## 3.3 Asymptotics

Asymptotic mathematical techniques are powerful for modeling the behavior of complex differential equations. When implemented carefully, asymptotics can be used to approximate non-linear differential equations to a high degree of accuracy. Additionally, asymptotic methods provide a unique perspective on the effect of physical parameters on overall system behavior. By condensing the governing equations of a system into non-dimensional form, the impact of individual lumped parameters on the behavior of the overall system can be evaluated.

Depending on the given parameters, some of the normalized terms may contribute significantly less than others to the general system. Should a typically non-linear term be scaled such that it contributes less to the governing equation than the other terms, it is possible to replace it with an approximation. Careful identification of these small terms, and judicious substitution of simplified expressions can yield accurate results to previously unsolvable differential equations. The 1-D, steady state heat equation within a thermoelectric material is:

$$k\frac{d^2T}{dx^2} + JT\frac{d\alpha}{dT}\frac{dT}{dx} + \frac{J^2}{\sigma} = 0 \tag{3.13}$$

33

where the first term is the diffusion of heat within the body of a material, the second term is the Thomson heat (and non-linear term) that accounts for the heat liberated or absorbed due to the changing voltage profile as a result of the temperature-dependency of the Seebeck coefficient, and the last term is the Joule heat.

Expressing the heat equation in non-dimensional form:

$$\frac{d^2\bar{T}}{d\bar{x}^2} + \frac{JL}{k}(\bar{T}\Delta T + T_c)\frac{\Delta\alpha}{\Delta T}\frac{d\bar{\alpha}}{d\bar{T}}\frac{d\bar{T}}{d\bar{x}} + \frac{J^2L^2}{\sigma k\Delta T} = 0 \tag{3.14}$$

where $L$ is the length of the thermoelement legs,

$$\bar{T} = \frac{T - T_C}{T_H - T_C} \tag{3.15}$$

$$\bar{x} = \frac{x}{L} \tag{3.16}$$

$$\frac{d\bar{\alpha}}{d\bar{T}} = \frac{d\alpha\Delta T}{dT\Delta\alpha} \tag{3.17}$$

and $\Delta\alpha$ is the difference in the Seebeck coefficient from the hot side to the cold side of the leg and $\Delta T = T_H - T_C$.

With given parameters, the impact of the individual terms on the whole system can be evaluated. Very accurate analytical approximations of the system behavior can be made if the non-linearities are carefully replaced. Condensing Eq.(3.14), the non-dimensional thermoelectric heat equation may be represented:

$$\frac{d^2\bar{T}}{d\bar{x}^2} + \epsilon[S\bar{T} + 1]\frac{d\bar{\alpha}}{d\bar{T}}\frac{d\bar{T}}{d\bar{x}} + R_A = 0 \tag{3.18}$$

with

$$S = \frac{\Delta T}{T_C} \tag{3.19}$$

$$\epsilon = \frac{JLT_C\Delta\alpha}{k\Delta T} \tag{3.20}$$

$$R_A = \frac{J^2L^2}{\sigma k\Delta T} \tag{3.21}$$

and the boundary conditions $\bar{T} = 0$ at $\bar{x} = 0$ and $\bar{T} = 1$ at $\bar{x} = 1$.

Until now, the only actions performed on the heat equation have been non-dimensionalizing the equation and rearranging terms. Using parameter values that can be seen in typical modeling scenarios, the relative sizes of the non-dimensional terms can be evaluated. To roughly determine the term sizes, the Melcor material properties from Appendix A5, the approximation for the constant Thomson coefficient from the preceding section ($\tau = 0.093$mV/K) and the leg parameters from Table 3.1 are used (in this case electrical current, $I$ is assumed to

range from 1.5A to 3A with $T_H = 473K$ and $T_C = 307K$).

The first term in Eq.(3.14) is of order one because it has been normalized. The second term, which is non-linear, is conveniently order 0.1 (with current ranging from 1.5A to 3A, the term ranges from 0.05 to 0.11), which allows for a series approximation with few terms. Finally, the last term ranges (because of the current) from 0.08 to 0.33, although the relative size of this term is less important since it does not require approximation. From Eq.(3.18), $\epsilon$ is selected as the expansion coefficient, since it has a relatively small value (0.01 to 0.05). Here, in the limit as $\epsilon \to 0$ the temperature profile is expanded using an asymptotic series:

$$\bar{T} = \bar{T}_0 + \epsilon \bar{T}_1 + \epsilon^2 \bar{T}_2 + ... \tag{3.22}$$

Because $\epsilon$ is small, the expansion can be limited to the first two terms, which contribute the most.

$$\bar{T} \approx \bar{T}_0 + \epsilon \bar{T}_1 + 0(\epsilon^2) \tag{3.23}$$

Substituting Eq.(3.23) into Eq.(3.18) *and ignoring any term with $\epsilon^2$ or higher* yields:

$$\frac{d^2\bar{T}_0}{d\bar{x}^2} + \epsilon \frac{d^2\bar{T}_1}{d\bar{x}^2} + \epsilon(S\bar{T}_0 + 1) \left.\frac{d\bar{\alpha}}{d\bar{T}}\right|_{\bar{T}_0} \frac{d\bar{T}_0}{d\bar{x}} + R_A = 0 \tag{3.24}$$

Grouping terms of like order $\epsilon$, the heat equations can be expressed as simple differential equations with polynomial forcing functions:

$$\frac{d^2\bar{T}_0}{d\bar{x}^2} = -R_A \tag{3.25}$$

$$\frac{d^2\bar{T}_1}{d\bar{x}^2} = -(S\bar{T}_0 + 1) \left.\frac{d\bar{\alpha}}{d\bar{T}}\right|_{\bar{T}_0} \frac{d\bar{T}_0}{d\bar{x}} \tag{3.26}$$

with the boundary conditions $\bar{T}_0 = \bar{T}_1 = 0$ at $\bar{x} = 0$ and $\bar{T}_0 = 1, = \bar{T}_1 = 0$ at $\bar{x} = 1$. Solving for $\bar{T}_0$ and $\frac{d\bar{T}_0}{d\bar{x}}$ is trivial:

$$\bar{T}_0 = -\frac{R_A}{2}\bar{x}^2 + (1 + \frac{R_A}{2})\bar{x} \tag{3.27}$$

$$\frac{d\bar{T}_0}{d\bar{x}} = -R_A\bar{x} + \frac{R_A}{2} + 1 \tag{3.28}$$

In order to evaluate $\bar{T}_1$, a functional form of $\bar{\alpha}$ must be defined. The experimental data for $\alpha$ is typically curve-fit using a polynomial of varying order. It is assumed that the Seebeck coefficient will always be expressed by a polynomial function:

$$\bar{\alpha} = \sum_{i=0}^{n} C_i \bar{T}^i \tag{3.29}$$

The Melcor data for the Seebeck coefficient is fit with a fifth-order polynomial. For

simplicity, the Seebeck coefficient will be assumed to be curve-fit with a polynomial of order five or less. The polynomial is left in general form so that the coefficients from a curve fit from any material may be entered into the model for analysis. If a polynomial of order less than five is used for a curve fit, then the superfluous terms may be set to zero from here throughout the rest of the analysis. The non-dimensional Seebeck coefficient will thus take the form:

$$\bar{\alpha} = C_0 + C_1\bar{T} + C_2\bar{T}^2 + C_3\bar{T}^3 + C_4\bar{T}^4 \tag{3.30}$$

Likewise, the derivative of $\bar{\alpha}$ with respect to normalized temperature is:

$$\frac{d\bar{\alpha}}{d\bar{T}} = C_1 + 2C_2\bar{T} + 3C_3\bar{T}^2 + 4C_4\bar{T}^3 \tag{3.31}$$

The conversion from $\alpha$ to $\bar{\alpha}$ is simple, but necessary. If the dimensional Seebeck coefficient takes the form:

$$\alpha = \beta_0 + \beta_1 T + \beta_2 T^2 + \beta_3 T^3 + \beta_4 T^4 \tag{3.32}$$

then the corresponding coefficients of the non-dimensional $\frac{d\bar{\alpha}}{d\bar{T}}$, $C_i$ are defined as:

Table 3.2: Coefficients of $\bar{\alpha}$ terms

| Coefficient | Value |
|---|---|
| $C_4$ | $(\beta_4\Delta T^3)(\frac{\Delta T}{\Delta \alpha})$ |
| $C_3$ | $(\beta_3\Delta T^2 + 4\beta_4\Delta T^2 T_c)(\frac{\Delta T}{\Delta \alpha})$ |
| $C_2$ | $(\beta_2\Delta T + 3\beta_3\Delta T T_c + 6\beta_4\Delta T T_c^2)(\frac{\Delta T}{\Delta \alpha})$ |
| $C_1$ | $(\beta_1 + 2\beta_2 T_c + 3\beta_3 T_c^2 + 4\beta_4 T_c^3)(\frac{\Delta T}{\Delta \alpha})$ |

Substituting Eq.(3.27), Eq.(3.28) and Eq.(3.31) into Eq.(3.26) yields an expression of $\frac{d^2\bar{T}_1}{d\bar{x}^2}$ in terms of $\bar{x}$ and TEM parameters. Thus, integrating $\frac{d^2\bar{T}_1}{d\bar{x}^2}$ twice with respect to $\bar{x}$ and applying the boundary conditions $\bar{T}_1 = 0$ at $\bar{x} = 0$ and $\bar{T}_1 = 1$ at $\bar{x} = 1$, the following expression for $\bar{T}_1$ is achieved:

$$\bar{T}_1 = \sum_{i=2}^{11} B_i\bar{x}^i + \bar{x}\sum_{i=0}^{5} D_i R_A^i \tag{3.33}$$

where the coefficients $B_i$ and $D_i$ are expressed in Table 3.3 and Table 3.4.

With expressions of $\bar{T}_0$ and $\bar{T}_1$ in terms of $\bar{x}$ and module parameters, $\bar{T}$ can be expressed by combining Eq.(3.33) and Eq.(3.27) into Eq.(3.23). $\bar{T}(\bar{x})$ is the approximate solution to the non-linear differential equation.

The non-dimensional variables can be differentiated and transformed quickly using the normalizing identities Eqs.(3.15-3.16) to get an expression of $\frac{dT}{dx}$.

$$\frac{d\bar{T}}{d\bar{x}} = \frac{d\bar{T}_0}{d\bar{x}} + \epsilon\frac{d\bar{T}_1}{d\bar{x}} \tag{3.34}$$

Table 3.3: Coefficients of $\bar{x}$ terms

| Coefficient | Value |
|---|---|
| $B_{11}$ | $\frac{1}{440} S R_A^5 C_4$ |
| $B_{10}$ | $-\frac{1}{80} S R_A^5 C_4 - \frac{1}{40} S R_A^4 C_4$ |
| $B_9$ | $-\frac{1}{192} S R_A^4 C_3 + \frac{1}{9} S R_A^3 C_4 - \frac{1}{144} R_A^4 C_4 + \frac{1}{9} S R_A^4 C_4 + \frac{1}{36} S R_A^5 C_4$ |
| $B_8$ | $-\frac{3}{8} S R_A^3 C_4 - \frac{3}{16} S R_A^4 C_4 + \frac{3}{64} S R_A^3 C_3 - \frac{1}{4} S R_A^2 C_4 + \frac{1}{32} R_A^4 C_4 + \frac{1}{16} R_A^3 C_4$ $+ \frac{3}{128} S R_A^4 C_3 - \frac{1}{32} S R_A^5 C_4$ |
| $B_7$ | $-\frac{9}{224} S R_A^4 C_3 + \frac{1}{7} S R_A^4 C_4 + \frac{2}{7} S R_A C_4 + \frac{1}{56} S R_A^5 C_4 - \frac{9}{56} S R_A^2 C_3 + \frac{4}{7} S R_A^2 C_4$ $+ \frac{1}{56} R_A^3 C_3 - \frac{3}{56} R_A^4 C_4 - \frac{3}{14} R_A^2 C_4 - \frac{3}{14} R_A^3 C_4 - \frac{9}{56} S R_A^3 C_3 + \frac{3}{7} S R_A^3 C_4 + \frac{1}{84} S R_A^3 C_2$ |
| $B_6$ | $\frac{1}{24} R_A^4 C_4 + \frac{1}{3} R_A C_4 + \frac{1}{4} S R_A C_3 - \frac{1}{3} S R_A C_4 + \frac{3}{8} S R_A^2 C_3 - \frac{1}{8} R_A^2 C_3 + \frac{3}{16} S R_A^3 C_3$ $+ \frac{1}{4} R_A^3 C_4 - \frac{1}{6} S R_A^3 C_4 - \frac{1}{24} S R_A^4 C_4 + \frac{1}{2} R_A^2 C_4 - \frac{1}{240} S R_A^5 C_4 - \frac{2}{15} S C_4 + \frac{1}{32} S R_A^4 C_3$ $- \frac{1}{3} S R_A^2 C_4 - \frac{1}{12} S R_A^2 C_2 - \frac{1}{24} S R_A^3 C_2 - \frac{1}{16} R_A^3 C_3$ |
| $B_5$ | $\frac{3}{10} R_A C_3 - \frac{3}{40} S R_A^3 C_3 + \frac{3}{40} R_A^3 C_3 - \frac{2}{5} R_A C_4 + \frac{3}{10} R_A^2 C_3 - \frac{1}{80} R_A^4 C_4 - \frac{3}{320} S R_A^4 C_3$ $- \frac{1}{40} S R_A^2 C_1 - \frac{9}{40} S R_A^2 C_3 + \frac{1}{5} S R_A^2 C_2 - \frac{1}{20} R_A^2 C_2 + \frac{1}{5} S R_A C_2 - \frac{1}{10} R_A^3 C_4$ $- \frac{3}{10} R_A^2 C_4 + \frac{1}{20} S R_A^3 C_2 - \frac{3}{10} S R_A C_3 - \frac{3}{20} S C_3 - \frac{1}{5} C_4$ |
| $B_4$ | $-\frac{3}{16} R_A^2 C_3 - \frac{1}{4} S R_A C_2 - \frac{1}{32} R_A^3 C_3 + \frac{1}{8} S R_A C_1 + \frac{1}{8} R_A^2 C_2 - \frac{1}{4} C_3 + \frac{1}{4} R_A C_2$ $+ \frac{1}{16} S R_A^2 C_1 - \frac{1}{4} S R_A^2 C_2 - \frac{3}{8} R_A C_3 - \frac{1}{48} S R_A^3 C_2 - \frac{1}{6} S C_2$ |
| $B_3$ | $-\frac{1}{6} S R_A C_1 - \frac{1}{24} S R_A^2 C_1 - \frac{1}{12} R_A^2 C_2 + \frac{1}{6} R_A C_1 - \frac{1}{3} C_2 - \frac{1}{3} R_A C_2 - \frac{1}{6} S C_1$ |
| $B_2$ | $-\frac{1}{2} C_1 - \frac{1}{4} R_A C_1$ |

Table 3.4: Coefficients of $R_A$ terms

| Coefficient | Value |
|---|---|
| $D_5$ | $\frac{1}{110880} S C_4$ |
| $D_4$ | $\frac{1}{13440} S C_3 + \frac{1}{10080} C_4 + \frac{1}{5040} S C_4$ |
| $D_3$ | $\frac{1}{1120} C_3 + \frac{1}{1680} S C_2 + \frac{3}{2240} S C_3 + \frac{1}{560} C_4 + \frac{1}{504} S C_4$ |
| $D_2$ | $\frac{1}{84} S C_4 + \frac{1}{120} C_2 + \frac{1}{80} C_3 + \frac{3}{280} S C_3 + \frac{1}{120} S C_2 + \frac{1}{240} S C_1 + \frac{1}{70} C_4$ |
| $D_1$ | $\frac{1}{12} C_1 + \frac{1}{20} S C_2 + \frac{1}{20} S C_3 + \frac{1}{15} C_4 + \frac{1}{12} C_2 + \frac{3}{40} C_3 + \frac{1}{24} S C_1 + \frac{1}{21} S C_4$ |
| $D_0$ | $\frac{1}{2} C_1 + \frac{1}{3} C_2 + \frac{1}{4} C_3 + \frac{1}{5} C_4 + \frac{3}{20} S C_3 + \frac{1}{6} S C_1 + \frac{2}{15} S C_4 + \frac{1}{6} S C_2$ |

$$\frac{dT}{dx} = \left( \frac{d\bar{T}_0}{d\bar{x}} + \epsilon \frac{d\bar{T}_1}{d\bar{x}} \right) \frac{\Delta T}{L} \tag{3.35}$$

where $\frac{d\bar{T}_1}{d\bar{x}}$ can be expressed as:

$$\frac{d\bar{T}_1}{d\bar{x}} = \sum_{i=2}^{11} i B_i \bar{x}^{i-1} + \sum_{i=0}^{5} D_i R_A^i \tag{3.36}$$

Thus the heat flow into and out of the leg can be calculated by combining the preceding equation and Eq.(3.28) into Eq.(3.35).

$$\frac{dT}{dx} = \left( -R_A \left( \frac{x}{L} \right) + \frac{R_A}{2} + 1 + \epsilon \left[ \sum_{i=2}^{11} i B_i \left( \frac{x}{L} \right)^{i-1} + \sum_{i=0}^{5} D_i R_A^i \right] \right) \frac{\Delta T}{L} \tag{3.37}$$

The module's performance can be fully described with $\frac{dT}{dx}$, utilizing the definition of heat flow out of the module Eq.(2.25), into a module Eq.(2.26) and the definition of module

output power, Eq.(2.10).

In order to implement this model, one would use the module parameters and operating conditions to get expressions for $\epsilon$, $S$ and $R_A$, Eqs.(3.19-3.21), and combine them with the coefficients of the curve fit of $\alpha$ ($C_i$) in preceding tables. If $\alpha$ requires a polynomial of less than order four, the unused coefficients can be set equal to zero. This procedure can be amended to accommodate either more coefficients for $\alpha$, or to have a longer expansion of $\bar{T}$ by taking more terms in Eq.(3.22).

The power output of a module accounting for separate thermoelectric leg material properties, according to the asymptotic model is:

$$P_{TEM} = N\left(I(\alpha_H T_H - \alpha_C T_C) - \frac{I^2 L}{\sigma_p A} - \frac{I^2 L}{\sigma_n A} + IT_C \Delta\alpha_p \sum_{i=2}^{11} iB_{p,i} + IT_C \Delta\alpha_n \sum_{i=2}^{11} iB_{n,i}\right)$$
(3.38)

The asymptotic model, aside from being a new design tool in and of itself, sheds light into specific terms that previously could not be solved analytically. Most importantly, it can be used to define a bulk Thomson coefficient accurately, for any temperature-dependent Seebeck coefficient. For simplicity's sake, if the p-type and n-type material were assumed to have the same material property values, Eq.(3.38) and Eq.(2.27) can be set equal to each other to find the asymptotic expansion of the Thomson coefficient. Quick analysis reveals the approximation for the Thomson coefficient in a bulk thermoelectric material experiencing a temperature gradient:

$$\tau^* = \pm T_C \frac{\Delta\alpha}{\Delta T} \sum_{i=2}^{11} iB_i$$
(3.39)

where the sign is positive for the p-type material and negative for the n-type material. This expression holds true for any material, and does not require that the p-type and n-type materials share the same material properties. This is the Thomson coefficient throughout the entire leg, and can be used to quantify the bulk Thomson heat in a thermoelectric module.

The asymptotic model elucidates the Thomson heat in another manner. Fig.(3.9) depicts the unitless temperature profile of the asymptotic model when the term $\epsilon$ is active and when it has a value of zero. The asymptotic contribution (the term that $\epsilon$ is a coefficient for, which is the Thomson heat), only shifts the temperature profile order $\epsilon$, which is to say order 0.05. However, this subtle shift in the temperature has a profound impact on the temperature gradient, $\frac{d\bar{T}}{d\bar{x}}$, which is used in calculating the output power of the thermoelectric module. As such, the asymptotic expansion has a large impact on power output, and confirms the findings of the previous section, namely that the Thomson heat is present and accounts for a substantial portion of the module's output power. When $\epsilon = 0$, the Thomson heat is neglected, and reciprocally when it is active (non-zero value), the Thomson heat is present.

The output power comparison for the asymptotic model (which accounts for the Thom-
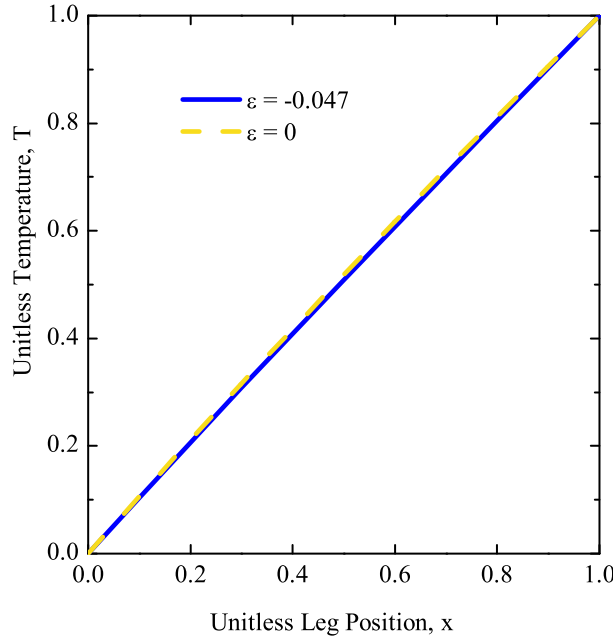
Figure 3.9: Unitless temperature profile of asymptotic and standard models. Melcor material properties (appendix A5), $T_H = 473K$, $T_C = 307K$ and $I = 3A$

son heat exactly) compared to the standard model can be seen in Fig.(3.10). The asymptotic expansion does not appear to deviate significantly from the standard model which approximates the Thomson heat by averaging the Seebeck coefficient. The models in the left hand side of Fig.(3.10) do not account for the thermal resistance of the ceramic substrates while the models in the right hand side do contain ceramic interfaces.

The asymptotic model allows for the calculation of the effective bulk Thomson coefficient for a thermoelectric material, $\tau^*$, which was previously unattainable because of the non-linearity of the governing equations. Resultantly, the contribution of the Thomson heat can be quantified exactly. In all cases, the Thomson heat contributes significantly to the performance of the module, and this contribution is approximated in the standard model by averaging the Seebeck coefficient.

## 3.4   Model Summary

Several effects have been dissected and evaluated for accuracy in the modeling of a thermo-electric module. The objective of this investigation was to develop a robust analytical model that could be used as a design tool. The following has been ascertained of the effects that were evaluated:

1. The thermal resistance of the ceramic substrate significantly diminishes module performance, and should always be accounted for.
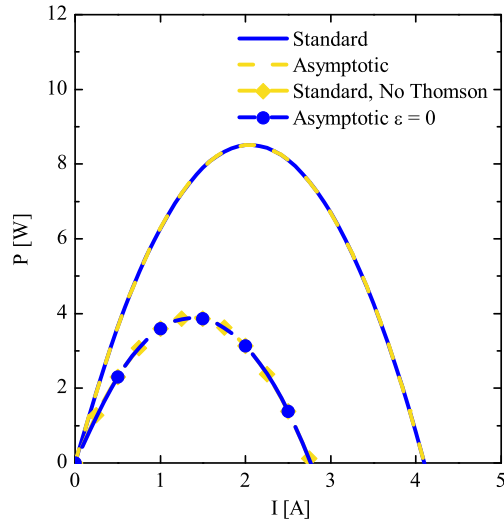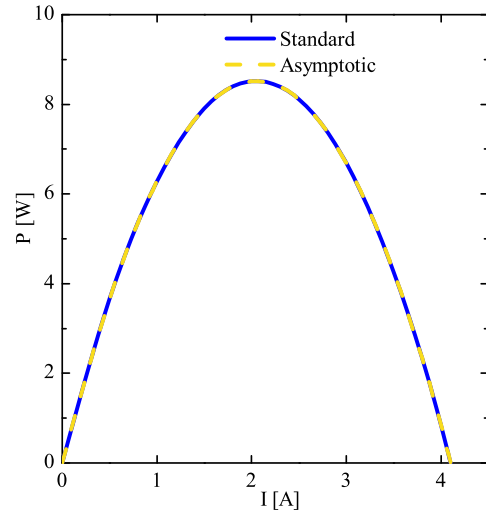
(a) No Ceramic, Melcor          (b) With Ceramic, CRC

Figure 3.10: Asymptotic model vs. standard model power output. $T_H = 473$K, $T_C = 307$K. (a) Melcor $Bi_2Te_3$ material properties, no ceramic substrate (b) CRC $Bi_2Te_3$ a ceramic substrate has been included

2. Heat leakage around the thermoelement legs is negligible. In worst case (a radiative emissivity value of 1), bypass heat leakage amounted to less than 5% of the heat moved by the Peltier effect and conducted through the thermoelectric device.

3. The Thomson heat is always present in a thermoelectric material, and has a significant impact on module performance.

4. The asymptotic model allows for an effective bulk Thomson coefficient to be calculated, and likewise the Thomson heat to be quantified.

5. The Thomson heat is approximated in the standard analytical model by averaging the Seebeck coefficient between the hot and cold sides of the thermoelectric device. When this is done, the Seebeck coefficient is assumed to be constant, and thus the Thomson heat is removed from the governing heat equation *but is still present in the analysis in the form of the averaged Seebeck coefficient.*

6. Assuming a constant Thomson coefficient is typically inappropriate for analysis. Thermoelectric material properties under most applicable temperature gradients do not permit the assumption of a constant Thomson coefficient.

For further comparison to finite element models, the standard model (averaged Seebeck coefficient), is augmented with the ceramic resistance model. The heat leakage is assumed to be negligible, and is thus not incorporated into the improved standard model.

40

# Chapter 4

# Experimental Work

In 2006, RIT commissioned the design and fabrication of a test stand capable of addressing many of the issues that arise from testing thermoelectrics [20]. The test stand was designed to explore and document thermoelectric module behavior under varying operating temperatures. The thermal delivery system is comprised of a copper heating block with integral cartridge heaters to supply heat flow into the hot-side of a TEM, and a cold-plate with circulating coolant to remove the heat from the cold-side of the TEM.

## 4.1 Description of Thermoelectric Module Test Stand

A test stand was designed to capture critical module parameters necessary for analysis [22]. Special attention was given to ensure: i) uniform and constant hot-side and cold-side temperatures, ii) a variable electrical load must be provided to dissipate the power generated by a test specimen, iii) the load pressure experienced by a given test specimen should be recordable and repeatable, iv) the amount of heat being delivered to the test specimen must be accurately measurable.

Measuring the heat flow into a module is critical to defining overall module conversion efficiency, and is arguably the most difficult parameter to quantify.

The test stand consists of a shielded heating block, cold-plate, as well as electrical and mechanical loading systems as seen in Fig.(4.1). Capable of delivering up to 1300 W of heat, the test stand can maintain a constant, uniform hot-side temperature up to 500 °C on modules of sizes up to 14cm x 15cm. The heat delivered to a TEM specimen, which is notoriously difficult to quantify and is frequently cited as a shortcoming of test stand designs, is determined using a novel method described in the proceeding section.

Mechanical loading conditions can have a significant effect on TEM performance. Since thermal contact resistances can be non-trivial, it is important for them to be understood and minimized. The force applied to the specimen is measured by load cells located under the cold-plate. The pressure loading system, in conjunction with the load cells allow for loading conditions of a module to be both varied for study and repeated for consistency between scans.
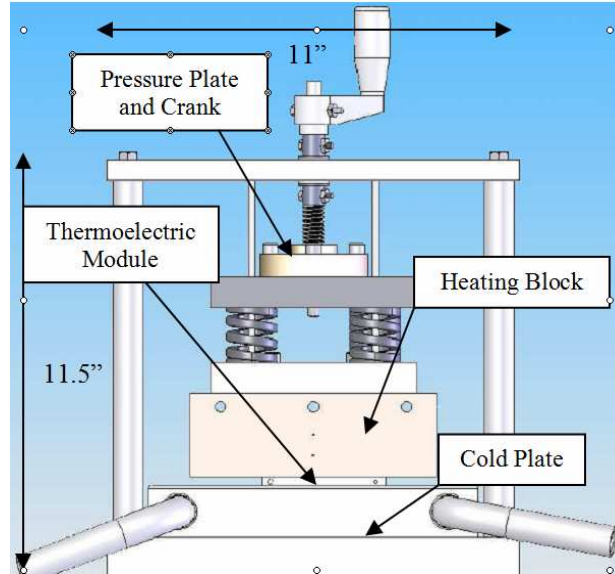
Figure 4.1: Schematic of the RIT TEM Test Stand [21]

## 4.2 Thermal Characterization of Test Stand

To determine the heat transfer through a TEM, the heat losses through the insulation on the top and the sides of the heating block must be accounted for, in addition to the losses through the insulation surrounding the sides of a TEM specimen. Typical module characterization tests involved monitoring the power delivered to the copper hot plate using a power analyzer. To determine the heat flow across an individual module, heat losses to the top and bottom of the test stand were determined at a range of temperatures. The heat losses through the top insulation were measured with 3% or less uncertainty [22]. TE module testing involved placing a module between the hot and cold plate, with thin insulation surrounding the TEM. The thermal losses through this insulation were also characterized with 5% or less uncertainty.

By monitoring the power delivered to the heating block and removing the losses through the top and bottom insulation, one is able to extract the total amount of heat transferred through a TE module. To validate the heat transfer measurements, two reference materials were tested: Borofloat borosilicate and Macor glass ceramic. These materials are highly thermally stable and have comparable thermal conductivities to those found in TE modules. The sample dimensions were chosen to have comparable thermal resistance to what was expected in typical room temperature TEM. Thermal grease was applied and the samples were pressed between the hot and cold plates at a pressure of 690 kPa and allowed to reach steady state.

The measured and published thermal conductivity are shown in Fig.(4.2). There is excellent agreement between the measured and published values. In the case of the borosilicate sample, the differences were less than the uncertainty in the measurement which was 4.2% or less. In the case of the Macor, the differences were less than 6.5%, which is close to the experimental uncertainty of 4.2%. Therefore we have great confidence in our ability to
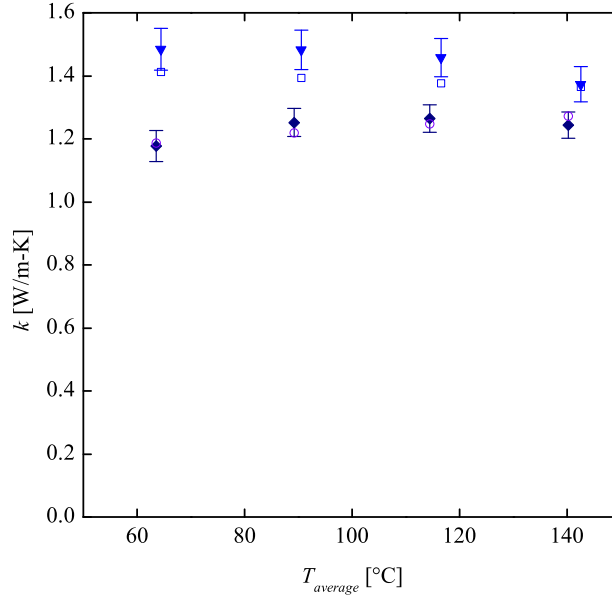
Figure 4.2: Measured versus published thermal conductivity for Borofloat (light blue triangle) and Macor (dark blue diamond) reference samples. The open shapes are published thermal conductivity values.

determine the heat flow through TE modules within 5% uncertainty.

Other areas of potential concern were in variations due to different loading pressures and application of thermal grease. A series of tests were conducted on the same TEM at loading pressures of 345, 690, and 1035 kPa. Although there was a slight increase in max operating power and the measured TEM parameters, the differences in all values was less than 4% over the tested loading range. All future tests were loaded at 690 kPa. A repeatability study between multiple operators revealed a deviation of measured parameters of less than 9%.

## 4.3    Module Scan and Parameter Measurement

A module scan consists of loading a module to the desired pressure and temperatures and leaving the module in open circuit conditions for approximately an hour to reach steady state conditions, which was determined by monitoring the heat input rate to the hot plate. Once steady state was reached, after typically 30 minutes or more, temperature and power data was collected and averaged in order to determine the module total thermal resistance $(R_{te}/N)$, which is explained below. The module was then connected to the loading box and typically twelve different electrical loads were automatically applied to capture the entire voltage-current curve for the module. For each load, the system was allowed to reach steady state for at least a minute and then voltage, current, and input thermal power were recorded and averaged for nearly two minutes before proceeding to the next loading condition.

The scan data can be used in one of three ways: i) to compare with theoretical models as will be demonstrated later, ii) validate performance of newly designed TE modules, and iii) extract TE module parameters for system design purposes.
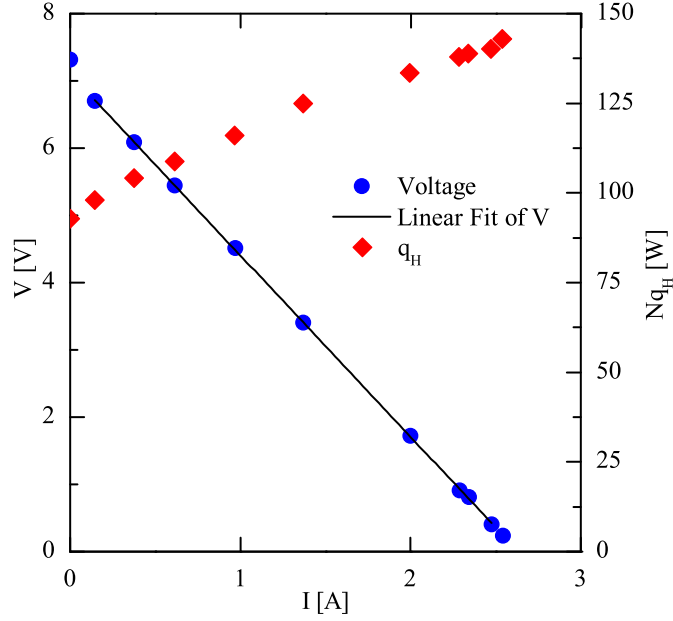
Figure 4.3: Sample Melcor module scan,$T_H = 473$K, $T_C = 306$K

For TE system design there are three TEM parameters needed (assuming a standard 1-D model): i) module level Seebeck parameter ($N\alpha_{p,n}$), ii) module level electrical resistance ($NR_e$), and iii) module level thermal resistance ($R_t/N$), where $N$ is the number of thermoelectric leg pairs. Consider the energy transfer and temperatures in Fig.(4.3) for a thermoelectric module with $N$ thermoelectric leg pairs.

Assuming negligible contact resistances and substrate resistances, the heat flowing into the hot surface and out of the cold surface of a TEM can be expressed with Eq.(2.8) and (2.9) where $K_{TEM} = N/R_t$ and $R_{TEM} = NR_e$.

The principal approach to extracting module parameters is to minimize the residuals between the measured generated power (or voltage, either will suffice) and hot side heat transfer data and Eqs.(2.8) and (2.11) for all electrical loads by varying the three module parameters. A typical scan can be seen in Fig.(4.3).

Dividing the module power by current, $I$, Eq.(2.11) can be rewritten as an expression of voltage:

$$V = -NR_e I + N\alpha_{p,n}(T_H - T_C) \tag{4.1}$$

$NR_e$ and $N\alpha_{p,n}$ can be determined by measuring the open circuit voltage ($V_{OC}$) and short circuit current ($I_{SC}$).

$$N\alpha_{p,n} = \frac{V_{OC}}{T_H - T_C} \tag{4.2}$$

Table 4.1: Parameters of Two Thermoelectric Modules

| Module | $T_h(C)$ | $T_c(C)$ | $N\alpha_{p,n}(mV/K)$ | $NR_e(\Omega)$ | $R_t/N(K/W)$ | $P_{max}(W)$ | $\eta_{max}(\%)$ |
|---|---|---|---|---|---|---|---|
| Melcor HT8-12-40-W6 | 99.2 | 29.0 | $47.3 \pm 4.2$ | $2.19 \pm 0.30$ | $1.68 \pm 0.07$ | 1.3 | 2.4 |
| | 148.9 | 30.9 | $46.0 \pm 2.6$ | $2.4 \pm 0.21$ | $1.73 \pm 0.06$ | 3.1 | 3.6 |
| | 198.5 | 33.5 | $47.0 \pm 1.9$ | $2.66 \pm 0.17$ | $1.68 \pm 0.05$ | 5.6 | 4.7 |
| Hi-Z Technology 14W | 99.0 | 29.1 | $13.4 \pm 0.3$ | $0.130 \pm 0.005$ | $0.729 \pm 0.016$ | 1.7 | 1.5 |
| | 148.7 | 31.8 | $13.7 \pm 0.2$ | $0.137 \pm 0.003$ | $0.752 \pm 0.014$ | 4.7 | 2.5 |
| | 198.2 | 34.1 | $14.1 \pm 0.1$ | $0.150 \pm 0.003$ | $0.750 \pm 0.013$ | 8.9 | 3.4 |
| | 247.4 | 36.7 | $14.1 \pm 0.1$ | $0.164 \pm 0.003$ | $0.765 \pm 0.013$ | 13.5 | 4.1 |

$$NR_e = \frac{V_{OC}}{I_{SC}} \tag{4.3}$$

The thermal resistance can be determined by measuring $Nq_H$ under open circuit conditions such that

$$\frac{R_t}{N} = \frac{T_H - T_C}{Nq_H} \tag{4.4}$$

Table 4.1 shows measured module parameters along with the max power and efficiency obtained by using the methods on two different TEMs. The uncertainty was generally less than 8% and in many cases less than 2%.

# Chapter 5

# Finite Element Modeling

While techniques for quantitatively evaluating thermoelectric materials for power generation are well understood, little focus has been given to modeling module-level behavior. Facets of module design which can contribute to module inefficiency, such as lateral leg spacing and ceramic interface thickness, have been largely ignored. It is imperative that a comprehensive model is developed to efficiently design thermoelectric modules (TEMs) to fully capitalize off of recent materials advancements.

Where analytical solutions fail, finite element methods (FEM) can provide a robust and accurate alternative. Recent advances in multiphysics coupling in commercial software have made finite element (FE) packages competitive with finite difference techniques tailored for thermoelectric analysis [11]. These new advances fully couple the electrical and thermal governing equations and can easily converge on solutions to non-linear system of equations. Additionally, new geometrical configurations can easily be explored with 3-D FEM, thus providing a new opportunity for thermoelectric module design improvement.

The FE technique is a powerful method for solving partial differential equations, and in many cases can handle non-linear governing equations. In general, FE algorithms break up geometric domains (the TE leg pair) that are governed by a set of equations (in this case the governing equations of thermoelectric heat transfer and direct electrical current) into a finite number of elements called a mesh. An approximate solution form of the dependent variable is assumed for each element by basis functions known as "shape" or "interpolation" functions. After applying appropriate boundary conditions, a solution is converged upon by several possible methods, including iteratively solving weighted residuals, or solving a global stiffness matrix.

With regards to thermoelectric modules, a FE model can provide several unique advantages. First, an FE model can solve the governing set of partial differential equations that cannot be solved analytically. This can permit the investigation of complex geometries, including curved geometries that cannot be solved analytically due to boundary condition constraints. The standard rectangular configuration of a thermoelectric leg pair cannot be solved analytically when the ceramic substrate has a larger area than the legs. Secondly, when material property temperature-dependency is accounted for, the non-linearities that

arise can be handled by a carefully chosen FE solver, whereas an analytical solution does not exist.

Explicitly put, there is likely to be a strong divergence between the analytical and FE models when either i) the geometry deviates significantly from a 1-D configuration or ii) the material property temperature-dependence is accounted for under large temperature gradients. Both of these scenarios are tested in the next chapter, once the FE model has been described.

Generally, the steps for FE analysis are:

1. Selection of general governing physics (viz. heat transfer and DC electricity)

2. Creation of appropriate subdomains (geometries)

3. Application of appropriate boundary and subdomain conditions (viz. temperatures, insulation, grounding, internal heating, etc.)

4. Meshing of the subdomains into an appropriate number of elements

5. Selecting and utilizing a solver algorithm

6. Postprocessing to acquire pertinent information

Every aspect of FE analysis is multifaceted, and thus a detailed account for a finite element model is outlined in the following sections. Foremost is the selection of the governing equations for a thermoelectric material.

## 5.1   Governing Equations

The general form of the steady-state, coupled governing equations that dictate thermoelectric behavior within and on a subdomain are [11] the following:

$$\mathbf{q} = T[\alpha] \cdot \mathbf{J} - [k] \cdot \nabla T \tag{5.1}$$

where $\mathbf{q}$ is the vector form of the heat flux on a boundary of a thermoelectric subdomain (volume), $[\alpha]$ is the Seebeck coefficient matrix, $\mathbf{J}$ is the vector form of the current flux on a boundary, $[k]$ is the thermal conductivity matrix and $T$ is the absolute temperature. All material properties are assumed to be isotropic.

The electrical current density is defined as:

$$\mathbf{J} = [\sigma] \cdot (\mathbf{E} - [\alpha] \cdot \nabla T) \tag{5.2}$$

where $[\sigma]$ is the electrical conductivity matrix and $\mathbf{E}$ is the electric field vector.

The thermoelectric subdomains are governed by:

$$\nabla \cdot \mathbf{q} = Q_{Joule} \tag{5.3}$$

$$\nabla \cdot \mathbf{J} = 0 \tag{5.4}$$

which indicates that current is conserved under steady-state, and that several forms of internal heating occur within a thermoelectric subdomain.

The joule heating per unit volume within the thermoelectric subdomain takes the form:

$$Q_{Joule} = \mathbf{J}^2/\sigma = \mathbf{E} \cdot \mathbf{J} - [\alpha]\nabla T \cdot \mathbf{J} \tag{5.5}$$

The second term on the right side of the Joule heat represents the work done against the electric potential that is generated by the temperature gradient. Combining Eqs.(5.1-5.5) yields the following heat equation [23]:

$$T\mathbf{J} \cdot \nabla[\alpha] + \frac{d\alpha}{dT}T\nabla T \cdot \mathbf{J} - \nabla \cdot ([k] \cdot \nabla T) = \mathbf{J}^2/\sigma \tag{5.6}$$

The first term of Eq.(5.6), which is the bulk Peltier effect, is typically neglected since the gradient of the Seebeck coefficient is zero unless the thermoelement leg has functionally graded doping. The second term is the bulk Thomson heat, which accounts for the electric potential change due to the temperature-dependency of the Seebeck coefficient.

Any metal or ceramic is assumed to have $[\alpha] = [0]$, and any ceramic is assumed to have $[\sigma] = [0]$. These assumptions permit the use of all of the governing equations in any material subdomain.

## 5.2  Finite Element Software Package, COMSOL

The selection of an appropriate FE software package hinges on several issues. Foremost, the FE package must either have the thermoelectric governing equations built in as a modeling option, or give the user the ability to alter the governing equations to incorporate the TE-unique terms (as seen in Eq.(5.6)). The latter option is preferable, since it allows for flexibility and the option to engage/disengage specific terms to see their relative impact on the model.

Additionally, the ideal package would have a good selection of solver algorithms to choose from to allow for rapid and accurate convergence on a solution. Because the governing equations are non-linear (where convergence is not guaranteed), the solver must be carefully selected in order to ensure convergence.

One such package, COMSOL, provides flexibility both in the manipulation of the governing equations and the selection of appropriate solvers. Whereas competitors have constrained thermoelectric governing equations, COMSOL permits the user to select which terms to incorporate, such as the Thomson heat, to determine the overall impact on the module performance. This ability to alter the governing equations is critical to determining which models

are appropriate under specific conditions and thus COMSOL proves to be an ideal tool for this study.

## 5.3 General Model Description

Commercially available TEMs consist of dozens of thermoelement p-n junctions (or leg pairs) connected in series by copper contacts. The assembly is typically packaged by being sandwiched between ceramic substrates for electrical insulation and structural support. The ceramic interface thickness, electrical contact geometry and leg spacing can play a primary role in heat recovery, despite being neglected as critical module design parameters. The efficiency and power density of a module can be significantly improved by optimizing the module layout.

The analysis of dozens of thermoelement pairs can be highly computationally intensive, so the model is limited to a single pair, seen in Fig.(5.1). All of the TEM geometry parameters can be probed by examining a single leg pair connected by electrical contacts and solder. Extrapolating the module performance from the behavior of a single pair assumes that the heat flux through the module is constant across the ceramic interfaces.

Since the solder bead between modules can provide a secondary heat path into the legs and increase the effective area of the thermoelement junction, both efficiency and power-density of a module can be affected by the thickness of the solder. Likewise, increasing the leg spacing and the copper contact thickness can increase the heat captured by the thermoelement, and thus positively effect the efficiency and power production of a TEM. The critical module facets are described in the proceeding section.
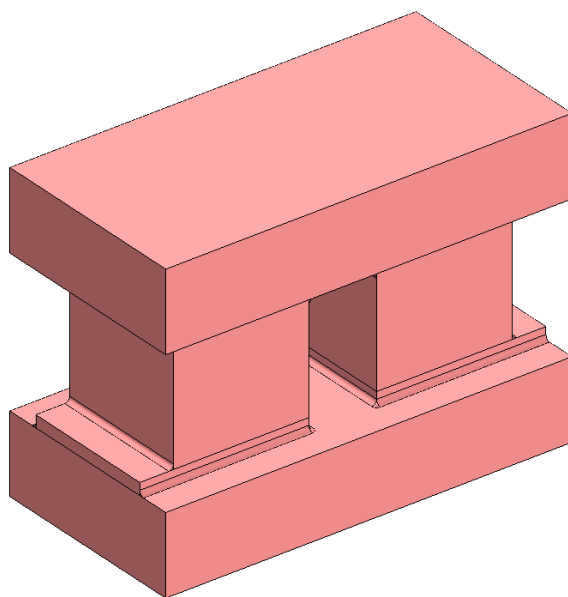


Figure 5.1: FEA model of a thermoelement junction in COMSOL

## 5.4 Nuances of the COMSOL Model

Singularities in computation arise in FE algorithms when sharp right angle geometries exist, and cannot be alleviated with standard mesh refinement. Small fillets (radius of 0.05mm) can be added to right-angle geometries to minimize computational error without compromising the behavior of the thermoelectric device.

Electrical contact resistances can have a significant impact on module performance and design optimization. In order to implement contact resistance boundary conditions, it is necessary to implement identity pairs at the critical internal boundaries. This can be done by treating the couple as an assembly (this option treats every subdomain as independent, unless identity pairs are specified by the user governing the interactions between subdomains) and creating identity pairs at all internal boundaries. The subdomains can be modeled with thermal and electrical insulation while the identity pairs can be given either continuity or contact resistance boundary conditions. With $\rho_c = d/\sigma$ , any combination of $d$ and $\sigma$ that yields the necessary contact resistance value will suffice.

However, the contact resistance for a given element pair is difficult to quantify. Previous work reports contact resistance values spanning $10^{-12}$ to $10^{-8} \Omega \cdot m^2$, however many values are listed merely as a variable that is numerically altered to fit a model to given experimental results [16]. Previous work that attempts to experimentally quantify contact resistances disclaim the results as piecemeal [24]. As such, the proposed model does not contain any contact resistances, but can easily incorporate them with the alteration of a few boundary conditions. The boundary conditions are left in a form that can incorporate the contact resistances if required, but $\rho_c$, the contact resistance of a boundary, is assumed to have a value of zero in the analysis that follows.

## 5.5 Implementation of Model in COMSOL

For quantitative comparison to other models, the same module parameters were used in the 3-D FE model as the 1-D analytical models, seen in Table 3.1. Several sets of material property data were used to test varying extremes of module operating conditions. Melcor material property data, provided by private communications with Dr. Jeff Herschberger of Melcor, was used as a benchmark commercial $Bi_2Te_3$. Additionally, data was taken from the CRC Handbook for the purposes of external reproducibility (the data is available to everyone), to simulate p-type and n-type legs with different material properties, and to probe high temperature ($T_H = 973$K, $T_C = 440$K) thermoelectric materials [12]. The material property data can be seen in Appendices A1-A5. The properties for the thermoelement leg pairs are assumed to be isotropic, and temperature-dependent and the properties for the p-type and n-type materials are different.

The hot and cold sides of the TEM are held at desired constant, uniform temperatures ($T_H$ and $T_C$). One side of the thermoelement leg pair is electrically grounded to provide a

voltage reference, while a current boundary condition is applied to the other leg to simulate closing the loop on a given electrical load. The current can be adjusted to simulate a range of loading conditions to fully capture the current-voltage relationship for a specific TEM for a given set of temperatures. All of the subdomains and boundaries are depicted in Fig.(5.2) and correspond to the conditions outlined in Tables 5.1 and 5.2.
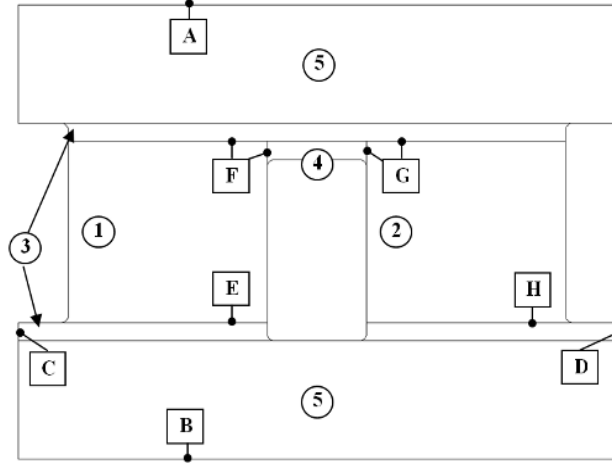


Figure 5.2: TEM COMSOL model subdomain and boundary conditions

Table 5.1: COMSOL Model Subdomain Physics Settings

| Subdomains | Condition |
|---|---|
| **1** : | p-type subdomain obeying Eqs.(1-6) |
| **2** : | n-type subdomain obeying Eqs.(1-6) |
| **3** : | Copper (Cu) contacts obeying $\mathbf{J} = [\sigma] \cdot \mathbf{E}$ and $\nabla \cdot ([k] \cdot \nabla T) = \mathbf{J}^2/\sigma$ |
| **4** : | Tin Lead (Sn-Pb) contacts obeying $\mathbf{J} = [\sigma] \cdot \mathbf{E}$ and $\nabla \cdot ([k] \cdot \nabla T) = \mathbf{J}^2/\sigma$ |
| **5** : | Alumina substrates with no current and $\nabla \cdot ([k] \cdot \nabla T) = 0$ |

All non-specified external boundaries in Table 5.1 are electrically and thermally insulated. All non-specified internal boundaries observe continuity. Boundaries E, F, G, and H can be made to have electrical contact resistances $\rho_c = d/\sigma$, (where $\rho_c$ is the electrical contact resistance and $d$ and $\sigma$ are the COMSOL parameters for contact resistance thickness and electrical conductivity respectively) however for the purposes of this investigation the contact resistances are assumed to be zero. The contact resistances conditions are left in the model for the sake of completeness, however $\rho_c = 0$ as described earlier.

Table 5.2: COMSOL Model Boundary Physics Settings

| Boundaries | Condition |
|---|---|
| **A** : | $T = T_H$ |
| **B** : | $T = T_C$ |
| **C** : | $V = 0$ |
| **D** : | $J_{Lead} = I/A_{Lead}$ |
| **E** : | $[k]_1 \nabla T_1 - [k]_2 \nabla T_2 = T[\alpha]_P \cdot \mathbf{J} + \rho_c \cdot \mathbf{J}^2$ |
| **F** : | $[k]_1 \nabla T_1 - [k]_2 \nabla T_2 = -T[\alpha]_P \cdot \mathbf{J} - \rho_c \cdot \mathbf{J}^2$ |
| **G** : | $[k]_1 \nabla T_1 - [k]_2 \nabla T_2 = -T[\alpha]_N \cdot \mathbf{J} - \rho_c \cdot \mathbf{J}^2$ |
| **H** : | $[k]_1 \nabla T_1 - [k]_2 \nabla T_2 = T[\alpha]_P \cdot \mathbf{J} + \rho_c \cdot \mathbf{J}^2$ |

# 5.6 Implementation of Boundary Conditions in COMSOL

A heat flux discontinuity known as the Peltier heat occurs at the internal boundaries between a thermoelectric and any other material when operating in power generation mode. This heat represents the amount of energy absorbed or liberated by charge carriers when crossing from the energy band of one material into the energy band of a different material, and can be seen as the first term on the right side of Eq.(5.1). Because there is an electrical potential discontinuity, energy (in the form of heat) must be absorbed or given off in order to preserve current (or charge carrier) continuity.

The heat at a given boundary is governed by Eq.(5.1). It is important to recognize that the Seebeck coefficient, $\alpha$ , is the difference between the respective Seebeck coefficients of the materials that form the internal boundary.

$$[\alpha] = [\alpha_1] - [\alpha_2] \tag{5.7}$$

where the subscripts 1 and 2 represent the local material at the internal boundary. The convention for determining the order of the Seebeck coefficients of adjacent materials in Eq.(5.7) is defined as follows: subtract the value of the material Seebeck coefficient bottom from top, right from left etc.

The convention for specifying the Peltier heat that is implemented in the COMSOL FE package is demonstrated in Fig.(5.3). The surface normal direction is determined by the order in which the subdomains are assembled, and can be identified by an arrow plot of the parameters $unx$, $uny$ and $unz$. Using the convention in the example depicted in Fig.(5.3), the Peltier heat liberated takes the following form:

This form of the boundary condition preserves electrical current directionality and is thus generalized. Note that metals and other conductors are treated as having a Seebeck coefficient of zero. A TEM operates at a generator when a heat flux is experienced and the legs are connected in series with an electrical load. The heat flux, in the case of this particular model, is imposed with constant temperature boundary conditions on the two

Table 5.3: Example of Peltier Heat Sign Convention in COMSOL

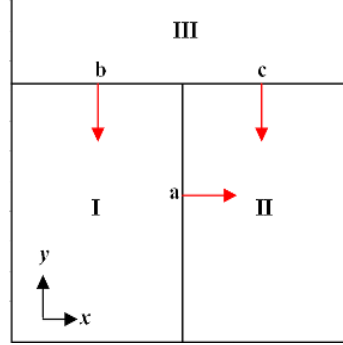| Boundaries | Heat Flux Discontinuity B.C. |
|:---:|:---|
| $\mathbf{a}$ : | $\mathbf{q} = -[k]_{II} \cdot \nabla T = T([\alpha]_I - [\alpha]_{II}) \cdot \mathbf{J} - [k]_I \cdot \nabla T$ |
| $\mathbf{b}$ : | $\mathbf{q} = -[k]_I \cdot \nabla T = T([\alpha]_{III} - [\alpha]_I) \cdot \mathbf{J} - [k]_I \cdot \nabla T$ |
| $\mathbf{c}$ : | $\mathbf{q} = -[k]_{II} \cdot \nabla T = T([\alpha]_{III} - [\alpha]_{II}) \cdot \mathbf{J} - [k]_{III} \cdot \nabla T$ |



Figure 5.3: Example of COMSOL boundary sign convention. Red arrows indicate surface normal direction

interfaces of the module. Power generated by the module can be calculated by the product of the current and the voltage across the two leads. Likewise, the difference between the heat flowing into and out of the module indicates power generated.

## 5.7 Mesh

The thermoelectric leg pair model is sensitive to mesh size. Because the Seebeck effect causes a heat flux discontinuity, a boundary integration is necessary for the computation of the Peltier heat. The boundary integration for the Peltier heat requires a fine mesh (more than ten elements per linear dimension of the boundary) in order to accurately estimate the heat generated or absorbed at the contact. A tetrahedral free mesh is applied in the thermoelement subdomains with a maximum element size of 0.14mm, ensuring a fine, even mesh throughout the legs. The legs, which has a volume of $L \cdot W^2$ (or 1.09mm $\cdot$ (1.4mm)$^2$ using nominal parameter values), can be meshed adequately with about ten elements along each dimension. An element size of 0.14mm would create ten elements along each linear dimension of the leg boundary where the Peltier heat is calculated. The final mesh can be seen in Fig.(5.4).

To confirm that the mesh was of the appropriate size, a mesh refinement series was performed. The mesh was periodically refined (5, 10, 15 and 20 divisions along each dimension corresponding to 125, 1000, 3375 and 8000 elements per leg) and the power output at a constant electrical current (1.5A) was obtained at each iteration, as seen in Fig.(5.5). A decaying exponential curve fit was applied to the peak power predicted at each iteration to determine the actual power at the limit of an infinite number of elements per leg (which presumably
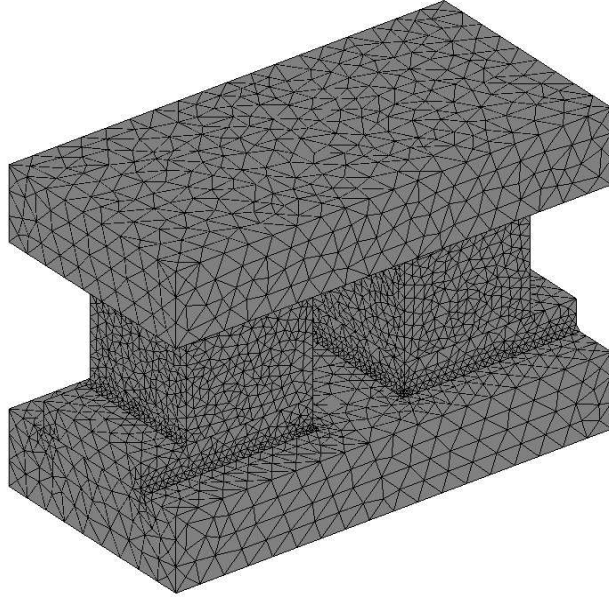
Figure 5.4: Final COMSOL mesh

would be the most accurate model). The purpose of this exercise was to find an optimal solution time for accurate results. With 8000 elements per leg, the simulations required 12 hours on the Large Memory Computer (LMC) to converge and occupied 12-14 Gigabytes of RAM. The LMC is a quad-core machine and is well equipped to handle computationally-intensive models. However, the time of computation was too long to achieve results reasonably (test series would take weeks). Thus, 1000 elements per leg was selected as a reasonably accurate mesh (under 3% error) that could achieve solutions on a regular desktop computer in less than 10 minutes. The exponential took the form:

$$P = a \cdot e^{b \cdot n} + P_{true} \tag{5.8}$$

where $n$ is the number of elements per leg and $P_{true}$ is the power predicted as the number of elements in the leg goes to infinity. After fitting, the exponential took the form:

$$P = 1.812 \cdot 10^{-3} \cdot e^{-1.342 \cdot 10^{-4} \cdot n} + 0.05455 \tag{5.9}$$

Because the rest of the assembly's physics do not require boundary integrations, the other subdomains are not as sensitive to meshing sizes and can be meshed coarsely. This was confirmed by performing a mesh refinement on the ceramic substrates. Changing the number of elements in the ceramic substrates from 150 elements per substrate (the final amount used in the model) to 4000 elements per substrate only amounted to a 0.07% change in predicted power output. Since the mesh involving 4000 elements was more computational intensive and did not amount to a more accurate model, the mesh in the ceramic was left at 150 elements per substrate.

54

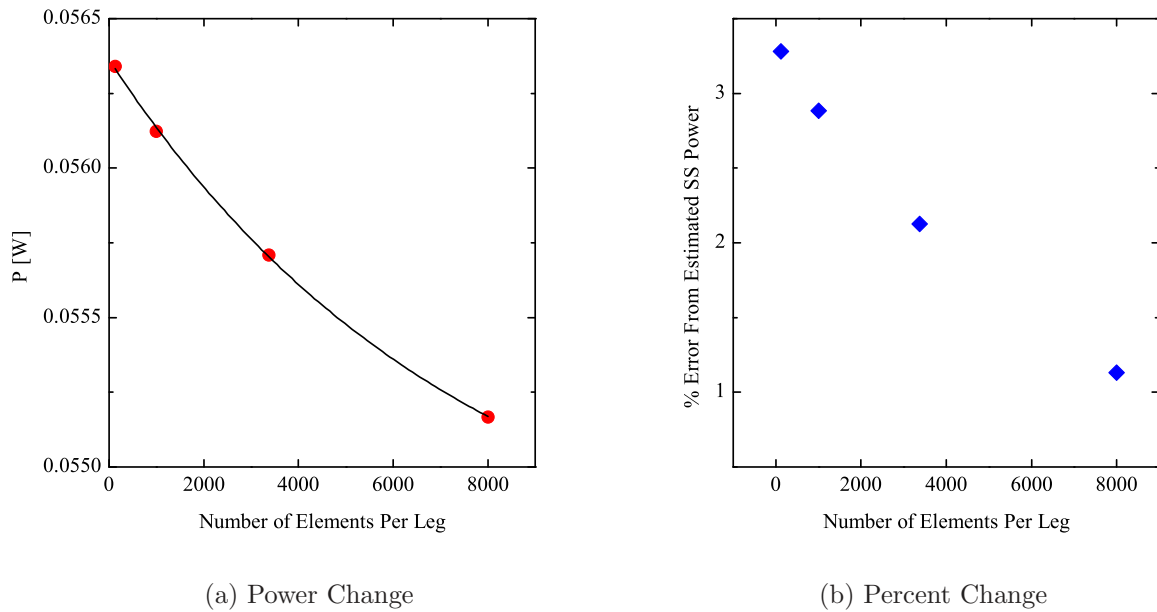|            |            |
| :--------: | :--------: |
| (a) Power Change | (b) Percent Change |

Figure 5.5: Mesh refinement of thermoelement leg and (a) predicted power output and (b) percent change from the true power (right, nominally SS Power). The power output is curve fit to a decaying exponential and the offset is the calculated actual power

An added benefit of using an assembly, aside from using identity pairs for contact resistances, is that each individual subdomain can be meshed separately. For the purposes of computational accuracy, the same maximum mesh size is used for the free mesh in all subdomains. However, mapped meshing is often more efficient and reduces computational error and can be easily implemented for certain geometries, such as purely rectangular blocks. Because small rounded fillets were required to reduce error due to singularities, a mapped mesh was not possible in the current model of the thermoelectric couple.

## 5.8   Solver

Selecting an appropriate general solver and linear system solver is critical to solution convergence. Serious computational errors can arise because the governing equations of a thermoelectric device are uniquely-coupled heat and electrical physics. Likewise, some solvers may inefficiently converge, if at all, because they are not suited for the thermoelectric governing equations. By definition, a thermoelectric system is governed by multiple physics, thus a segregated stationary solver is used for the thermoelectric system with voltage, $V$, and temperature, $T$, being the first and second independent variables respectively.

The linear system solver must be carefully selected based on a given model, governing equations and computational resources. The overall model is decomposed into a large system of linear equations and the solver spends most of the time solving the vast number of unknowns. There is a myriad of methods for converging on a solution to a system of linear

equations, each technique with varying advantages and disadvantages.

Most 3-D models using the COMSOL package are implemented with an iterative solver to conserve computational memory. Iterative solvers must have preconditioners carefully selected and tuned to converge on some systems. In some cases, an iterative solver cannot converge on a solution at all. Direct solvers, which are memory-intensive, are typically used for two-dimensional models because they inherently have fewer elements or 3-D models that have a coarse mesh. However, if a large memory resource is available for 3-D models, direct solvers have no difficulty converging on a solution, regardless of the form of the Jacobian. The UMFPACK algorithm, which is a direct method, was used instead of an iterative method for the solving of the TEM model because of the reasons stated above.

For this work, the Research Computing Group (RCG) has permitted use of the Large Memory Computer (LMC) for the utilization of COMSOL. With 32 Gigabytes of memory and four parallel processors, the LMC can easily utilize a direct solver and converge rapidly. The LMC was necessary in determining the appropriate mesh size because the finely meshed models could not be run on a typical workstation. However, as described in section 5.7, it was found that a coarse mesh could predict module performance with minimal error (approximately 3% error) and that the modeling could be done on a standard workstation.

## 5.9 Postprocessing

Once a solution has converged, there are a few steps of postprocessing to obtain the necessary data. Boundary integrations must be completed to determine the power produced, module efficiency and energy balance. A boundary integration of heat flux on the hot and cold sides (boundaries A and B respectively of Fig.(5.2)) yields heat flowing into and out of the module, and likewise a boundary integration of electric potential of the electrical lead boundary with a current density (surface D in Fig.(5.2)), yields the surface electric potential $V_S(V \cdot m^2)$. All three of these values can be used to determine module power and efficiency. First, an energy balance can confirm that the electrical and thermal predictions of power are comparable. Often there are errors due to meshing and computation, typically on the order of 3% or less.

$$P_{TEM} = N \cdot (q_{H,P} - q_{C,P}) = N \cdot I \cdot V = N \cdot J_{Lead} \cdot V_s \qquad (5.10)$$

where $q_{H,P}$ and $q_{C,P}$ are the absolute values of the postprocessed heat flow at the hot side and cold side respectively. $V_S$ and $J$ are the absolute values of the postprocessed surface electric potential and the current density boundary condition respectively. The efficiency of a module can also be calculated by the following equation:

$$\eta_{TEM} = \frac{q_{H,P} - q_{C,P}}{q_{H,P}} = \frac{I \cdot V}{q_{H,P}} \qquad (5.11)$$

To calculate the peak power of a TEM from the finite element model, the power is determined at five electrical current loads. These five operating points are then fit to a

second order polynomial using a least squares technique.

$$P_{TEM}(I) = aI^2 + bI \tag{5.12}$$

The parameters $a$ and $b$ are altered to minimize the residual. The maximum operating power, $P_{Max}$ occurs when the derivative of $P_{TEM}$ with respect to current, $I$ is equal to zero. The conditions are as follows:

$$I_{PMax} = \frac{-b}{2a} \tag{5.13}$$

$$P_{Max} = -\frac{b^2}{4a} \tag{5.14}$$

This curve fit and resulting calculation gives a good approximation for $P_{Max}$ of the finite element model and allows for quantitative comparison with the analytical models.

## 5.10 Model Validation

To ensure that the finite element model was developed correctly, it was compared with the analytical model in a 1-D scenario. A thermoelement leg was implemented in COMSOL, given temperature-independent properties (from the integral average method) and had a uniform cross-sectional area, ensuring 1-D transport for both electrical current and heat flow.

This FE model was compared to a 1-D analytical model with identical parameters, as can be seen in Fig.(5.6). As expected, the 1-D COMSOL model with temperature-independent material properties has excellent agreement with the analytical model. This indicates that the Peltier boundary conditions and bulk heating terms were correctly implemented and that the FE model is sound.

## 5.11 Summary

A comprehensive 3-D FE model has been developed. Its modeling capabilities include temperature-dependent properties (including the Thomson effect) and contact resistances, although the later are neglected in further modeling due to a lack of accurate resistance measurements. Likewise, the model has the capability of evaluating functionally-doped thermoelectric materials (whose Seebeck coefficient varies spatially) but this effect is neglected in further analysis because it is out of the scope of this work.

A mesh-sensitivity test series was performed, and it was found that the leg surface where Peltier heat occurs is highly sensitive to mesh refinement and required a relatively fine mesh. Conversely, it was found that the ceramic substrate was fairly mesh-insensitive and could be modeled with a coarse mesh for optimal conversion time.
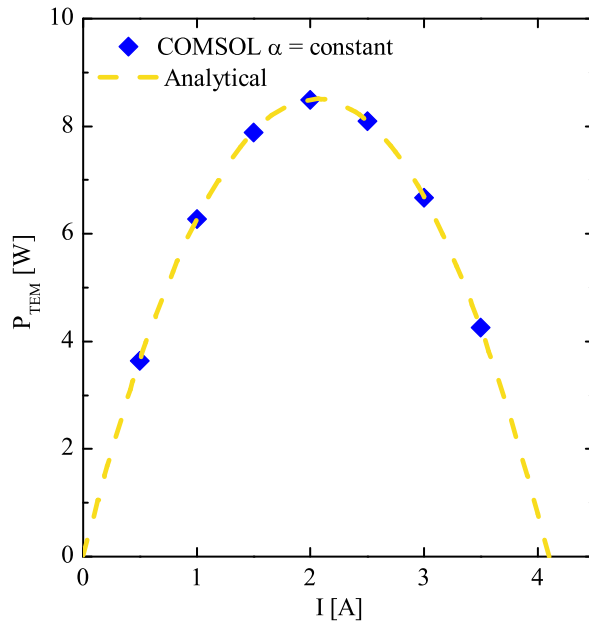
Figure 5.6: Validation of FE Model. Melcor $Bi_2Te_3$ material properties, $T_H = 473K$, $T_C = 307K$, no ceramic interface

Finally, a 1-D FE model with temperature-independent material properties was developed for comparison with a 1-D analytical model and excellent agreement was found, giving good confidence in the FE governing equations and mesh. Because nearly any TEM geometry can be accurately modeled, the 3-D FE model serves as an excellent benchmark for evaluation and validation of analytical models.

# Chapter 6

# Model Comparison

Several models have been presented and explained, however the discrepancies between them have thus far been minimally explored. As a benchmark (and also independent design tool), a finite element model has been developed. Because of the robust nature of finite element techniques, the FE model is the most accurate representation and thus can be used for quantitative comparison between models. Two module facets were identified as potential sources of discrepancy between the 3-D finite element model and the 1-D analytical model: i) material property temperature-dependency coupled with high temperature gradients and ii) heat spreading due to 3-D geometries, particularly in the ceramic interface. These two facets are explored to determine the threshold at which point the 1-D analytical model becomes inaccurate and thereby loses credence as a design tool.

## 6.1 Temperature Dependency

Temperature dependency of thermoelectric material properties, particularly the Seebeck coefficient, give rise to behavior that may not be fully captured by the 1-D analytical models. To probe this issue, a 1-D approximation of a thermoelectric module was implemented in COMSOL. The 1-D COMSOL model consisted of a single thermopile leg. The top of the leg experienced the hot-side temperature, $T_H$, and the inward current flow, $I$, while the bottom of the leg experienced the cold-side temperature, $T_C$ and electrical grounding.

To ascertain the relative impact of the temperature-based Seebeck coefficient, the 1-D COMSOL model was run in two scenarios, the first with constant material properties (determined by the integral average over the experienced temperature difference) and the second with a temperature-dependent Seebeck coefficient only. In both cases, there is no ceramic substrate. The results are seen in Fig.(6.1).

There was little error when the 1-D COMSOL model with temperature-independent properties was compared to the 1-D COMSOL model that had the Seebeck coefficient as a function of temperature (cross-sectional area and leg length from Table 3.1 with no ceramic interface, Melcor Bi$_2$Te$_3$ material properties, Appendix A5). Immediately it is clear that for 1-D cases in the materials that are evaluated, the analytical model with integral-averaged
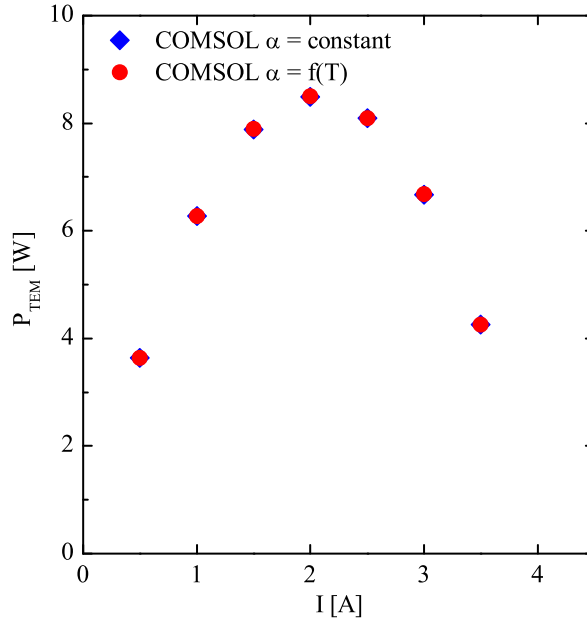
Figure 6.1: Impact of the temperature-dependency of the Seebeck coefficient. Melcor material properties $Bi_2Te_3$, $T_H = 473K$, $T_C = 307K$, no ceramic substrates are included

material properties is an excellent predictive model.

## 6.2   Geometrical Effects and Error Mapping

All analytical models of a TEM have one assumption in common, namely they assume that the heat transfer through the module can be considered 1-D. The validity of this assumption in actual module geometries has yet to be explored. Even with a basic geometry, 3-D voltage profiles can be seen inside the thermoelectric legs, as seen in Fig.(6.2). It should be noted that Fig.(6.2) serves as an example to illustrate 3-D transport, and that it does not reflect the model used for error mapping (which is the quantification of the error between the 1-D analytical model and the 3-D FE model based on geometrical facets which the 1-D model cannot account for).

Given that temperature-dependency does not cause discrepancy between analytical and finite element models, the primary source of error between the two modeling methods must multi-dimensional transport due to geometrical factors. Resultantly, the error between the modeling types should increase at larger temperature gradients, since the 3-D model has two additional dimensions in which heat can flow into the leg. This multi-dimensional transport is referred to as "heat funnelling" in this work. Because the 1-D analytical model cannot account for heat funnelling by itself in any capacity, the performance it predicts will begin to deviate more and more from the 3-D FE model as the heat flow through the module increases. The heat flow through a module at a given temperature gradient can be impacted
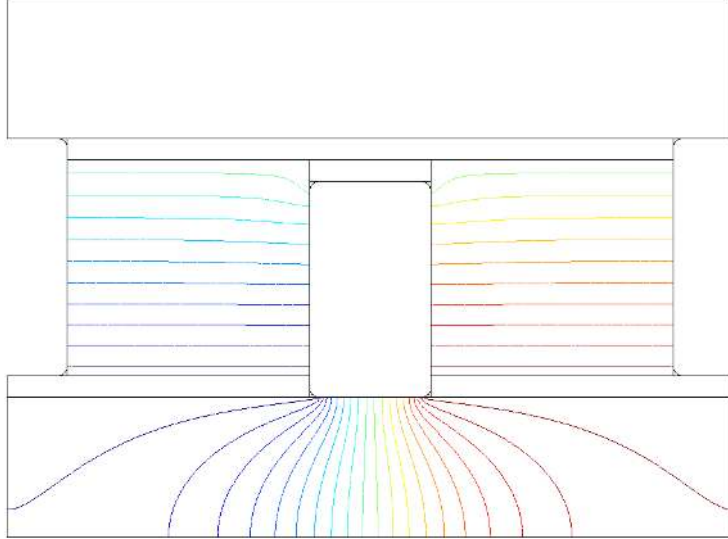
Figure 6.2: Example of a 3-D voltage profile within a thermoelectric junction

by several module design parameters. For a given module geometry configuration, $\alpha$, $k$, $\sigma$ and $k_{Cer}$ can all impact heat flow through the module.

The solder and electrical contact resistances have been removed from the FE model used in the error mapping analysis (see Fig.(3.1)). This allows for quantitative comparison of the discrepancies between the 3-D FE model and 1-D analytical model (with ceramic interface included) due to geometrical effects. Any difference between the models would therefore be a direct result of the 3-D geometry, and not a result of a new geometry facet such as a solder connection or a new contact phenomena, such as electrical contact resistances.

The geometry of the thermoelement legs are identical between the 3-D FE and 1-D analytical models, which is to say that they have the same length and cross-sectional area. However, the 3-D FE model also has leg-spacing, electrical (copper) contacts, and a ceramic interface with a larger cross-sectional area than the thermoelement junction. This leaves the ceramic substrate as the primary contributor to the 3-D transport effects and likewise indicates that the 3-D effects are driven by the heat transport in the ceramic interface.

The two main sources of resistance in the thermal circuit of the TEM is the ceramic substrate and the equivalent thermal resistance of the thermoelectric junctions. The equivalent thermal resistance of the junctions is not the same as the thermal resistance calculated using the thermal conductivity of the thermoelectric materials because the Peltier, Joule and Thomson heat all impact the overall equivalent resistance. Any error between the 1-D analytical model and 3-D FE model would therefore be a function of the ratio between the thermal resistance of the ceramic interface and the effective thermal resistance of the thermoelectric junction. The equivalent thermal resistance of a thermoelectric junction can be approximated as:

$$R_{TE,Eq} = \frac{\Delta T}{q_H} \qquad (6.1)$$

where $\Delta T = T_H - T_C$ is the difference in temperatures from the hot-side ceramic interface to the cold-side ceramic interface and is not based on equivalent junction temperatures. The reason that the boundary temperatures ($T_H$ and $T_C$) are used instead of equivalent junction temperatures ($T_{HE}$ and $T_{CE}$) in this calculation is to allow predictive error mapping, which is also the reason why the resistance is approximated as 1-D despite having 3-D transport. The heat flowing into the module, $q_H$ holds the standard form from Eq.(2.7) and is thus a function of $k$, $\alpha$ and $\sigma$ at a fixed current (recall that in $q_H$ the Peltier heat is accounted for in the first term, and the Thomson heat and Joule heat are accounted for in the $\frac{dT}{dx}$ term). The the thermal resistance for the ceramic is also approximated as 1-D for predictive mapping:

$$R_{Cer} = \frac{t_{Cer}}{k_{Cer} A} \tag{6.2}$$

where $A$ is the cross-sectional area of the thermoelement legs and *not* the cross-sectional area of the expanded 3-D ceramic substrate and $t_{Cer}$ is the thickness of one ceramic substrate.

The 1-D analytical model with ceramic interfaces was compared to the 3-D FE model (also with ceramic interfaces and temperature-independent material properties) by determining the predicted peak power $P_{Max}$ in both scenarios. The error between the two models was plotted against the ratio of $R_{Cer}$ to $R_{TE,Eq}$ for hypothetical scenarios by altering the parameters that the ratio was dependent on- namely $k$, $k_{Cer}$, $\alpha$ and $\sigma$.

Two sets of material properties were selected as base materials to alter, the Melcor material properties (p-type and n-type $Bi_2Te_3$), and the high-temperature CRC material properties (p-type $CeFe_4Sb_{12}$ and n-type $CoSb_3$). The hypothetical scenarios were generated by selecting one thermoelectric material parameter ($k$, $\alpha$, $\sigma$) from the base material and multiplying it by a factor, $f$ to alter the ratio $R_{Cer}/R_{TE,Eq}$ or alternatively $R_{Cer}q_H\Delta T^{-1}$, where $f$ was 1, 1.5 and 1.8, with $f = 1$ being the exact material properties of the base material property. Every factor, $f$, represents a hypothetical material with different properties (say, a material of higher Seebeck coefficient or higher thermal conductivity). The ratio $R_{Cer}q_H\Delta T^{-1}$ was also altered by multiplying the thermal conductivity of the ceramic, $k_{Cer}$ by much larger factors $f_{cer} = 1$, 40, and 100 to test the regime where the models converge.

The results of the error mapping, Fig.(6.3), indicate that the error between the 1-D analytical model and 3-D FE model is proportional to the ratio $R_{Cer}q_H\Delta T^{-1}$ for both the lower-temperature Melcor $Bi_2Te_3$ properties and the higher-temperature CRC $CeFe_4Sb_{12}$ and $CoSb_3$ properties. In Fig.(6.3), $q_H$ (and therefore $R_{TE,Eq}$) is determined in COMSOL by post-processing.

Linear fits of the error, $E$ as a function of the ratio $R_{Cer}q_H\Delta T^{-1}$ for the two cases in Fig.(6.3) yield:

$$E_{Melcor} = 1.840R_{Cer}q_H\Delta T^{-1} - 0.008$$
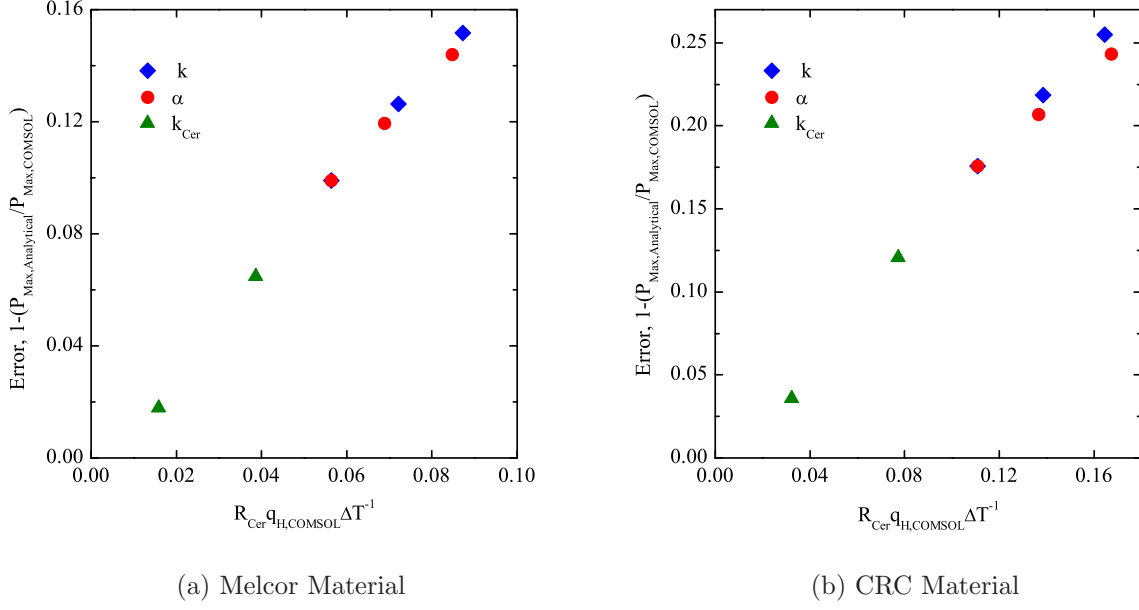
$$R^2 = 0.996$$

(a) Melcor Material        (b) CRC Material

Figure 6.3: Error mapping of analytical model vs. COMSOL. (a) base Melcor material properties $Bi_2Te_3$, $T_H = 473K$, $T_C = 307K$, ceramic substrates are included. The hot-side heat flow, $q_H$ is post-processed from COMSOL. (b) base CRC material properties (p-type $CeFe_4Sb_{12}$ and n-type $CoSb_3$), $T_H = 973K$, $T_C = 440K$, ceramic substrates are included

and

$$E_{CRC} = 1.539 R_{Cer} q_H \Delta T^{-1} - 0.005$$
$$R^2 = 0.988$$

Intuitively, the line in Fig.(6.3) should have a y-intercept of zero. The intercept is slightly off from zero (less than 1% error in the COMSOL post-processed models in Fig.(6.3)) and is an artifact of the numerical FE model likely caused by the mesh. A 1-D FE model slightly underpredicts power output when compared to the 1-D analytical model with identical parameters when a free mesh is implemented. Given that the ratio $R_{Cer} q_H \Delta T^{-1}$ is largely approximated, a less than 1% error is acceptable.

Even more valuable is the predictive error mapping. The issue with Fig.(6.3) is that $q_H$ is determined via postprocessing in COMSOL, which means that the model has to be developed and implemented in COMSOL in the first place. This is not helpful when trying to choose whether or not to model a TEM with a 1-D analytical model or a 3-D FE model, *prima facie*. However, when the error between the 1-D analytical and 3-D FE is plotted against $R_{Cer} q_H \Delta T^{-1}$ where $q_H$ is determined by the analytical model, the trend still indicates proportionality, as seen in Fig.(6.4). Presumably, once a comprehensive error mapping has been completed, a researcher can determine whether or not an analytical model would be adequate for modeling a given TEM versus using a more complex (and expensive) finite
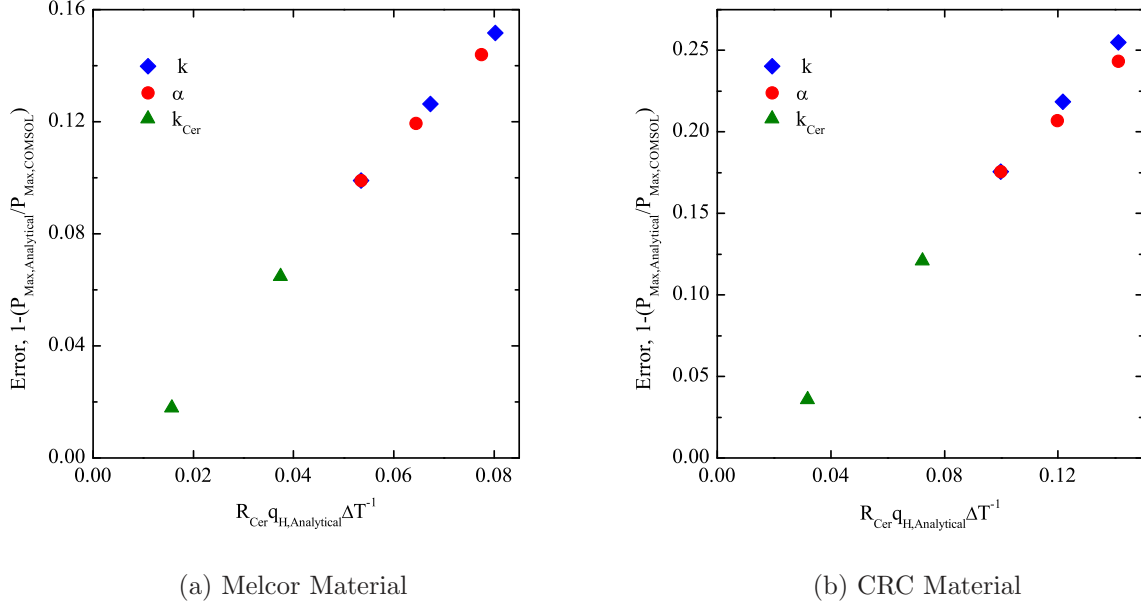
(a) Melcor Material        (b) CRC Material

Figure 6.4: Error mapping of analytical model vs. COMSOL. The thermal resistance ratio is based on the equivalent hot-side heat flow, $q_H$ from the analytical thermal resistance model. On the left side, Melcor material properties $Bi_2Te_3$, $T_H = 473K$, $T_C = 307K$, ceramic substrates are included. On the right side, CRC material properties (p-type $CeFe_4Sb_{12}$ and n-type $CoSb_3$), $T_H = 973K$, $T_C = 440K$, ceramic substrates are included

element model, without ever using a FE package. This can be done *for this particular TEM geometry* by calculating $R_{Cer}$ using Eq.(6.2) and $R_{TE,Eq}$ (or $q_H\Delta T^{-1}$) from Eq.(6.1) (which can be done with known parameters $L$, $W$ (or $A$), $t_{Cer}$, $k$, $k_{Cer}$, $\alpha$, and $\sigma$), and comparing the result to Fig.(6.4).

The results for the fit of the predictive curves in Fig.(6.4) are:

$$E_{Melcor,Pred} = 2.049R_{Cer}q_H\Delta T^{-1} - 0.013$$
$$R^2 = 0.996$$

and

$$E_{CRC,Pred} = 1.899R_{Cer}q_H\Delta T^{-1} - 0.020$$
$$R^2 = 0.988$$

Remarkably (and possibly coincidentally), the Melcor material properties (p-type and n-type $Bi_2Te_3$), and the high-temperature CRC material properties (p-type $CeFe_4Sb_{12}$ and n-type $CoSb_3$) yield predictive slopes for the error curves within 5% of each other. In both cases, the error reaches 0.1 (say, the limit when the one-dimensional model becomes too

inaccurate to use) when the ratio $R_{Cer}q_H\Delta T^{-1}$ reaches about 0.05. This is the case when the ratio of ceramic thermal resistance to the effective resistance of the thermoelectric leg is greater than 5%, the 1-D model will underpredict performance by more than 10% because of 3-D effects. Note that the current TEM parameters have already reached and exceeded the 10% error mark.

The y-intercept for the predictive error mapping results drifts farther away from zero, presumably because more approximations are being made with $q_H$ being treated as fully 1-D transport, but the y-intercept error never exceeds 2%. It is important to note that the predictive error mapping is only valid for the this particular modeled TEM configuration, and has not been made general for multiple geometry scenarios. To examine the impact of other geometry effects on power output (and also qualitatively show the stability of the error mapping), the next section explores new TEM configurations.

As an example of predictive error mapping, a case with Melcor $Bi_2Te_3$ is considered with $T_H = 395K$ and $T_C = 325K$. The analytical model reports that peak power is $P_{Max} = 1.44W$ and occurs at $I_{Max} = 0.86A$ with a heat flow into the module of $q_H = 61W$. Using the predictive error mapping equation, the predicted error of the analytical model vs. the 3-D FE model is 9%. The FE model was run with the same properties and conditions, and reported a peak power $P_{Max} = 1.58W$, which indicated that the 1-D analytical model had 9% error in the peak power.

## 6.3   New Geometry Configurations

New geometries are modeled using COMSOL for several reasons. First, the geometries are altered to see the relative impact on predicted power output of the module. If a given module parameter, say leg spacing $D$, is altered drastically with little impact on predicted peak power then it can be inferred that the predictive error mapping holds accuracy for varying leg spacing. This analysis is purely qualitative and does not establish a universal predictive error map, but it serves to give confidence in error prediction for a family of geometry configurations.

Secondly, this geometric parameter sweep illustrates the design capability of the FE model. Previously unexplored geometric facets can now be probed for optimal TEM performance.

Because a parametric sweep of a geometry can be computationally and labor intensive, the model was simplified to 2-D analysis to facilitate rapid testing. While the 2-D model provides excellent insight, some of the heat funneling effects are exaggerated. This is because there is heat funneling into the leg in the third dimension which is inherent in the thermocouple and not captured in the 2-D model. That is to say, a 3-D model will report slightly higher power output than a 2-D model due to the extra heat being funneled into the leg in the third dimension. As a result, a parametric sweep of a 2-D model would slightly over predict percentage increases in power output. Since the parametric sweeps in this section are meant

Table 6.1: Parameters for Modeling a 2-D Thermoelectric Module from Fig.(3.1)

| Parameter | Value | Symbol |
|---|---|---|
| Leg Height | 1.219 [mm] | $L$ |
| Leg Width | 1.371 [mm] | $W$ |
| Leg Spacing | 0.610 [mm] | $D_{norm}$ |
| Copper Thickness | 0.122 [mm] | $t_{Cu,norm}$ |
| Ceramic Thickness | 0.794 [mm] | $t_{Cer}$ |
| Solder Thickness | 0.122 [mm] | $t_{Solder,norm}$ |
| Ceramic Thermal Conductivity | 27 [W/mK] | $k_{Cer}$ |
| Copper Thermal Conductivity | 400 [W/mK] | $k_{Cu}$ |
| Copper Electrical Conductivity | $6 \cdot 10^7$ [S/m] | $\sigma_{Cu}$ |
| Number of Leg Pairs | 127 | $N$ |

to be qualitative and illustrative, the discrepancies between the 2-D and 3-D model are tertiary.

The impact of altering main geometric effects (e.g. leg spacing, contact thickness, solder thickness) is captured in a 2-D model, and yields insightful results. The parameters for the 2-D model are seen in Table 6.1.

The first parameter that was evaluated was leg spacing. The spacing was increased by factors of 2, 3, and 4 and the peak power at each new leg spacing $D_P$ was compared to the peak power at the nominal leg spacing, $D_{norm}$. No solder was used in this model so that the impact of solder on module performance would not convolute the effect of increasing the leg spacing. The voltage profile of the most exaggerated case, $D_P/D_{norm} = 4$ seen in Fig.(6.5) indicates 1-D transport in the leg, with only slightly more heat being taken in laterally in the ceramic interface. The small increase in peak power (see Fig.(6.6)) indicates that the multi-dimensional heat funneling is minimal and that at large leg separation lengths the predictive error mapping still holds true. The largest increase from peak power is 1.6%, as seen in Fig.(6.6), while the change in efficiency remains negligible. The peak power diminishes after a certain point because increasing the leg length proportionately increases electrical contact length, and thus overall internal electrical resistance of the module.

The copper contact thickness was also increased by factors of 2, 3 and 4 for peak power comparison. No solder was used in this model so that the impact of solder on module performance would not convolute the effect of increasing the contact thickness. The difference in peak power is similarly plotted against the ratio of parameterized contact thickness to normal contact thickness, $t_{Cu,P}/t_{Cu,norm}$. Again, the voltage profiles in Fig.(6.8) indicate largely 1-D transport and the maximum power increase is less than 1% (seen in Fig.(6.7)) indicating that the contact thickness does not have a significant impact in predictive error mapping. The initial peak power increase is likely due to increased mobility for the heat flow in the center of the couple, where the gap exists. The peak power drops after the copper contact thickness was increased by a factor of three. This is due to the increased thermal resistance of the thickening contact. At the standard thickness, the contact's thermal resistance (0.16 K/W)
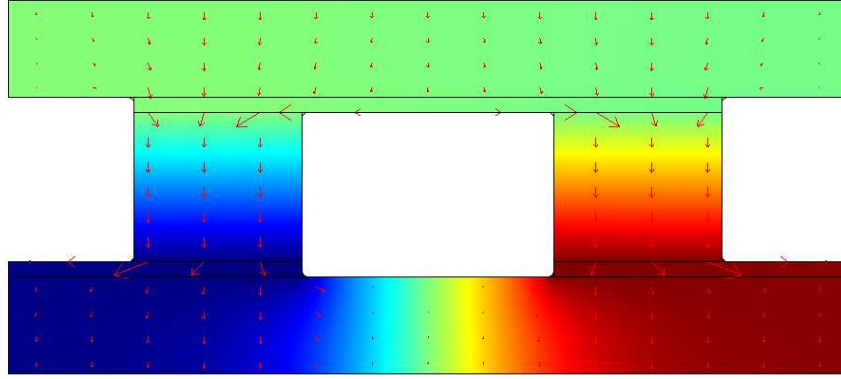
Figure 6.5: 2-D example of increased leg spacing for a TEM with Melcor $Bi_2Te_3$ material properties, $T_H = 473$, $T_H = 307$ and no solder. The voltage gradient is seen in color and the arrows indicate heat flow. This case is for $D_P/D_{norm} = 4$
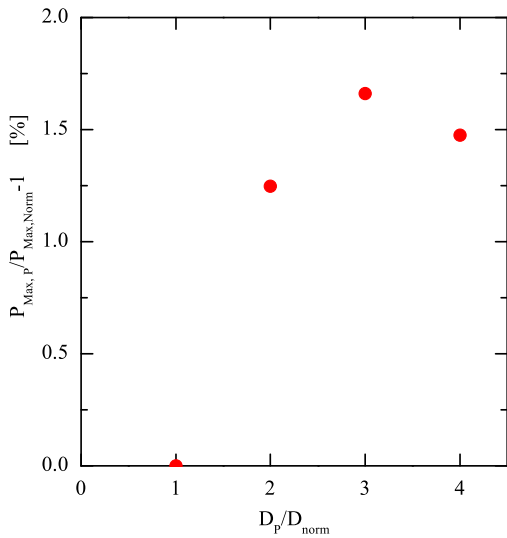


(a) Peak Power
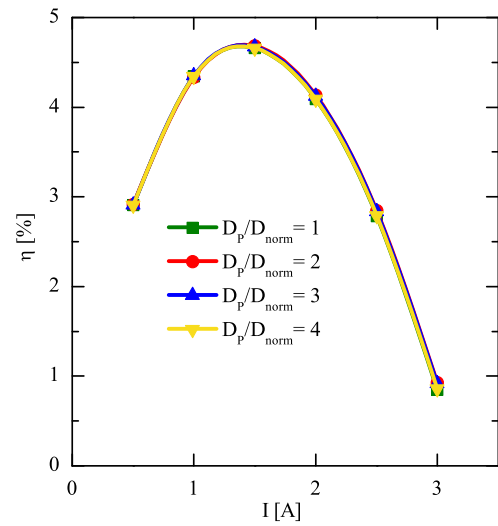


(b) Efficiency

Figure 6.6: 2-D FE module leg distance sweep with Melcor material properties $Bi_2Te_3$, $T_H = 473K$, $T_C = 307K$ and base device parameters from Table 6.1. (a) Peak power vs. parametric sweep of inter leg distance (b) efficiency vs. parametric sweep of electrical contact thickness

67

(a) Peak Power
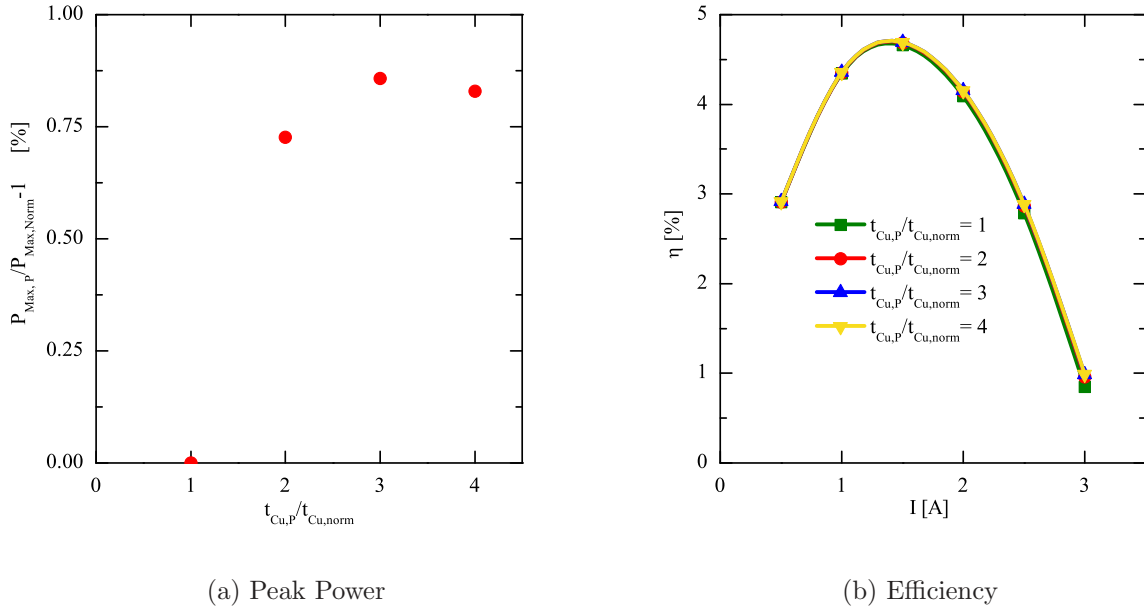
(b) Efficiency

Figure 6.7: 2-D FE module contact thickness sweep with Melcor material properties $Bi_2Te_3$, $T_H = 473K$, $T_C = 307K$ and base device parameters from Table 6.1. (a) Peak power vs. parametric sweep of contact thickness (b) efficiency vs. parametric sweep of electrical contact thickness

accounts for 12% of the equivalent thermal resistance of the thermoelectric at $I = 0.5A$ (1.33 K/W) and increases to 49% of the equivalent thermal resistance of the TE couple when the contact thickness is increased by a factor of four (corresponding to a thermal resistance of 0.65 K/W). Because both of these numbers are overwhelmed by the resistance of the ceramic interfaces (15.52 K/W), the increase in copper thickness has minimal parasitic effect on the overall peak power production of the module and negligible effect on efficiency.

Finally, the solder thickness was increased by factors of 2, 3, 3.5 and 4, and the peak power captured at every instance and compared to a case with no solder (zero thickness). The difference in peak power is plotted against the ratio of parameterized solder thickness to normal solder thickness, $t_{Solder,P}/t_{Solder,norm}$. In this case, the model is highly sensitive to solder joint thickness, as seen in Fig.(6.9). Between $t_{Solder,P}/t_{Solder,norm} = 3$ and 3.5, the peak power increases by nearly 10%. In the image of the worst case scenario, $t_{Solder,P}/t_{Solder,norm} = 4$ seen in Fig.(6.8), heat flow is visibly entering the legs diagonally at the top ceramic interface. This means that heat is being drawn in laterally, and thus the transport is multi-dimensional which can also be seen by the voltage profile in the legs. This heat funnelling effect not only indicates that a solder joint causes the 1-D analytical model to lose accuracy (and also lose predictive error mapping) because of multi-dimensional transport, but that module geometry can be optimized to increase power output by 10% or more, which is congruent with the new high-power-density module design proposed recently by Crane et al [16]. The peak efficiency diminishes only slightly (about 2%), which indicates a net benefit due to the optimization of the solder thickness.
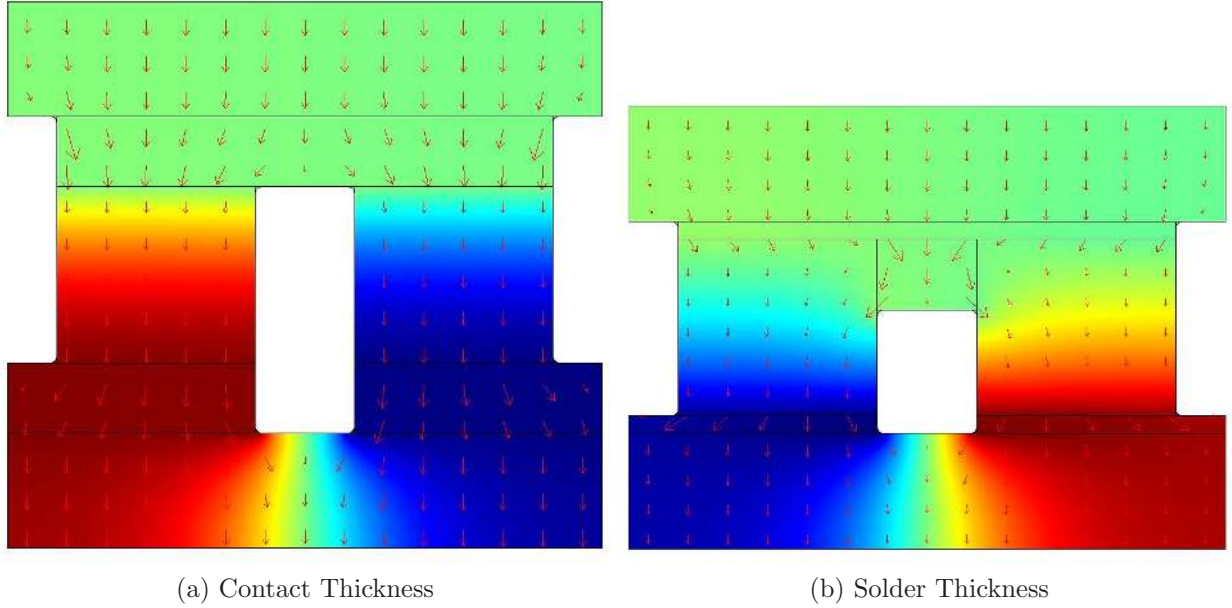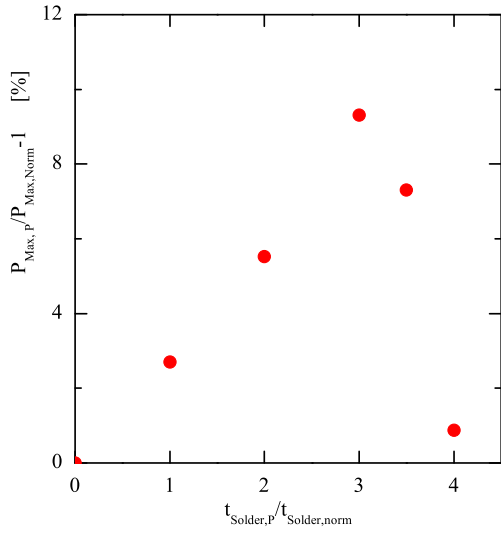
(a) Contact Thickness        (b) Solder Thickness

Figure 6.8: 2-D FE module of new TEM geometries with Melcor material properties $Bi_2Te_3$, $T_H = 473K$, $T_C = 307K$ and base device parameters from Table 6.1. (a) thickened copper contacts with $t_{Cu,P}/t_{Cu,norm} = 4$ (b) thickened solder joint with $t_{Solder,P}/t_{Solder,norm} = 4$

This is profound, because the peak power has increased significantly without adding any expensive material (such as copper or $Bi_2Te_3$). Instead, adding slightly more solder (which is just a tin-lead mixture), has caused a dramatic change in power output. The increase in power output can be attributed to two causes. First, the heat funneling effect has caused heat to come into the legs from a larger area- namely that the solder is assisting the heat in conducting it down into the legs. Relatively large heat flow can be seen going through the solder into the legs in Fig.(6.8). More heat flow through the module leads to higher effective leg temperature differences, which in turn produces higher module power output. The second cause for an increase in power output is that the effective cross-sectional area of the leg has increased at the solder interface, thus the Peltier heat (and resultantly produced power) has increased accordingly. There is, however, a law of diminishing returns, since the solder joint thickness will cause an electrical short through the leg. The peak power occurs when the solder thickness is about one-third of the leg length in this particular geometry, and thus a full optimization may yield a different device configuration than that proposed by Crane et al [16].

The predicted power output is stable (does not change more than 1.6%) across a wide range of geometries for the facets that govern the electrical contacts and ceramic interfaces. This gives good confidence in the predictive error mapping for thermoelement legs of this particular geometric configuration.

When a new geometric facet is introduced, such as increased solder thickness, the multi-dimensional transport can cause a significant increase in the temperature difference across the legs, and likewise a significant increase in power output. The case of the thickened solder joint demonstrates two things. First, it is demonstrative of the shortcomings of the

(a) Peak Power
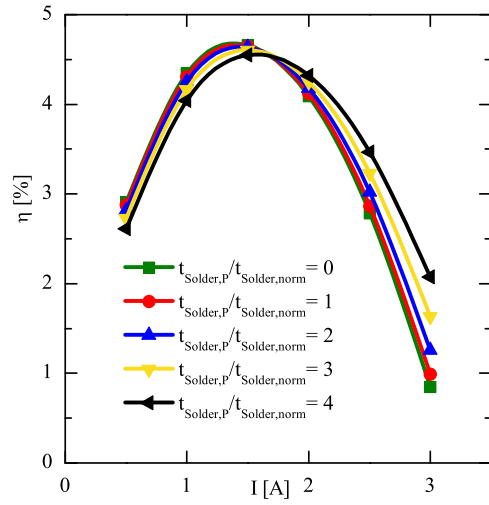
(b) Efficiency

Figure 6.9: 2-D FE solder thickness parametric sweep with Melcor material properties $Bi_2Te_3$, $T_H = 473K$, $T_C = 307K$ and base device parameters from Table 6.1. (a) Peak power vs. parametric sweep of solder thickness (b) efficiency vs. parametric sweep of solder thickness

1-D analytical model (and the inability to use predictive error mapping as a correction for solder geometries) in predicting module performance and secondly, the ability for FE models to be used for sophisticated module optimization. With the price of copper and tellurium increasing, improvements made to module performance by cheaper materials such as solder become even more enticing. Ultimately, it will be economic factors that will determine how large of a role thermoelectric modules play as a power generation technology, so module optimization is critical.

# Chapter 7

# Conclusion

As a nascent technology, the footprint that thermoelectrics will have in efficient, sustainable and remote energy applications will be determined by device-level cost and performance. To address this issue, much effort recently has gone into development of high-performance materials with little impact on commercially available modules. Pivotal in the transition from academic research to commercial development is device-level design tools that can aid in the manifestation of novel materials into practical power production modules.

## 7.1  New Design Tools

At such a critical time in the emergence of thermoelectrics as a solvent power production technology, several novel tools have been established for the purposes of designing and implementing TEMs for power generation applications:

i) Improved analytical models have been proposed that can account for thermal interface resistance, bypass heat leakage and Thomson heating. The exact quantification of the Thomson heat in a bulk thermoelectric material has never been analytically achieved before the asymptotic model. The analytical models (as with any 1-D model), are excellent for quantitatively comparing different materials for performance characteristics, but fail at capturing 3-D effects that are present in TEMs.

ii) A finite element model was implemented in COMSOL to address the 3-D transport in a TEM. This model can account for any possible geometry, thermal and electrical contact resistances, functionally graded doping and temperature-dependent properties (including the Thomson effect). Because the 3-D FE model is robust, it was used as a benchmark for analytical model comparison and validation. The robustness of the 3-D FE model was used in the dissection of module-level effects to determine which effect had the largest impact on device-performance, and which could be neglected. Likewise, the 3-D FE model was used to demonstrate module-level optimization capabilities (although the parametric series only serves as a qualitative demonstration) and was immediately able to identify a new device configuration with a possible 10% increase in power output.

iii) A new method of predictive error mapping for 1-D analytical models has been de-

veloped and demonstrated. The deviation of the 1-D analytical model from actual device behavior (due to 3-D transport) can potentially be predicted based on pre-defined module parameters. With commercial thermoelectric materials, the 1-D analytical model already has a 10-20% error depending on the material and temperature gradient. Eventually, with further work, this technique can be used either as a corrective factor for the 1-D analytical models to capture 3-D module performance without using FE software, or it can be used as a model-selection criteria for researchers trying to determine an appropriate modeling technique for new materials (since the analytical models are simple and cheap to implement, while the finite element models are complex and expensive).

iv) A robust TEM test stand was created, validated and subsequently used for the characterization of a commercially available TEM. The characterization of TEMs can be used both for implementation of said modules into larger power generation systems, and can also be used for model validation (provided accurate material properties are available for the commercial modules). The test stand employs a novel technique for determining the heat flow into a module (a metric notoriously difficult to quantify), and thus has the ability to calculate a module's thermodynamic efficiency. This technique can be extended to a wide base of module test stand configurations, and can predict a module's conversion efficiency to within 5% error.

## 7.2    Discoveries

In addition to the design tools, new insight has been cultivated for both material and module-level parameters that significantly impact device performance and could play new roles in TEM design:

i) An asymptotic solution to the non-linear governing equation of heat in a thermoelectric material has been established. This is the first direct analytical solution to a non-constant Thomson coefficient, which corresponds to most thermoelectric materials. In addition, a method for calculating the effective bulk Thomson coefficient has been established and can be used for quantifying the Thomson heat in a material.

ii) The first such mathematical account for the accuracy of the standard 1-D analytical model in predicting performance of a material with a Seebeck coefficient that is highly temperature-dependent has been established. A highly temperature-dependent Seebeck coefficient means that the governing equations are non-linear and cannot be solved analytically without asymptotic techniques. However, the non-asymptotic analytical model that has an integral-averaged Seebeck coefficient retains excellent agreement with a numerical solution to the non-linear differential equation. This is because the Thomson heat (or the non-linear portion of the governing equation) is embedded in the Seebeck coefficient when it is integral averaged over the experienced temperature gradient. This was mathematically proven by examining the only case when the governing equations can be analytically solved with the Thomson heat (and without asymptotic techniques).

## 7.3 Limitations

Several factors limited some of the original proposed scope of this thesis. Initially, the hope was to use the test stand as a vehicle for validation of models. The ability for model validation through experimentation is predicated on the ability to obtain accurate material property data for a commercially available module. As the material properties that were obtainable did not correspond to any available TEM, there was no way to quantitatively compare a model to a given module and expect good agreement. To address the issue of model validation, the 3-D FE model was rigorously developed as a benchmark. In this way, models could be quantitatively compared and validated for a given set of parameters when compared against the robust 3-D FE model.

Additionally, electrical and thermal contact resistances were left out of the analysis (though the models are capable of accounting for them), despite initial hopes to do so. Mainly, there has been no accurate measurement of contact resistances for thermoelectric devices. Because contact resistances (particularly electrical contact resistances) are used as curve-fitting parameters between models and experimental results, there is no way to tell if the resultant value is capturing the contact resistance purely or is accounting for additional effects. Because of this, reported contact resistance values can range by several orders of magnitude. In addition, experimental characterization of electrical contacts has come with explicit disclaimers of inaccuracy. Without any such accurate measurement, the modeling of contact resistance is impossible.

Finally, the predictive error mapping is not universal for all module configuration. Because of time limitations, the technique could only be demonstrated for a given geometry and has not been generalized yet. There is no way to analytically find a functional form of the dependence of error (between 1-D analytical and 3-D FE) on module parameters since the governing equations are implicit and inseparable. Thus, in order to find a universal functional form of error a large-scale design of experiments (DOE) must be implemented on the 3-D FE model with all module material and geometry parameters. Given that 3-D model geometry development and computation are time-intensive, the technique for error mapping could only be demonstrated and not be made fully universal.

## 7.4 Future Work

Should this work be continued, there are two fronts which are immediately achievable given the newly-developed modeling capabilities. First, a full DOE should be performed on a comprehensive 3-D FE model to establish a universal error map that would include all module geometric and material parameters. This would involve testing a combination of extreme cases, where each parameter is probed. Non-dimensional analysis establishes that unitless power is a function of the following lumped parameters (excluding contact resistances):

$$\frac{P}{kLT_{ave}} = f(\alpha^2 \sigma T_{ave}/k, A/L^2, A_{Cer}/A, k_{Cer}/k, t_{Cer}/L, \Delta T/T_{ave}) \qquad (7.1)$$

where $\Delta T = T_H - T_C$ and $T_{ave} = \frac{T_H + T_C}{2}$, and are thus both a function of the hot and cold side temperatures. The lumped parameters are found by identifying all of the modeling parameters and also all of the dimensions necessary. The smallest possible number of main parameters are selected such that all of the dimensions are represented and then each remaining parameter is expressed by a combination of the main (lumped non-dimensional) parameters. As such, there are eight lumped parameters that govern the performance of a module, and a simple DOE (a total of two extreme cases for each parameter, one large value and one small value) would require at least $8^2 = 64$ scenarios. With each scenario requiring at least two data points to determine peak power, the 3-D FE model would have to be run at least 128 times to determine a functional relationship between all of the parameters, although more sophisticated DOE techniques may reduce this number. In this way, regardless of the geometry, a researcher would be able to predict the error between a 1-D analytical model and the actual module behavior and use the predicted error as a correction factor.

Optimal module design is the second potential research area, since COMSOL provides a unique opportunity for module optimization because it is compatible with MATLAB, a good scripting program with built in optimization algorithms. It would be possible to write a script to optimize a cost factor based on material costs and the performance of a module, and thus design a more economically-viable module. The capacity (and need) for optimization has been demonstrated in this work by increasing module power output by 10% by adding solder, a relatively cheap module component.

In the long term, it would be ideal to have in-house thermoelectric material property testing capabilities and also material synthesis capabilities, although this would require significantly more resources and the cultivation of more materials science expertise or collaborations.

## 7.5   Summary

This work has demonstrated new design advancements and understanding at the material, module and system scale, as summarized in Table 7.1. These advancements can be useful immediately and, reciprocally, in the future. In the short term, increased module performance can be realized with optimized module configurations. Additionally, currently-available modules can be selected for system-level integration more rigorously to provide better system-level performance. In the long term, material selection can be tailored to specific operating conditions of a given application using these advanced models.

With these new insights and tools, tangible improvements to TE technology can be realized, which will aid in securing thermoelectrics as an important power generation resource in a time when energy production is so critical.

Table 7.1: Design Tools and Scope of Use

| Design Tool | Use | Ch. |
|---|---|---|
| Improved 1-D Model | New material-level evaluation and comparison | 3 |
| Error Mapping | Evaluation and selection of new materials for applications | 6 |
| 3-D FE Model | Module-level design and optimization | 5 |
|  | Design and evaluation of novel geometries |  |
|  | Evaluation of new materials at module scale |  |
| TEM Test Stand | Module-level characterization | 4 |
|  | Integration of modules into power-generation systems |  |

# Appendices

# Appendix A

# Material Properties

Table A.1: CRC Thermoelectric Material Properties p-type $Bi_2Te_3$ [12]

| T[K] | $\alpha$[V/K] | $\sigma$[S/m] | k[W/mK] |
|------|------|------|------|
| 482 | 0.000196 | 44943 | 1.071 |
| 473 | 0.000198 | 45998 | 1.043 |
| 448 | 0.000202 | 49603 | 0.992 |
| 423 | 0.000204 | 54525 | 0.971 |
| 398 | 0.000203 | 61274 | 0.970 |
| 373 | 0.000200 | 70671 | 0.979 |
| 348 | 0.000194 | 83472 | 0.987 |
| 323 | 0.000185 | 98522 | 0.985 |
| 298 | 0.000173 | 107874 | 0.963 |

Table A.2: CRC Thermoelectric Material Properties n-type $Bi_2Te_3$ [12]

| T[K] | $\alpha$[V/K] | $\sigma$[S/m] | k[W/mK] |
|------|------|------|------|
| 438 | -0.000161 | 34722 | 1.278 |
| 423 | -0.000171 | 34246 | 1.207 |
| 398 | -0.000187 | 34013 | 1.092 |
| 373 | -0.000201 | 34482 | 0.980 |
| 348 | -0.000210 | 35842 | 0.872 |
| 323 | -0.000213 | 38314 | 0.823 |
| 298 | -0.000209 | 42016 | 0.800 |

Table A.3: CRC Thermoelectric Material Properties p-type CeFe$_4$Sb$_{12}$ [12]

| T[K] | $\alpha$[V/K] | $\sigma$[S/m] | k[W/mK] |
|------|--------|--------|-------|
| 973 | 0.000156 | 117785 | 2.689 |
| 948 | 0.000160 | 118764 | 2.698 |
| 923 | 0.000164 | 119904 | 2.706 |
| 898 | 0.000166 | 121065 | 2.712 |
| 873 | 0.000167 | 122249 | 2.717 |
| 848 | 0.000167 | 123609 | 2.720 |
| 823 | 0.000167 | 125000 | 2.722 |
| 798 | 0.000166 | 126422 | 2.723 |
| 773 | 0.000164 | 127877 | 2.723 |
| 748 | 0.000162 | 129533 | 2.722 |
| 723 | 0.000160 | 131233 | 2.721 |
| 698 | 0.000157 | 132978 | 2.719 |
| 673 | 0.000154 | 134952 | 2.716 |

Table A.4: CRC Thermoelectric Material Properties n-type CoSb$_3$ [12]

| T[K] | $\alpha$[V/K] | $\sigma$[S/m] | k[W/mK] |
|------|--------|--------|-------|
| 973 | -0.000186 | 101936 | 4.274 |
| 948 | -0.000188 | 101522 | 4.186 |
| 923 | -0.000191 | 101214 | 4.102 |
| 898 | -0.000193 | 100908 | 4.024 |
| 873 | -0.000194 | 100806 | 3.950 |
| 848 | -0.000196 | 100704 | 3.883 |
| 823 | -0.000197 | 100704 | 3.823 |
| 798 | -0.000198 | 100806 | 3.771 |
| 773 | -0.000198 | 101112 | 3.727 |
| 748 | -0.000198 | 101522 | 3.693 |
| 723 | -0.000198 | 102145 | 3.668 |
| 698 | -0.000197 | 102880 | 3.655 |
| 673 | -0.000196 | 103842 | 3.654 |
| 648 | -0.000194 | 105042 | 3.665 |
| 623 | -0.000191 | 106496 | 3.689 |
| 598 | -0.000188 | 108225 | 3.725 |
| 573 | -0.000184 | 110253 | 3.775 |
| 548 | -0.000179 | 112612 | 3.837 |
| 523 | -0.000174 | 115340 | 3.910 |
| 498 | -0.000168 | 118343 | 3.992 |
| 473 | -0.000161 | 121654 | 4.082 |
| 448 | -0.000155 | 125156 | 4.179 |
| 440 | -0.000153 | 126422 | 4.212 |

Table A.5: Laird-Melcor Thermoelectric Material Properties for Both p-type and n-type $Bi_2Te_3$

| T[K] | $\alpha$[V/K] | $\sigma$[S/m] | k[W/mK] |
|------|---------------|---------------|---------|
| 273 | ±0.000194 | 108696 | 1.61 |
| 300 | ±0.000202 | 99010 | 1.51 |
| 325 | ±0.000207 | 86207 | 1.53 |
| 350 | ±0.000210 | 78125 | 1.55 |
| 375 | ±0.000200 | 72993 | 1.58 |
| 400 | ±0.000196 | 67568 | 1.63 |
| 425 | ±0.000190 | 63291 | 1.73 |
| 450 | ±0.000186 | 59524 | 1.88 |
| 475 | ±0.000179 | 56818 | 2.09 |

# Bibliography

[1] A. Majumdar, "MATERIALS SCIENCE: Enhanced: Thermoelectricity in Semiconductor Nanostructures," *Science*, vol. 303, no. 5659, pp. 777–778, 2004.

[2] S. Angrist, *Direct Energy Conversion.* Boston: Allyn and Bacon Inc., 1986.

[3] J. Yang, "Potential applications of thermoelectric waste heat recovery in the automotive industry," vol. 2005 of *International Conference on Thermoelectrics, ICT, Proceedings*, (Clemson, SC, United States), pp. 155–159, Institute of Electrical and Electronics Engineers Inc., Piscataway, NJ 08855-1331, United States, 2005.

[4] Ioffe and A.F., *Semiconductor Thermoelements and Thermoelectric Cooling.* Moscow: Publishing House USSR Academy of Sciences, 1956.

[5] S. Lineykin and S. Ben-Yaakov, "Modeling and analysis of thermoelectric modules," *IEEE Transactions on Industry Applications*, vol. 43, no. 2, pp. 505–512, 2007.

[6] M. Srinivasan and S. M. Praslad, "Advanced thermoelectric energy recovery system in light duty and heavy duty vehicles: Analysis on technical and marketing challenges," vol. 2 of *Proceedings of the International Conference on Power Electronics and Drive Systems*, (Kualu Lumpur, Malaysia), pp. 977–982, Institute of Electrical and Electronics Engineers Inc., Piscataway, NJ 08855-1331, United States, 2005.

[7] M. S. Bohn, D. K. Benson, and T. S. Jayadev, "Thermoelectric ocean thermal energy conversion," *Transactions of the ASME. Journal of Solar Energy Engineering*, vol. 102, no. 2, pp. 119–27, 1980.

[8] M. Hodes, "One-dimensional analysis of thermoelectric modules," vol. 1 of *Thermomechanical Phenomena in Electronic Systems -Proceedings of the Intersociety Conference*, (Las Vegas, NV, United States), pp. 242–250, Institute of Electrical and Electronics Engineers Inc., Piscataway, United States, 2004.

[9] M. S. El-Genk and H. H. Saber, "Performance optimization of segmented thermoelectric unicouples," AIP Conf. Proc. (USA), (Albuquerque, NM, USA), pp. 980–8, AIP, 2002.

[10] P. G. Lau and R. J. Buist, "Calculation of thermoelectric power generation performance using finite element analysis," XVI ICT '97. Proceedings ICT'97. 16th International Conference on Thermoelectrics (Cat. No.97TH8291), (Dresden, Germany), pp. 563–6, IEEE, 1997.

[11] E. E. Antonova and D. C. Looman, "Finite elements for thermoelectric device analysis in ansys," 2005 24th International Conference on Thermoelectrics (ICT) (IEEE Cat. No.05TH8854C), (Clemson, SC, USA), pp. 215–18, IEEE, 2005.

[12] D. M. Rowe and G. Min, "Design theory of thermoelectric modules for electrical power generation," *IEE Proceedings: Science, Measurement and Technology*, vol. 143, no. 6, pp. 351–356, 1996.

[13] C. Jincan, Y. Zijun, and W. Liqing, "The influence of thomson effect on the maximum power output and maximum efficiency of a thermoelectric generator," *Journal of Applied Physics*, vol. 79, no. 11, pp. 8823–8, 1996.

[14] M. Freunek, M. Mller, T. Ungan, W. Walker, and L. Reindl, "New physical model for thermoelectric generators," *Journal of Electronic Materials*, 2009. 10.1007/s11664-009-0665-y.

[15] S. A. Omer and D. G. Infield, "Design optimization of thermoelectric devices for solar power generation," *Solar Energy Materials and Solar Cells*, vol. 53, no. 1-2, pp. 67–82, 1998.

[16] D. Crane, D. Kossakovski, and L. Bell, "Modeling the building blocks of a 10% efficient segmented thermoelectric power generator," *Journal of Electronic Materials*, 2009.

[17] A. Rodriguez, J. G. Vian, D. Astrain, and A. Martinez, "Computational model and test bench for thermoelectric power generation, for thermoelectric parameters dependent on the temperature," 2006 25th International Conference on Thermoelectrics (IEEE Cat No. 06TH8931C), (Vienna, Austria), p. 5 pp., IEEE, 2006.

[18] T. Hirano, J. Teraki, and Y. Nishio, "Computational design for functionally graded thermoelectric materials," vol. 308-311 of *Mater. Sci. Forum (Switzerland)*, (Dresden, Germany), pp. 641–6, Trans Tech Publications, 1999.

[19] P. G. Lau and R. J. Buist, "Temperature and time dependent finite-element model of a thermoelectric couple," in *Proceedings ICT '96*, Fifteenth International Conference on Thermoelectrics, (Pasadena, CA, USA), pp. 227–33, IEEE, 1996.

[20] K. Smith, E. Sandoz-Rosado, C. Jno-Charles, C. Henry, E. Herrmann, and R. J. Stevens, "Development of a test stand for the characterization of thermoelectric modules for power generation," in *ASME International Mechanical Engineering Congress and Exposition, IMECE 2007, November 11, 2007 - November 15, 2007*, vol. 8 PART A of *ASME International Mechanical Engineering Congress and Exposition, Proceedings*, (Seattle, WA, United states), pp. 591–598, American Society of Mechanical Engineers, 2008.

[21] K. Smith, E. Sandoz-Rosado, C. Jno-Charles, C. Henry, E. Herrmann, and R. Stevens, "Development of a test stand for the characterization of thermoelectric modules for power generation," *Proceedings of International Mechanical Engineering Congress and Exposition 2007*, vol. IMECE2007-41595, 2007.

[22] E. Sandoz-Rosado and R. Stevens, "Experimental characterization of thermoelectric modules and comparison with theoretical models for power generation," *Journal of Electronic Materials*, 2009.

[23] C. A. Domenicali, "Irreversible thermodynamics of thermoelectric effects in inhomogeneous, anisotropic media," *Physical Review*, vol. 92, no. 4, p. 877, 1953.

[24] R. J. Buist and S. J. Roman, "Development of a burst voltage measurement system for high-resolution contact resistance tests of thermoelectric heterojunctions," in *Eighteenth International Conference on Thermoelectrics. Proceedings, ICT'99, 29 Aug.-2 Sept.*

*1999*, Eighteenth International Conference on Thermoelectrics. Proceedings, ICT'99 (Cat. No.99TH8407), (Piscataway, NJ, USA), pp. 249–51, IEEE, 1999.